

THESIS

CHARACTERIZATION OF GASEOUS AND PARTICULATE EMISSIONS FROM  
COMBUSTION OF ALGAE BASED METHYL ESTER BIODIESEL

Submitted by

Bethany Fisher

Department of Mechanical Engineering

In partial fulfillment of the requirements

For the Degree of Master of Science

Colorado State University

Fort Collins, Colorado

Fall 2009

COLORADO STATE UNIVERSITY

November 10, 2009

WE HEREBY RECOMMEND THAT THE THESIS PREPARED UNDER OUR SUPERVISION BY BETHANY FISHER ENTITLED *CHARACTERIZATION OF GASEOUS AND PARTICULATE EMISSIONS FROM COMBUSTION OF ALGAE BASED METHYL ESTER BIODIESEL* BE ACCEPTED AS FULFILLING IN PART REQUIREMENTS FOR THE DEGREE OF MASTER OF SCIENCE.

Committee on Graduate Work

---

Daniel B. Olsen

---

John Volckens

---

Advisor Anthony J. Marchese

---

Department Head Allan Kirkpatrick

ABSTRACT OF THESIS

CHARACTERIZATION OF GASEOUS AND PARTICULATE EMISSIONS FROM  
COMBUSTION OF ALGAE BASED METHYL ESTER BIODIESEL

The advantages to using biodiesel in place of petroleum diesel are also accompanied by disadvantages. Biodiesel is usually made from crops that are also used to produce food. The land and water use impacts would be profound if current biodiesel feedstocks were used to displace a significant portion of current global petroleum diesel consumption. Oil-producing algae is a favorable alternative to the more common biodiesel feedstocks (soy, canola, etc.) because it does not compete with food sources, does not require arable land to grow and has the potential to produce significantly more oil per area per year than any other oil crops. However, the fatty acid composition of the oil produced by algal species currently under consideration for fuel production differs from that of the more common vegetable oils in that it often includes high quantities of long chain and highly unsaturated fatty acids. When transesterified into fatty acid methyl esters (FAME) biodiesel, the unique fatty acid composition could have a substantial impact on emissions such as Nitrogen Oxides (NO<sub>x</sub>) and particulate matter (PM).

Accordingly, the goal of this study was to examine the effect of the chemical structure of algal methyl esters on pollutant emissions from a diesel engine operating on algae-based FAME biodiesel. Tests were performed on a 2.4 L, 39 kW John Deere 4024T, off-road diesel engine meeting USEPA Tier 2 emissions regulations. The engine was fitted with a unique, low-volume fuel system that enabled emissions tests to be conducted with small specialty fuel samples. Tests were performed on 9 different fuel blends at 2 different engine loading conditions. Exhaust gas measurements were made using a 5-gas emissions analysis system that includes

chemiluminescence measurement of  $\text{NO}_x$ , flame ionization detection of total hydrocarbons, paramagnetic detection of oxygen and non-dispersive infrared detection of CO and  $\text{CO}_2$ . Particulate matter was characterized using an Aerosol Mass Spectrometer (AMS), which is capable of direct measurement of particle composition. The PM size distributions (between 10 to 1000 nm) were measured using a Sequential Mobility Particle Sizer. Total PM mass emissions were measured using gravimetric analysis of Teflon filters and the ratio of elemental carbon to organic was measured using thermo-optical analysis of quartz filters. Experiments were performed with ultra-low sulfur diesel, soy biodiesel (both pure biodiesel, B100, and a blend of 20% biodiesel and 80% diesel, B20), canola biodiesel (B20 and B100), and two synthetic algal methyl ester formulations (B20 and B100 for each). Combustion of algal methyl esters resulted in decreased  $\text{NO}_x$  relative to both canola and soy biodiesel and ULSD, in contrast to previous research that examined the effect of fatty acid saturation and chain length on  $\text{NO}_x$  emissions. A correlation was found between  $\text{NO}_x$  emissions and premixed burn fraction, which provides an explanation for these results. Emissions of formaldehyde and organic PM were found to be slightly elevated with the two algal fuels in comparison with the traditional feedstocks. Particle size distribution, total PM mass, total hydrocarbons, CO and acetaldehyde emissions were similar between the different types of biodiesel.

Bethany Fisher  
Mechanical Engineering Department  
Colorado State University  
Fort Collins, CO 80523  
Fall 2009

## Acknowledgements

Many people contributed to this project, during all stages of planning and implementation, without whom the project would never have been completed. First and foremost, many thanks to Dr. Anthony Marchese for the research plan and all the support along the way. His encouragement and guidance enabled me to overcome many obstacles and grow as an engineer and researcher. A big thank you to the rest of my thesis committee, Dr. John Volckens and Dr. Dan Olsen, for their additional guidance with the many details of the project. The members of senior design team ABBISSET, Morgan Davis, Jason Blaszczyk, Jason Gott, Wes Cravens, A.J. Lyle, and Ben Funderburk, put so much time and effort into getting the engine running and all the auxiliary systems ready. Completing this project without them would have been impossible. We also received a lot of support on this project from Dr. Jeff Collett and Taehyoung Lee from the Atmospheric Science Department. Taehyoung was present for all the testing and completed all the AMS analysis and we also used the Atmospheric Science EC/OC machine during filter analysis.

Many people at the EECL were indispensable. Kirk Evans and Phil Bacon let me ask endless questions and helped with the myriad of technical problems we had along the way. Their knowledge and technical expertise were greatly appreciated. Tim Vaughn, Dave McKenna, Manuel Kern, and Kabel Skelton dropped everything to get the engine ready and help during testing. Mark Machacek with Solix Biofuels profiled the fish oil and provided algae fatty acid profiles.

# Table of Contents

1.	Introduction.....	1
1.1	Biodiesel .....	1
1.2	Algae-based Biodiesel .....	7
1.3	Gaseous Emissions.....	12
1.4	Particulate Matter.....	13
1.5	Thesis Overview .....	18
2.	Experimental Equipment .....	20
2.1	Engine Description.....	20
2.1.1	Fuel System Modifications .....	21
2.2	Exhaust Manifold Modification.....	26
2.3	Data Acquisition and Control System.....	28
2.4	Exhaust Measurements .....	33
2.4.1	5-Gas Analyzer .....	33
2.4.2	Fast NO <sub>x</sub> Analyzer .....	35
2.4.3	Fourier Transform Infrared Spectrometer.....	35
2.4.4	Dilution Tunnel.....	36
2.4.5	Particulate Matter Filter Measurements.....	38
2.4.6	Sequential Mobility Particle Sizer .....	42
2.4.7	Aerosol Mass Spectrometer .....	44
2.4.8	Pressure Transducer .....	46
3.	Fuel Production and Analysis .....	48
3.1	Simulating Algal Oil.....	50
4.	Experimental Procedures .....	54
4.1	Test Matrix.....	54

4.2	Testing Procedures.....	55
5.	Results and Discussion .....	57
5.1	Brake Power Calculation .....	57
5.1.1	Brake Specific Fuel Consumption .....	58
5.2	Gaseous Emissions.....	61
5.2.1	5-Gas Analyzer Results.....	62
5.2.2	Heat Release.....	68
5.2.3	Premixed Burn Fraction and NO <sub>x</sub> Production.....	72
5.2.4	FTIR Results .....	80
5.3	Particulate Matter Emissions .....	83
5.3.1	Total Mass Emissions .....	84
5.3.2	Scanning Mobility Particle Sizer Results.....	86
5.3.3	Elemental and Organic Carbon .....	91
5.3.4	AMS Results .....	94
6.	Conclusions.....	101
6.1	Recommendations for Future Work.....	102
7.	References.....	104
	Appendix A – Additional 5-Gas Results.....	109
	Appendix B – Additional FTIR Results.....	110
	Appendix C - Heat Release Analysis.....	111

## LIST OF FIGURES

Figure 1.1 - Biodiesel production in the U.S. since 2000, adapted from (National Biodiesel Board 2009).	3
Figure 1.2 - Effect of biodiesel on emissions as a function of percent biodiesel blended with diesel, adapted from (EPA 2002).	6
Figure 1.3 - NO <sub>x</sub> and PM trends as related to number of double bonds for methyl and ethyl esters for fatty acids with 18 carbons.	11
Figure 1.4 - Engine exhaust particulate matter sized distribution based on number and mass, adapted from (Kittelson 1998).	14
Figure 1.5 - Particle deposition fraction for different regions of the respiratory system: Head Airways Region, Alveolar Region, TB - Tracheobronchial Region, adapted from (Hinds 1999).	15
Figure 1.6 - Size distribution of particulate matter produced by the combustion of petroleum diesel (B0) and a biodiesel blend (B83). Reprinted with permission from the author (Bennett, et al. 2008).	17
Figure 1.7. Changes in total mass, elemental and organic carbon in exhaust due to biodiesel content in fuel. Reprinted with permission from the author (M. Bennett 2007).	18
Figure 2.1 – Schematic of fuel system for all four cylinders, including the isolated cylinder fuel system and isolation bolt.	23
Figure 2.2 - Mass flow meter configuration.	23
Figure 2.3 - Schematic diagram of redesigned fuel injection system for the 4024T engine.	25
Figure 2.4 - Completed fuel injection system and instrumentation panel.	25
Figure 2.5 - Schematic of Exhaust Manifold and orientation of sample probes on cylinder 4.	27
Figure 2.6 - Photograph of all the probes installed on the exhaust manifold. Cylinder 1 is located on the left; cylinder 4 is on the right.	28
Figure 2.7 - Electrical control box containing cRIO and associated data acquisition systems.	29
Figure 2.8 - Main screen of LabVIEW program showing temperatures, pressure, fuel flow rates, and engine speed, power and torque.	30
Figure 2.9 - (a) Dynamometer controller. (b) Dynamometer control screen from LabVIEW program.	31
Figure 2.10 –Rosemount 5-Gas analyzer rack for measurement of CO, CO <sub>2</sub> , O <sub>2</sub> , NO, NO <sub>2</sub> , and THC.	34
Figure 2.11 – Schematic diagram of dilution tunnel (Bennett, et al. 2008).	36

Figure 2.12 - (a) Filter pack set up. (b) Photo of one cyclone and filter pack line. ....	39
Figure 2.13 - Microbalance used to weigh the Teflon filters.....	40
Figure 2.14 - Sample analysis cycle for Sunset Analyzer, reprinted with permission of the author (Holden 2008). ....	42
Figure 2.15 – Schematic diagram of the Differential Mobility Analyzer (DMA). ....	43
Figure 2.16 - Aerodyne High-Resolution Time-of-Flight Aerosol Mass Spectrometer. ....	46
Figure 3.1 - Large scale biodiesel reactor in the EECL. ....	49
Figure 3.2 - Fatty Acid profile for algae strain <i>Nannochloropsis Oculata</i> and the fish oil mixture used to simulate it. ....	51
Figure 3.3 - Fatty Acid profile for algae strain <i>I. Galbana</i> and the fish oil mixture used to simulate it. ....	51
Figure 4.1 - Samples of red diesel and B100 biodiesels used in tests.....	55
Figure 5.1 - Brake specific fuel consumption (g/kW-hr) for John Deere 4024T engine for 9 different fuel types at rated speed (2400 RPM) and 50% and 75% load. The error bars represent the range of the two runs for each data point. ....	59
Figure 5.2 - Average thermal efficiency for all nine fuels at both loads.....	61
Figure 5.3 - Brake specific carbon monoxide emissions (g/kW-hr) for John Deere 4024T engine for 9 different fuel types at rated speed (2400 RPM) and 50% and 75% load. The error bars represent the range of the two runs for each data point. ....	63
Figure 5.4 - Brake specific total hydrocarbon emissions (g/kW-hr) for John Deere 4024T engine for 9 different fuel types at rated speed (2400 RPM) and 50% and 75% load. The error bars represent the range of the two runs for each data point. ....	64
Figure 5.5 - Brake specific NO <sub>x</sub> emissions (g/kW-hr) for John Deere 4024T engine for 9 different fuel types at rated speed (2400 RPM) and 50% and 75% load. The error bars represent the range of the two runs for each data point.....	65
Figure 5.6 - Brake specific NO emissions (g/kW-hr) for John Deere 4024T engine for 9 different fuel types at rated speed (2400 RPM) and 50% and 75% load. The error bars represent the range of the two runs for each data point.....	66
Figure 5.7 - Brake specific NO <sub>2</sub> emissions (g/kW-hr) for John Deere 4024T engine for 9 different fuel types at rated speed (2400 RPM) and 50% and 75% load. The error bars represent the range of the two runs for each data point.....	67
Figure 5.8. Example heat release rate curve. ....	69
Figure 5.9 - Heat Release Rate (J/deg) from John Deere 4024T engine for B100 Blends at 50% load.....	70

Figure 5.10 - Heat Release Rate (J/deg) from John Deere 4024T engine for B100 Blends at 75% load.....	70
Figure 5.11 - Heat Release Rate (J/deg) from John Deere 4024T engine for B20 Blends at 50% load.....	71
Figure 5.12 - Heat Release Rate (J/deg) from John Deere 4024T engine for B20 Blends at 75% load.....	71
Figure 5.13 - Premixed burn fraction for all fuels. The error bars represent the range of the two runs for each data point.....	75
Figure 5.14 - Brake Specific NO <sub>x</sub> vs. Premixed Burn Fraction. The data points are colored to show fuel type. Diamond-shaped data points correspond to 50% load; Round data points denote 75% load. ....	77
Figure 5.15 - Premixed Burn Fraction vs. Start of Combustion. Diamond-shaped data points correspond to 50% load; Round data points denote 75% load.....	78
Figure 5.16 - Brakes Specific NO <sub>x</sub> vs. Start of Combustion. Diamond-shaped data points correspond to 50% load; Round data points denote 75% load.....	79
Figure 5.17 - Brake specific formaldehyde emissions (g/kW-hr) for John Deere 4024T engine for 9 different fuel types at rated speed (2400 RPM) and 50% and 75% load. The error bars represent the range of the two runs for each data point.....	81
Figure 5.18 - Brake specific acetaldehyde emissions (g/kW-hr) for John Deere 4024T engine for 9 different fuel types at rated speed (2400 RPM) and 50% and 75% load. ....	82
Figure 5.19 - Brake specific total particulate matter mass emissions (g/kW-hr) for John Deere 4024T engine for 9 different fuel types at rated speed (2400 RPM) and 50% and 75% load. The error bars represent the range of the two runs for each data point.....	85
Figure 5.20 - SMPS size distribution for B100 blends at rated speed, 50% load. ....	87
Figure 5.21 - SMPS size distribution for B100 blends at rated speed, 75% load. ....	87
Figure 5.22 - SMPS size distribution for B20 blends at rated speed, 50% load. ....	88
Figure 5.23 - SMPS size distribution for B20 blends at rated speed, 75% load. ....	88
Figure 5.24 - Size Distribution for Soy B100 at 50% and 75% load, with standard deviation error bars shown. ....	90
Figure 5.25 - Elemental and Organic Carbon for 9 different fuel types at rated speed and 50% load. The error bars represent the range of the two runs for each data point.....	92
Figure 5.26 - Elemental and Organic Carbon for 9 different fuel types at rated speed and 75% load. The error bars represent the range of the two runs for each data point.....	93
Figure 5.27. Break down of organic carbon for each fuel at 50% load. ....	95

Figure 5.28 - Break down of organic carbon for each fuel at 75% load. ....	96
Figure 5.29 - Inorganic Components in Organic Carbon at 50% Load. ....	97
Figure 5.30 - Inorganic Components in Organic Carbon at 75% Load. ....	97
Figure 5.31 – Two peaks in ion concentration near mass-to-charge ratio of 59 for B20 blends at 75% load. ....	99
Figure 5.32. Examples of the molecular structure of methyl esters.....	100

## **LIST OF TABLES**

Table 1.1 - Oil yield and land use for common biodiesel feedstocks and microalgae, adapted from (Chisti 2007). ....	5
Table 1.2 - Common fatty acids found in vegetable and algal oils, along with their carbon number: double bond number description and structure.....	9
Table 1.3 - Comparison of fatty acid profiles for seven biodiesel sources based on fatty acid composition by % weight <sup>a</sup> , fatty acids denoted by Carbon #: Double Bond #. ....	10
Table 2.1 - All equipment used to monitor engine and measure properties of the exhaust that were of interest. ....	32
Table 3.1 - Fish Oil Mixtures compared to Algal Oil, percent volume based on number of double bonds.....	52
Table 5.1- Cleanliness of Laboratory Air and Dilution Tunnel .....	83

## LIST OF ABBREVIATIONS

<b>A/F</b>	-	Air Fuel Ratio
<b>ALPM</b>	-	Actual Liters per Minute
<b>AMS</b>	-	Aerosol Mass Spectrometer
<b>B100</b>	-	100% Biodiesel fuel
<b>B20</b>	-	20% Biodiesel, 80% Petroleum Diesel fuel
<b>BC</b>	-	Black Carbon
<b>CH<sub>2</sub>O</b>	-	Formaldehyde
<b>CH<sub>4</sub></b>	-	Methane
<b>CO</b>	-	Carbon Monoxide
<b>CO<sub>2</sub></b>	-	Carbon Dioxide
<b>CPC</b>	-	Condensation Particle Counter
<b>cRIO</b>	-	Compact Rio Data Acquisition System
<b>DAQ</b>	-	Data Acquisition System
<b>DHA</b>	-	Docosaheptaenoic acid
<b>DMA</b>	-	Differential Mobility Analyzer
<b>EC</b>	-	Elemental Carbon
<b>EECL</b>	-	Engine and Energy Conversion Lab
<b>EPA (I)</b>	-	Eicosapentaenoic acid
<b>EPA (II)</b>	-	Environmental Protection Agency
<b>FAME</b>	-	Fatty Acid Methyl Ester
<b>FID</b>	-	Flame Ionization Detector
<b>FTIR</b>	-	Fourier Transform Infrared Spectrometer
<b>HAP</b>	-	Hazardous Air Pollutant
<b>HEPA</b>	-	High Efficiency Particulate Air filter

<b>IPCC</b>	-	Intergovernmental Panel on Climate Change
<b>N<sub>2</sub></b>	-	Nitrogen
<b>NDIR</b>	-	Non-dispersive Infrared Detector
<b>NESHAP</b>	-	National Emission Standards for Hazardous Air Pollutants
<b>NO</b>	-	Nitric Oxide
<b>NO<sub>2</sub></b>	-	Nitrogen Dioxide
<b>NO<sub>x</sub></b>	-	Nitrogen Oxide, the sum of NO and NO <sub>2</sub>
<b>NMHC</b>	-	Non-methane Hydrocarbon
<b>NREL</b>	-	National Renewable Energy Lab
<b>O<sub>2</sub></b>	-	Oxygen
<b>O<sub>3</sub></b>	-	Ozone
<b>OC</b>	-	Organic Carbon
<b>PM</b>	-	Particulate Matter
<b>PM<sub>10</sub></b>	-	Particulate matter smaller than 10 μm
<b>PAH</b>	-	Polycyclic Aromatic Hydrocarbon
<b>PUFA</b>	-	Polyunsaturated Fatty Acid
<b>RCM</b>	-	Rapid Compression Machine
<b>RPM</b>	-	Revolution per Minute
<b>SCFM</b>	-	Standard Cubic Feet per Minute
<b>SMPS</b>	-	Sequential Mobility Particle Sizer
<b>SOC</b>	-	Start of Combustion
<b>SOF</b>	-	Soluble Organic Fraction
<b>TDC</b>	-	Top Dead Center
<b>THC</b>	-	Total Hydrocarbons
<b>ToF MS</b>	-	Time of Flight Mass Spectrometer
<b>ULSD</b>	-	Ultralow Sulfur Diesel

# 1. INTRODUCTION

## 1.1 Biodiesel

The global consumption of natural resources (e.g. fossil fuels) is directly proportional to the global population and the gross domestic product per capita as illustrated by Equation (1.1) below:

$$(1.1) \quad \text{Fossil Fuel Consumption} = \text{population} \times \left\{ \frac{\text{GDP}}{\text{Person}} \right\} \times \left\{ \frac{\text{Fossil Fuel Consumption}}{\text{unit of per capita GDP}} \right\}$$

where GDP is the gross domestic product (Graedel and Allenby 1996). With today's sustained levels of population growth, along with unprecedented economic growth among developing economies, the depletion of fossil fuels promises to be a civilization-scale challenge that will be faced by the human race at some point in the not too distant future. Current estimates predict that the world oil supply could be depleted within the next fifty years, with some models predicting a much sooner date (Appenzeller 2004). Indeed, as indicated by Equation (1.1), the only term affecting total fossil fuel consumption that the human race can reasonably expect to exert significant control is the rate of fossil fuel consumption per unit of per capita GDP. In the transportation sector, 97% of all energy consumption is derived from the combustion of liquid, petroleum-based fossil fuels (Chapman 2007). Liquid biofuels, which are derived from renewable resources such as plants and animal byproducts, have the potential to reduce the rate of fossil fuel consumption.

Our need to find an alternative to petroleum is not only driven by diminishing supply and increasing demand, but also with the intention of reducing the environmental effects caused by the combustion of petroleum products. The pollutants produced by the transportation sector

contribute to smog, ground level ozone and a variety of negative health effects. The 4<sup>th</sup> Report by the Intergovernmental Panel on Climate Change (IPCC) concluded that global warming is occurring and that CO<sub>2</sub> emissions from the combustion of fossil fuels are largely responsible (IPCC 2007).

In the past several decades, biofuels have emerged as candidates to help mitigate the issues of global warming, fossil fuel depletion and, in some cases, atmospheric pollution. To date, the only biofuels that have achieved any significant penetration in the global transportation sector are ethanol and biodiesel. However, ethanol, made through the fermentation of starch, and biodiesel, the product of transesterifying triglycerides, are not the only fuels that can be created from renewable sources. The same technology used to convert crude petroleum into jet fuel, diesel, and gasoline can be used on biomass or plant oil (U.S. Department of Energy 2009). The thermal or catalytic cracking process can be used on triglycerides to remove oxygen and break down the hydrocarbon chains to the lengths required to make renewable diesel, renewable jet fuel, and renewable alcohols. The production of biodiesel in the U.S. in 2008 was roughly 700 million gallons, as shown in Figure 1.1 below, which is well below the production capacity in the U.S. of 2.7 billion gallons (National Biodiesel Board 2009). Until biodiesel production in the U.S. has reached capacity, renewable diesel will not be a profitable product for the crude oil manufacturing plants that processed nearly 80 billion gallons of crude oil in 2008 (Energy Information Administration 2009).

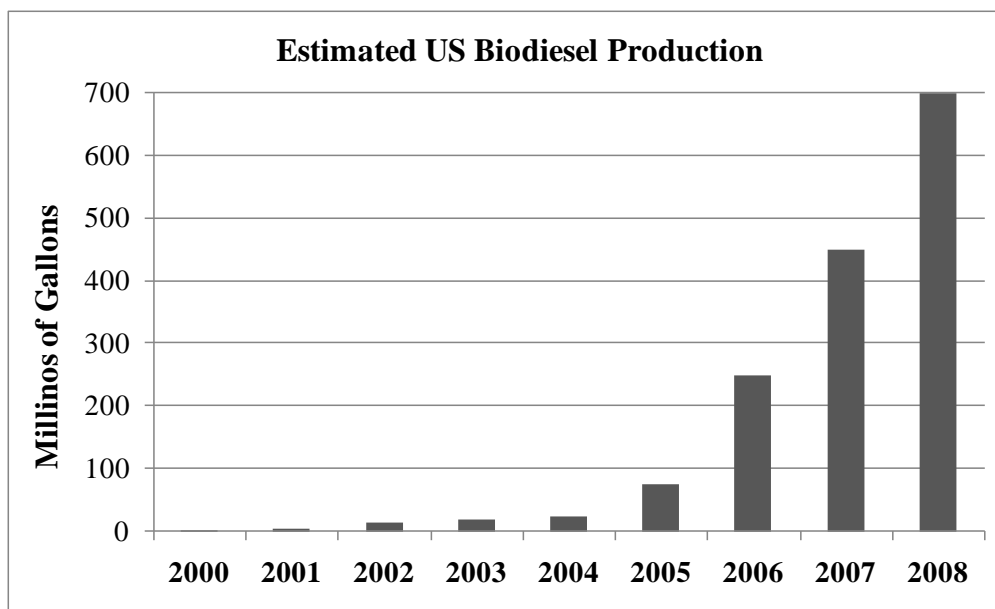
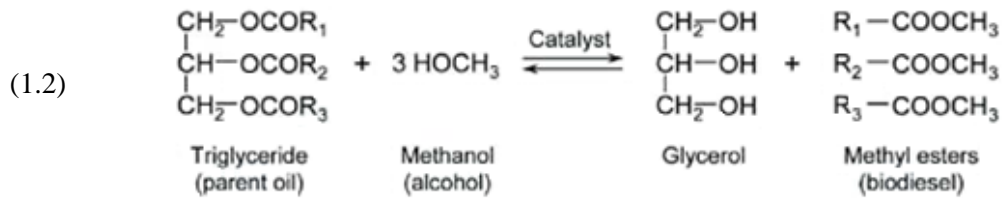


Figure 1.1 - Biodiesel production in the U.S. since 2000, adapted from (National Biodiesel Board 2009).

Biodiesel is defined as a fatty acid alkyl ester produced from either vegetable oil or animal fat (McCormick, Graboski, et al. 2001). Biodiesel has similar properties to petroleum diesel, but is made from non-petroleum oil. Any type of oil, including used vegetable oil or animal fats, can be converted to biodiesel through a chemical process call transesterification. Transesterification, the reaction shown in Equation (1.2), converts triglycerides to alcohol esters (methyl esters in below equation) in a reaction with alcohol and a catalyst. The most common alcohols used are methanol (forming methyl esters) and ethanol (creating ethyl esters) and common catalysts are sodium or potassium hydroxide (Chisti 2007). When using methanol, this reaction replaces the glycerol from the triglyceride with three methyl groups. The glycerol must be separated from the methyl esters before the biodiesel can be used as a fuel. Unlike renewable diesel that will produce the same fuel no matter the feedstock, the feedstock used to make biodiesel impacts the fuel properties and combustion emissions (U.S. Department of Energy 2009).



Biodiesel from vegetable oil produces an overall reduction in greenhouse gas emissions, relative to petroleum diesel, as the plants take in nearly the same amount of CO<sub>2</sub> during growth as is expelled during the combustion of the oil they produce. The use of pure biodiesel in place of petroleum diesel reduces net CO<sub>2</sub> emissions by approximately 80% (Sheehan, et al. 1998). The processing and transport of biodiesel requires fossil fuel energy and these sources for CO<sub>2</sub> emissions must be taken into account when looking at the entire life cycle for biodiesel. When biodiesel is burned in a diesel engine, many combustion products, such as carbon monoxide (CO) and total hydrocarbons (THC), are reduced (Demirbas 2007) (EPA 2002). Feedstock for biodiesel, such as soybeans and canola, can be grown domestically so increasing our use of biodiesel would help reduce our dependence on foreign oil and create domestic jobs.

There are a number of issues that need to be addressed in order for biodiesel to become a realistic alternative to petroleum diesel. First, the crops currently used to produce the feedstock oil for biodiesel do not produce enough oil per area per year to impact fossil fuel consumption significantly. Table 1.1, adapted from (Chisti 2007), summarizes oil yield per area per year from a variety of crops used to make biodiesel. The table also shows the total land area necessary to produce 100% of the transportation fuels consumed in the United States in comparison to the current total U.S. crop area. For most common oil feedstock crops (corn, soy, and canola), significantly more land would be needed than is currently used in all farming nationally. The only crop that has the potential to produce enough oil in a reasonable land area is microalgae. The 2007 Energy Independence and Security Act requires that at least 21 billion gallons of advanced biofuels (i.e. non-corn ethanol) are produced in the U.S. by 2022 (Congress 2007). This would be a significant increase from current production levels (See Figure 1.1) and will require

advanced technology, such as cellulosic ethanol and biofuels derived from microalgae (U.S. Department of Energy 2009).

**Table 1.1 - Oil yield and land use for common biodiesel feedstocks and microalgae, adapted from (Chisti 2007).**

<b>Crop</b>	<b>Oil yield (gal/acre)</b>	<b>Land area needed (M acre)<sup>a</sup></b>	<b>Percent of existing US crop area.<sup>a</sup></b>
<b>Corn</b>	18	7610	1692
<b>Soybean</b>	48	2935	652
<b>Canola</b>	127	1102	244
<b>Jatropha</b>	202	692	154
<b>Coconut</b>	287	489	108
<b>Oil Palm</b>	636	222	48
<b>Microalgae<sup>b</sup></b>	6275	22	5

<sup>a</sup> For meeting 100% of all transport fuels in the United States

<sup>b</sup> Assuming 30% oil (by wt.) in biomass

Table 1.1 also highlights another problem with biofuels. Most of the crops listed above are also vital components of the global food supply. Using these important food sources as fuel feedstock has both ethical and economic implications. For example, when massive government subsidies for corn ethanol were instituted in 2005, the price of tortillas in Mexico soared and the UN's World Food Program asked for \$500 million additional funds to help compensate (Grundwald March 27, 2008). Even if a nonfood crop, such as jatropha, is grown on land that traditionally is used to grow food crops, the feedstock can interfere with the food supply. Biofuels are not likely to replace a significant portion of the petroleum demand if biofuel production continues to compete with food production.

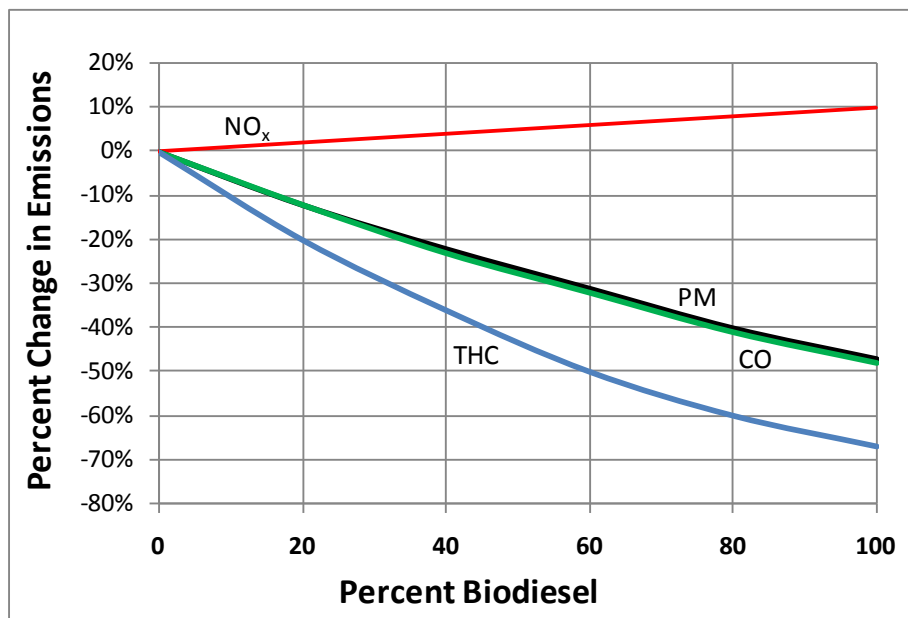


Figure 1.2 - Effect of biodiesel on emissions as a function of percent biodiesel blended with diesel, adapted from (EPA 2002).

Another issue with biodiesel combustion is the increased emissions of nitrogen oxides (NO<sub>x</sub>). While most of the emissions from biodiesel combustion are reduced when compared to petroleum diesel, emissions of nitrogen oxides (NO<sub>x</sub>) generally increase with biodiesel, as shown in Figure 1.2 (EPA 2002). Oxides of nitrogen are a regulated pollutant in the US and the European Union because they contribute to photochemical smog, acid rain and ground level ozone, all of which contribute to health problems (Sheehan, et al. 1998). It is also shown in Figure 1.2 that biodiesel combustion results in decreased mass of total particulate matter. However, recent studies have shown that average particle size is decreased and organic content of the particles is increased for biodiesel combustion (Lapuerta, Armas and Rodriguez-Fernandez 2008) (Bennett, et al. 2008). Both of these trends could have adverse health consequences since smaller particles can be inhaled deeper into the lungs (Kittelson 1998) and the organic matter on the particles has been linked to many of the health effects associated with diesel exhaust such as cancer, respiratory ailments and heart disease (Gaffney and Marley 2009). Despite all the

potential benefits of biodiesel, the problems associated with land use, competition with food sources and increased NO<sub>x</sub> emissions must be rectified if widespread use is ever to be achieved.

## **1.2 Algae-based Biodiesel**

Biodiesel produced from algal oil has the potential to solve many of the problems associated with biodiesel. Algae have been shown to produce 15-70% oil by dry weight (Chisti 2007). Algae can reach maturity in 7-10 days and can grow all year long in certain climates. Accordingly, current estimates suggest that it may be possible to achieve a 2 order of magnitude increase in productivity (gallons per acre per year) from algae in comparison to soybeans (See Table 1.1). To feed the algae during growth, CO<sub>2</sub> is often bubbled up through the algae and the required CO<sub>2</sub> could be supplied by the exhaust from a power plant. Several test sites for algae farms have been established near power plants for this very purpose (Jacquot 2009). Lastly, since there are hundreds of strains of demonstrated oil-producing algae (each with their own unique oil composition), it may be possible to find a type of algal oil that reduces all emissions, not just some of them.

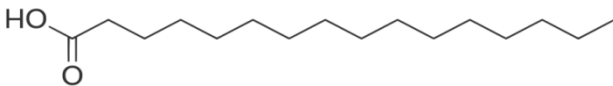
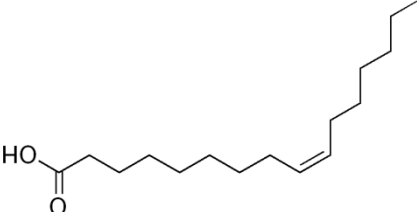
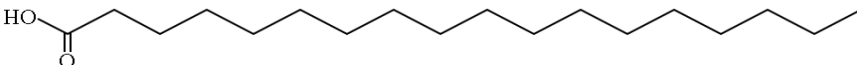
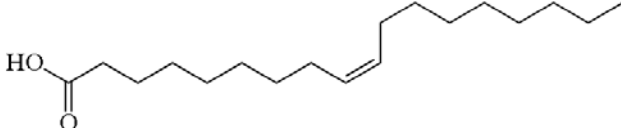
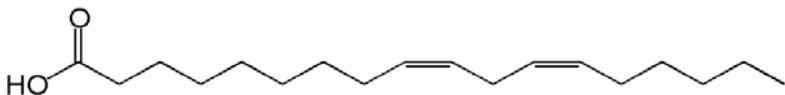
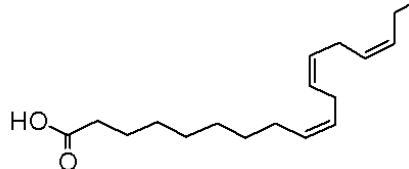
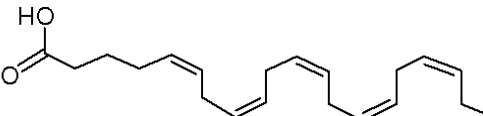
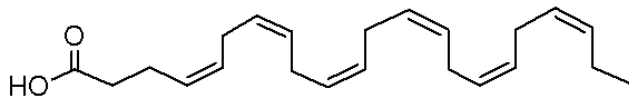
Algal oil has recently attracted attention for its Omega-3 oil content and it is available commercially as a nutritional supplement. For example, Martek Biosciences Corporation (Columbia, MD) sells oil extracted from a species of algae rich in DHA (Docosahexaenoic Acid) to companies that package it in vitamins and in a number of food items, such as milk, canola oil and eggs (Martek Biosciences Corporation 2009). Although algal oil is currently more expensive than the fish oil that is more commonly used as an Omega-3 source, it provides a vegetarian/vegan source for Omega-3 oils. Moreover, it is possible to tailor the algae species/growing conditions to produce a specific oil profile. Much of the research on the production of algal oil to date has been conducted by pharmaceutical companies with the goal of producing Omega-3 oil. Even though the ultimate goal in that research may differ from research focusing on algal oil as a fuel source, it provides a useful resource to researchers looking to grow

algae for fuel. For example, oil profiles for different species of algae and information about growing conditions are important considerations for both algal fuel producers and algal nutritional supplement producers.

One of the advantages to algae-based fuels is also a major obstacle: the endless possibilities for algae type and oil produced. Beginning in the late 1970's, the National Renewable Energy Lab (NREL) in Golden, CO studied algal oil for the development of transportation fuels and determined that there were over 300 types of algae that could produce oil (J. D. Sheehan 1998). A range of environmental preferences are found in this group of oil producers. Some are fresh water algae, some salt water, and some will grow in waste water. Virtually any place in the world could grow algae for oil. However, the high level of diversity also presents researchers with almost infinite variables to consider when choosing an algae species. Additionally, the growing conditions and processing techniques can affect the oil yield and fatty acid composition for any given species.

Algal oil is different from most vegetable oils in that it often contains large amounts (10-50% by weight) of long, polyunsaturated fatty acids (PUFA). Fatty acids are often identified by the number of carbon atoms and number of double bonds in the form Carbon #: Double Bond #. Table 1.2 shows some of the most common fatty acids found in vegetable and algal oils, including their structure and the naming scheme based on carbon number and number of double bonds. The last two fatty acids in the table, EPA and DHA, Eicosapentaenoic Acid and Docosahexaenoic Acid, respectively, are found in many types of algal oil.

**Table 1.2 - Common fatty acids found in vegetable and algal oils, along with their carbon number: double bond number description and structure.**

Names		Structure
<b>Palmitic Acid</b>	16:0	
<b>Palmitoleic acid</b>	16:1	
<b>Stearic acid</b>	18:0	
<b>Oleic Acid</b>	18:1	
<b>Linoleic acid</b>	18:2	
<b>Linolenic acid</b>	18:3	
<b>EPA</b>	20:5	
<b>DHA</b>	22:6	

Typically, the most unsaturated fatty acid seen in other vegetable oils is Linolenic Acid (C18:3), found in Canola oil and Palm oil, as shown below in Table 1.3. However, algal oil can contain high levels of Eicosapentaenoic Acid (C20:5) and Docosahexaenoic Acid (C22:6), which are not typically seen in significant quantities in vegetable oils. The last two feedstocks shown in Table 1.3, *Nannochloropsis Oculata* and *Isochrysis Galbana*, are two types of microalgae that will

be discussed later in more detail. As shown in the table, these algae species can contain around 10 and 20% EPA/DHA by weight.

**Table 1.3 - Comparison of fatty acid profiles for seven biodiesel sources based on fatty acid composition by % weight<sup>a</sup>, fatty acids denoted by Carbon #: Double Bond #.**

Feedstock	8:0	10:0	12:0	14:0	16:0	16:1	18:0	18:1	18:2	18:3	20:0	20:4	20:5	20:6
Soy					10		4	24	54	8				
Canola					5		2	64	20	8				
Coconut	9	6	49	17	8		2	5	2					
Palm				1	42		5	41	10					
Jatropha					11		17	13	47		5			
Nannoch. Oculata				4	29	24	9	4	1	1		5	22	
Iso. Galbana				13	36	32	1	4	4				7	3

<sup>a</sup> The fatty acid profiles shown were compiled from several sources: (Moser 2008) (Tiwari, Kumar and Raheman 2007) (Yuan, Hansen and Zhang 2009) (Fernandez-Feiriz, et al. 1989).

Since EPA and DHA are not found in other vegetable oils and are longer and more unsaturated than the fatty acids more commonly seen, it was unclear how their presence will affect exhaust emissions. Prior to the present study, there had not been any known studies published that looked at the emissions of algae-based methyl ester biodiesel. However, some previous studies have investigated how carbon chain length and number of double bonds affect various emissions from diesel engines operating on methyl esters.

McCormick and coworkers from NREL (2001) investigated how the chemical composition of biodiesel affects the engine-out emissions (McCormick, Graboski, et al. 2001) (Graboski, McCormick and Alleman, et al. 2003). Specifically, they were interested in how chain length and number of double bonds affected the particulate matter and NO<sub>x</sub> in the engine exhaust. They found that for increasing chain length in saturated methyl esters, NO<sub>x</sub> decreased and particulate matter mass increased. When looking at the effect of number of double bonds, they studied methyl esters of C18:0, C18:1, C18:2 C18:3 and saw NO<sub>x</sub> increase linearly as the number of double bonds increased. The results, shown in Figure 1.3, indicated that all these methyl esters

produce a similar and low amount of particulate matter, except C18:2, which produced an atypically large amount of PM.

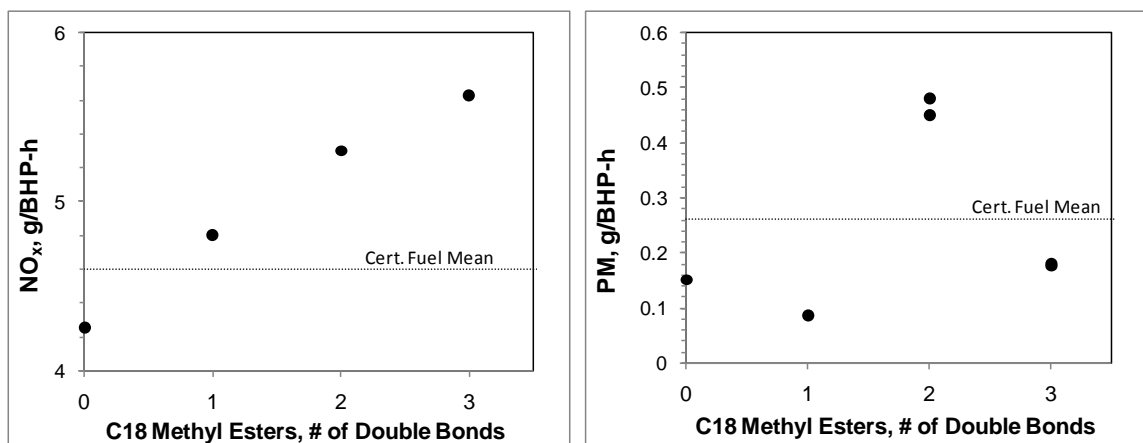


**Figure 1.3 - NO<sub>x</sub> and PM trends as related to number of double bonds for methyl and ethyl esters for fatty acids with 18 carbons.**

A similar study, conducted by Allan and coworkers (2008), used an ultra low volume fuel injection system with a single cylinder diesel engine to test small quantities of pure fatty acid alcohol esters (Allan, et al. 2008). To test the effect of chain length, they looked at saturated methyl esters, with 12, 14, 16, 18, and 22 carbon molecules and found that as chain length increased, NO<sub>x</sub> decreased, with the C22:0 methyl ester producing 20% less NO<sub>x</sub> than petroleum diesel. Total particulate mass, on the other hand, was low and relatively constant between the four shorter saturated methyl esters, but more than doubled for C22:0. Even with the large increase in particulate mass from the shorter chains to the longest, the C22:0 methyl ester still emitted less mass than petroleum diesel. When looking at the effect of increasing double bonds, methyl esters C18:0, C18:1 and C18:2 were studied. As the number of double bonds increased, NO<sub>x</sub> increased, with C18:2 producing 40% more NO<sub>x</sub> than petroleum diesel. Total particulate matter also increased as the degree of saturation increased. Both C18:0 and C18:1 produced less particulate mass than diesel, but C18:2 emitted about 25% more mass than diesel.

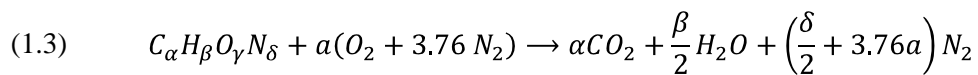
Both papers show that the number of double bonds has a greater effect on NO<sub>x</sub> production than chain length, so even though the longer chains found in algae-based biodiesel

might suggest a decrease in  $\text{NO}_x$ , the greater number of double bonds was expected to be the dominant factor prior to conducting this study. Therefore, an increase in  $\text{NO}_x$  was expected when burning the algae-based biodiesel. The two studies did not find a consistent trend relating to particulate matter, so it was unclear how the algae-based methyl esters would compare in terms of PM. Although  $\text{NO}_x$  and particulate matter were the focus of the two aforementioned studies, it is also possible that combustion of algae-based biodiesel will release anomalous amounts of other pollutants. As mentioned above, the oil produced by algae is different from all types of oil currently used to produce biodiesel and no emissions studies of algae-based biodiesel had been conducted prior to the present study. Accordingly, this work examines how the emissions of this new fuel source will compare to both petroleum diesel and more traditional biodiesel such as soy methyl esters and canola (rapeseed) methyl esters.

Since the effect of algal biodiesel composition on emissions is unclear, various systems were employed to characterize the gaseous and particulate matter emissions.

### 1.3 Gaseous Emissions

In the ideal case, combustion of a carbon-based fuel, such as diesel or biodiesel will produce water and carbon dioxide. For a generic fuel, complete combustion is given by:



However, combustion is never complete, resulting in the production of many other gaseous species. In addition to  $\text{CO}_2$ ,  $\text{H}_2\text{O}$  and  $\text{N}_2$ , a few of the simpler products of incomplete combustion include  $\text{CO}$ ,  $\text{NO}$ ,  $\text{NO}_2$ , and  $\text{O}_2$ . Unburned or partially burned fuel leads to gaseous hydrocarbons in the exhaust. A variety of species can be formed from partially burned fuel, including toxic species like formaldehyde and carcinogens such as polycyclic aromatic hydrocarbons (PAHs).

As previously mentioned, the concentration of  $\text{CO}$  and  $\text{THC}$  produced during combustion tend to decrease as the biodiesel content in a diesel blend increases. When using neat biodiesel

(B100), THC can be reduced up to 70% with respect to petroleum diesel and CO can decrease by 50% (Sheehan, et al. 1998). On the other hand, emissions of NO<sub>x</sub> usually increase as the ratio of biodiesel to diesel increases, up to a 10% increase for pure B100 (EPA 2002). Formaldehyde is another hazardous pollutant of interest but it is unclear how the use of biodiesel affects its production. Some studies have seen decreases in formaldehyde emissions when using biodiesel (Di, Cheung and Huang 2009), but other studies have reported the opposite (Graboski and McCormick 1998).

## **1.4 Particulate Matter**

In addition to the gaseous species that are produced during combustion, particulate species are also created. Diesel fuel is injected as a liquid into the engine cylinder and the resulting fuel-air mixture is not homogeneous (Heywood 1988). Unburned hydrocarbons, from the fuel-rich regions within the cylinder, combine in the exhaust and form the building blocks for particulate matter. Once small particles, 10-20 nm in diameter, have formed, they will start to agglomerate and form large, complex chains (Kittelson 1998). Gaseous species will begin to condense and adsorb on to the surface of the particulates as the temperature decreases. The bulk of the particulate mass is carbon, but a variety of chemical species can be present on the surface that contribute to the health effects associated with engine exhaust (Heywood 1988).

The distribution of particle sizes produced during diesel combustion is generally tri-modal, as shown in the idealized lognormal particle number and mass distributions in Figure 1.4 (Kittelson 1998). The three modes are the nuclei mode (0.005 to 0.05 μm), the accumulation mode (0.1 to 0.3 μm) and the coarse mode (> 1 μm). The particles in the accumulation mode comprise the majority of the particulate mass. The accumulation mode particles consist mostly of agglomerated nuclei mode particles with the adsorbed organic carbon on their surface (Kirchner, et al. 2009). On a number basis, however, the nuclei mode contains the vast majority of the particles. Nuclei mode particles are comprised of layers of grapheme-like sheets of elemental

carbon, organic carbon and inorganic compounds (Kittelson 1998). Coarse mode particles make up the remaining fraction of the diesel exhaust. These larger particles are formed from accumulation mode particles that get trapped on the walls of the engine and exhaust system and continue to grow, before being carried out with the exhaust (Kittelson 1998).

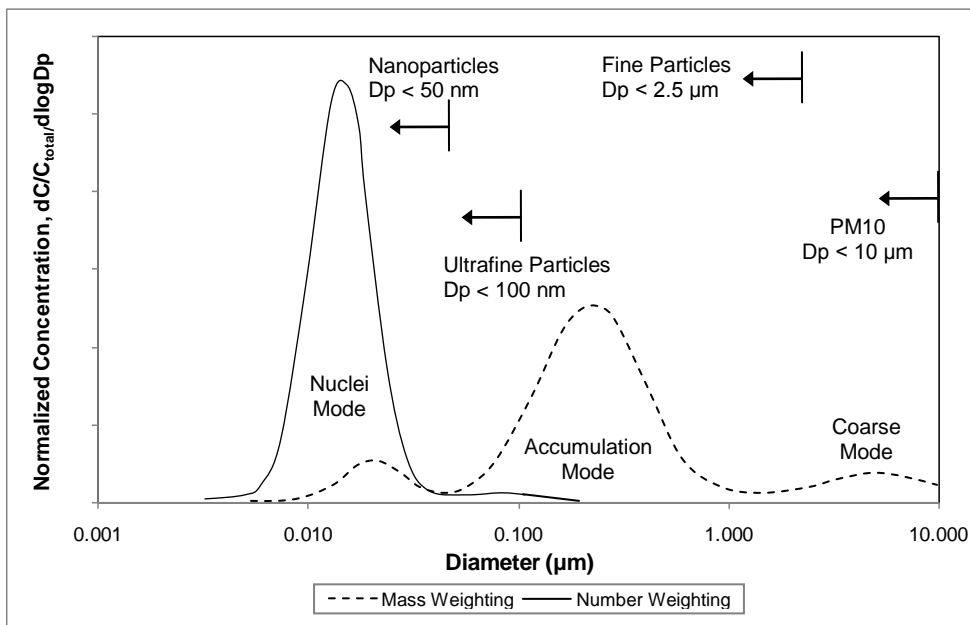


**Figure 1.4 - Engine exhaust particulate matter sized distribution based on number and mass, adapted from (Kittelson 1998).**

The organic compounds that condense on the surface of the carbon molecules include toxic and carcinogenic species and rather than trying to classify each compound found in particulate matter, it may be more useful to distinguish between the elemental carbon, the carbon particles that form the core of the particles, and the organic carbon, representing the hydrocarbons and chemicals adsorbed and absorbed on the surface of this core (Diaz-Robles, Fu and Reed 2008). Black carbon (BC) is another name for elemental carbon and the organic carbon content in particulate matter is also referred to as the soluble organic fraction (SOF). The relative amount of elemental carbon (EC) and organic carbon (OC) in the exhaust can help predict environmental and physiological effects as EC and OC have different chemical, optical, and toxicological properties (Moosmuller, et al. 2001). Elemental carbon absorbs light, while OC tends to scatter

light, so they have an opposing effect on global warming and radiative transfer (Chung, Lall and Paulson 2008). The OC content can contain potential carcinogenic and mutagenic compounds, like polycyclic aromatic hydrocarbons (Alander, et al. 2004), whereas cardiac arrhythmia episodes have been linked to increased exposure to EC (Peters, et al. 2000). There also is a small inorganic component to diesel exhaust, formed from metal compounds in the fuel and lubricating oil from engine wear (Alander, et al. 2004).

Particle size is another important factor that determines the overall health effects of exhaust. The size of the particles will determine how far into the body the particle can penetrate. The figure below shows the fraction of particles that deposit in three regions of the respiratory system.

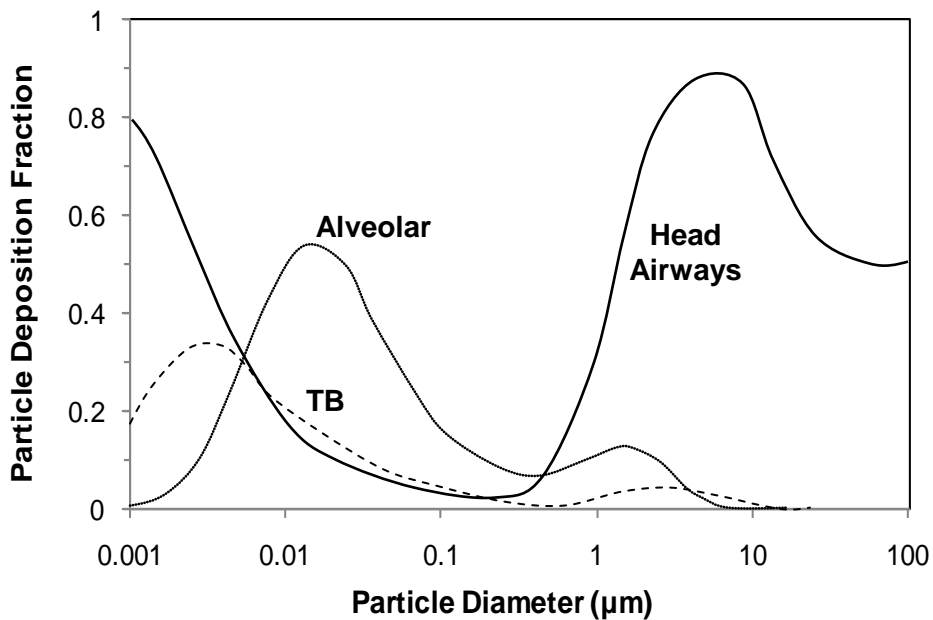


**Figure 1.5 - Particle deposition fraction for different regions of the respiratory system: Head Airways Region, Alveolar Region, TB - Tracheobronchial Region, adapted from (Hinds 1999).**

The head airways region will trap most of the largest particles and the smallest particles. The large particles are caught in nasal hairs or impact at bends in the nasal passage because their inertia is too high to follow the airflow path. The smallest particles deposit in this region because they quickly diffuse to the walls (Hinds 1999). The particles that penetrate through the head

airways then reach the tracheobronchial region. Ultrafine particles, those larger than the smallest particles that diffuse to the walls of the head airways, are deposited in this region due to diffusion. The shorter distance to the walls in the tracheobronchial region, relative to the head and nasal airways, allows these particles to diffuse to the walls in this region. The alveolar region, deep in the lungs where gas exchange takes place, is the final place that particles can deposit. Particles between 0.01-0.02  $\mu\text{m}$  in diameter deposit the most efficiently in alveolar region, as the largest and smallest particles do not make it this far into the lungs. The number distribution of particles produced by diesel combustion usually peaks between 0.05 - 0.1  $\mu\text{m}$  (Burtscher 2005). This is not the most efficiently deposited particle size in the alveolar region, but of the three regions, they are most likely to end up in the alveolar region.

The use of neat biodiesel or biodiesel blends affects many of the particulate matter properties. The total mass concentration and mean particle size produced during combustion decrease with the use of biodiesel (Jung, Kittelson and Zachariah 2006). Both of these trends can be seen in Figure 1.6 as the biodiesel curve is shifted toward smaller particle mobility diameters and the peak is also lower than that of diesel. As illustrated in Figure 1.5, as particle size decreases, the efficiency at which it is deposited in the alveolar region in the lungs increases, making the smaller particles produced by biodiesel potentially more harmful than the larger diesel particulates.

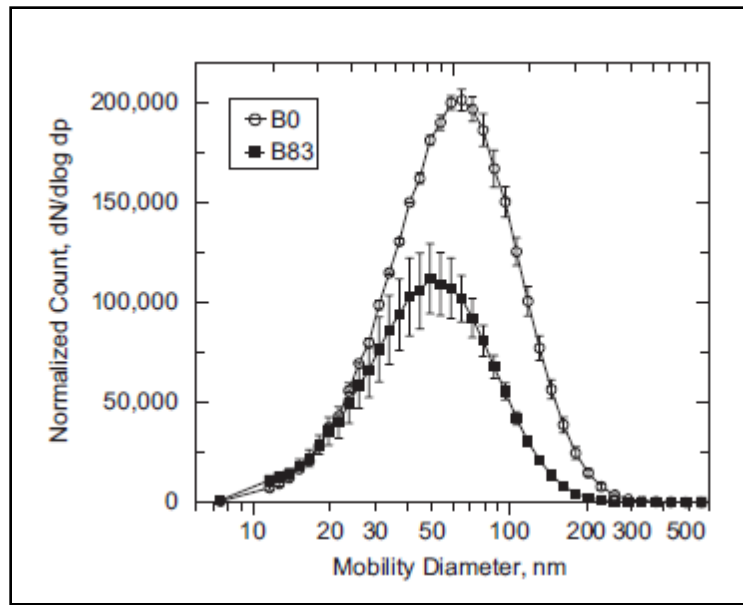


**Figure 1.6 - Size distribution of particulate matter produced by the combustion of petroleum diesel (B0) and a biodiesel blend (B83). Reprinted with permission from the author (Bennett, et al. 2008).**

The breakdown between elemental and organic carbon is also affected by the biodiesel blend ratio. While the elemental carbon content in the particulate matter tends to decrease with the use of biodiesel, the organic carbon content usually increases (Chung, Lall and Paulson 2008). The following figure, from Bennett (2007), which presents data obtained from the same engine used in the present study, supports this trend (M. Bennett 2007). Since OC is comprised of many different hydrocarbons, some toxic and potentially carcinogenic, an increase in OC could be detrimental to human health.

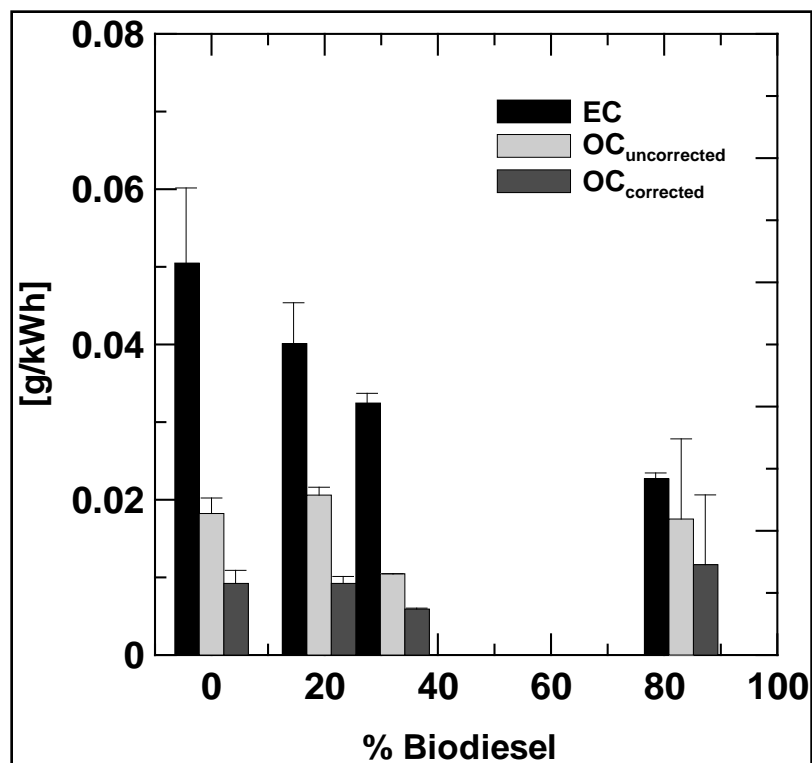


Figure 1.7. Changes in total mass, elemental and organic carbon in exhaust due to biodiesel content in fuel. Reprinted with permission from the author (M. Bennett 2007).

## 1.5 Thesis Overview

This thesis presents the results of several emissions tests designed to determine the differences in emissions between combustion of algae-based biodiesel, soy and canola biodiesel, and petroleum diesel. Oil from microalgae has been touted as a viable alternative to diesel fuel, but the emissions have not been measured. Chapter 2 describes the engine and instrumentation used to perform these tests. Some modifications to the engine and traditional sampling methods were required due to the limited supply of fuel and those changes are described in detail.

In Chapter 3, the specifics for each of the fuels tested are given. The ultra low sulfur diesel and the soy biodiesel were both obtained from commercial sources, while the canola biodiesel and algae-based biodiesel were produced in-house. Two types of algal fuels were synthesized using transesterified fish oil and two pure methyl esters from Procter & Gamble. The

process used to create these two “algal” fuels is based on matching the degree of saturation, on a volume basis, from the actual algal oil profile with the fish oil mixture.

In Chapter 4, the daily testing procedures are described. Before running the engine, the calibration on the dynamometer was corrected. During warm-up, cool down, and in between fuels, all the four cylinders were run on petroleum diesel. The fuels tested, the engine conditions, and the data sets collected during the tests are all described in this chapter.

In Chapter 5, the gaseous and particulate emissions results are presented. All of the raw data is converted into normalized units that are more conducive to comparison, when applicable. The algal fuels produced less  $\text{NO}_x$  than both soy and canola biodiesel, as well as ULSD, but increased formaldehyde emissions. Correlations between  $\text{NO}_x$ , premixed burn fraction and start of combustion are presented as possible explanations for the  $\text{NO}_x$  results. As expected, the biodiesel blends reduced particulate mass but increased the organic carbon fraction of the particulate matter. Most of the particulate results did not vary significantly between the traditional types of biodiesel and the algae-based biodiesels. The aerosol mass spectrometer identified a mass-to-charge ratio value that could be used to identify exhaust due to biodiesel combustion, distinct from petroleum diesel combustion.

In Chapter 6, conclusions from this work are summarized and future tests intended to further explore the differences between algal biodiesel and other biodiesel fuels are described.

## **2. EXPERIMENTAL EQUIPMENT**

All of the experimental work for this project was conducted at Colorado State University's Engine and Energy Conversion Lab (EECL). The EECL, founded in 1992, contains 24,000 ft<sup>2</sup> of lab space and houses a dozen engines used for alternative fuel and efficiency research.

### **2.1 Engine Description**

The test engine was a four-cylinder, turbocharged, glycol and water cooled, off-road John Deere model 4024T built in 2003. The total displacement of the engine is 2.4 L, capable of producing 39 kW at 2400 rpm. Mechanically controlled unit injector pumps deliver fuel to the cylinders and the injection timing was unaltered for the tests presented herein. The load on the engine was applied by a water-cooled eddy current or induction dynamometer, made by Mid-West Dynamometers (model 1014A, River Grove, IL). The speed of the engine, the load produced by the dynamometer, and the resulting power were all measured by a control unit. The speed of the engine was set using a voltage-controlled throttle, while the load was set independently by the dynamometer control unit. Both the throttle and dynamometer control unit are managed with a LabVIEW program.

Two Micro Motion (Boulder, CO) coriolis meters, flow meter model CMF010M323NQEZZZZ and transmitter model 2700R11BBCEZZZ, measured the mass flow rate of fuel feeding an isolated cylinder (to be discussed in more detail) and the three remaining cylinders, respectively. Eleven type K thermocouples were used to monitor temperature in the fuel system as well as other key points on the engine, such as oil temperature and exhaust

temperature. The boost pressure produced by the turbocharger was measured with an Omega (Stamford, CT) PX181B-030G5V pressure transducer. A data acquisition (DAQ) system was installed and programmed to monitor and record temperatures, pressure, and fuel flow rates from both coriolis meters. The dynamometer control unit delivered speed, load and power measurements to the same LabVIEW program. The speed of the engine, synonymous to the speed of the dynamometer, was measured with a Hall Effect RPM (revolutions per minute) sensor built into the dynamometer controller. Two high-speed Kistler (Amherst, NY) 6056A pressure transducers were installed in the engine's glow plug adapters to measure the in-cylinder pressure. The data from these high speed pressure transducers was collected by a Hi-Techniques Win600 computer.

Tests were performed on the exhaust to quantify both the gaseous emissions and particulate emissions for 9 different fuels and at two engine loads. The test matrix will be described in more detail in Chapter 4. The instruments used for these tests are described in the following sections. Some modifications were made to the engine to make the test plan more feasible and those changes will be discussed as well.

### **2.1.1 Fuel System Modifications**

Even though algae-based biodiesel has received a lot of publicity for its potential impact on the future of biofuels, there have been no known emissions studies performed to quantify the environmental and health-related effects from use in an engine. One reason that explains the lack of prior work in this area is the limited availability of algal fuel. There are numerous companies working on producing algal oil for fuel but, to date, most companies are unable to generate the volume of fuel required to perform engine tests at a reasonable cost. Most companies are still evaluating different algal strains and production systems and have not begun scaling up their operations.

Since algal fuel is scarce, operating the entire engine on algal fuel for the time required for some of the emissions tests would have been difficult. With the help of an undergraduate student design team who were enrolled in the CSU MECH486 Senior Design Practicum, the John Deere 4024T engine was modified to isolate the fuel system for one of the four cylinders. This system enabled a single cylinder to operate on one fuel, while the remaining cylinders ran on petroleum diesel at all times. Similar tests performed by Allan et al. used an ultra low volume fuel injection system on a single cylinder engine to accommodate pure methyl ester samples that were only available in small quantities. They took advantage of the high pressure in the common rail fuel injection system on their engine and as a result, their engine was able to run on less than 100 mL of fuel (Allan, et al. 2008). Since the John Deere engine used in this study uses mechanical, cam-driven injector pumps, it was not possible to replicate their design. Instead, the unit pump on one of the four cylinders was isolated from the common fuel system and fuel was injected directly into this cylinder.

The original engine configuration employs a single fuel intake line fed into a fuel galley that supplied fuel to each of the cylinders. A fuel return line collected all the extra fuel from each cylinder and sent the return fuel out of the engine block. To isolate cylinder four, shown at far left in Figure 2.1, a long hollow bolt was inserted into a threaded hole that extended to the inlet of the unit pump. This bolt blocked fuel from the common galley from being fed into the unit pump and also provides a way to supply a different fuel to that cylinder. The end of the bolt on the outside of the engine was then mated to the stainless steel Swagelok fuel lines. An identical bolt was used on the return side of the pump to collect any excess fuel.

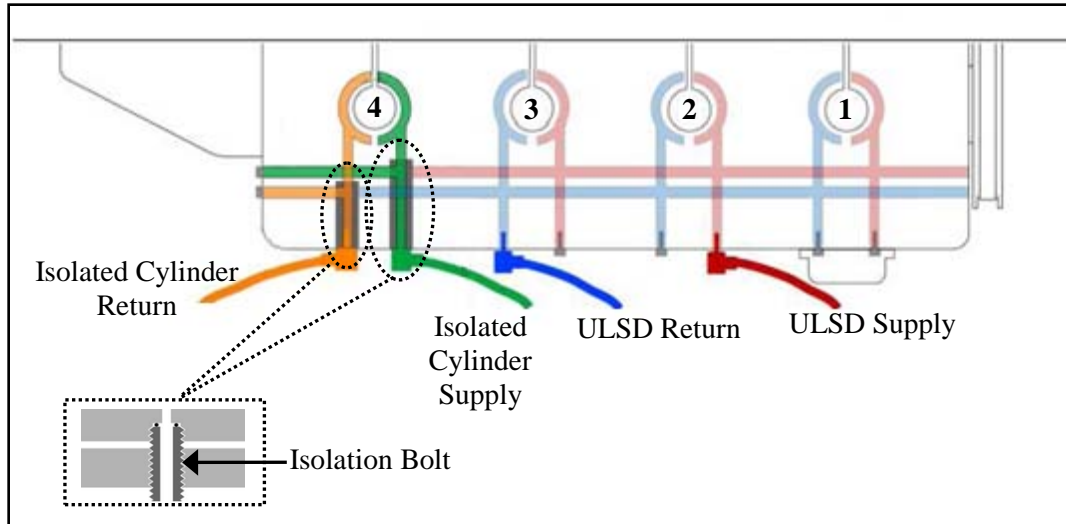


**Figure 2.1 – Schematic of fuel system for all four cylinders, including the isolated cylinder fuel system and isolation bolt.**

The return line of the isolated cylinder fed back into the intake fuel line, upstream of a circulation pump, in an effort to simplify the fuel system and enable the use of one flow meter. When measuring mass emissions of exhaust pollutants, it is critical to measure the instantaneous mass flow rate consumed by the engine, which is the difference between the mass flow rate of fuel supplied and the mass flow rate of fuel returned. The mass flow meter is positioned to measure the net flow rate to the engine, as shown in Figure 2.2.

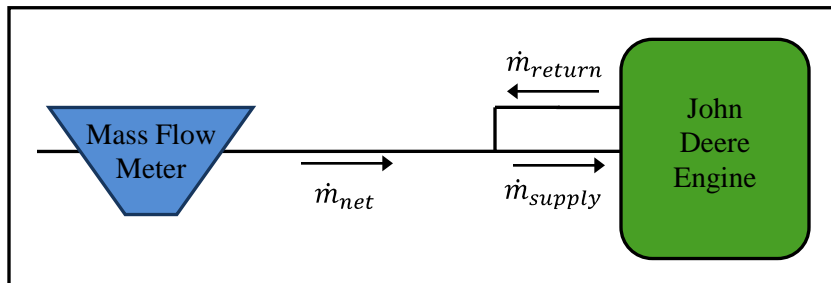


**Figure 2.2 - Mass flow meter configuration.**

According to mass conservation, the mass flow at the node in the figure above is given by:

$$(2.1) \quad \dot{m}_{net} + \dot{m}_{return} = \dot{m}_{supply}$$

where  $\dot{m}_{net}$  is the fuel mass flow rate injected into the cylinder(s),  $\dot{m}_{supply}$  is the mass flow rate of fuel supplied to the fuel injectors, and  $\dot{m}_{return}$  is the mass flow rate of extra fuel leaving the

fuel injectors. After a simple rearrangement, Equation 2.1 is equivalent to:

$$(2.2) \quad \dot{m}_{net} = \dot{m}_{supply} - \dot{m}_{return}$$

Therefore, the net fuel injected into the cylinder is measured by a single mass flow meter immediately upstream of where the return fuel enters the fuel line. This system of measuring the net fuel flow rate was used on both the isolated cylinder and the remaining three cylinders.

All four cylinders were operated on petroleum diesel during warm up, cool down, and after each test to ensure consistency between tests. A remotely controlled three-way valve regulated the fuel source for cylinder 4 between the main diesel tank and a separate, smaller tank containing the fuel of interest. The fuel injection system and instrumentation panel designed and built by the team of seniors is shown in Figures 2.3 and 2.4.

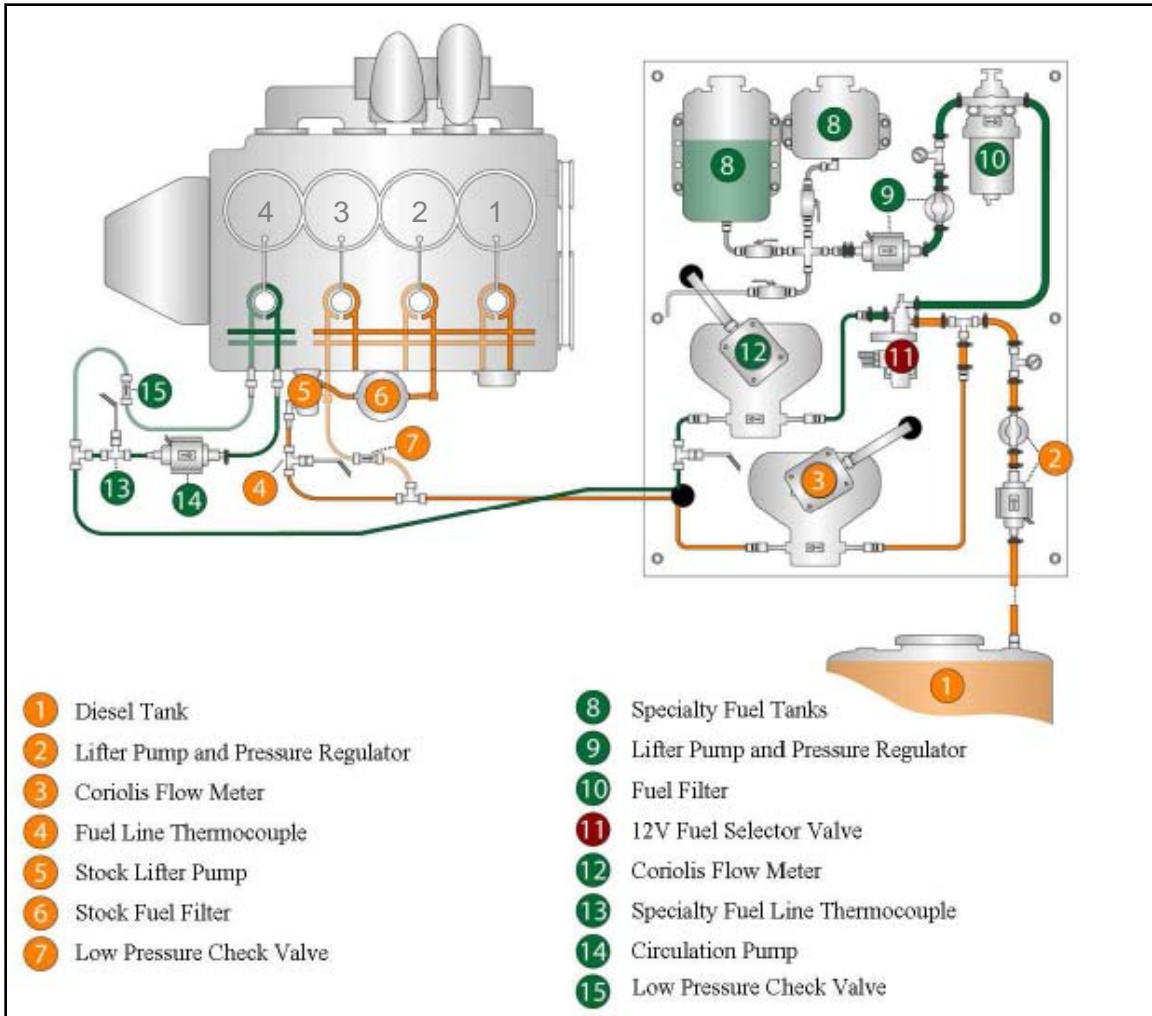


Figure 2.3 - Schematic diagram of redesigned fuel injection system for the 4024T engine

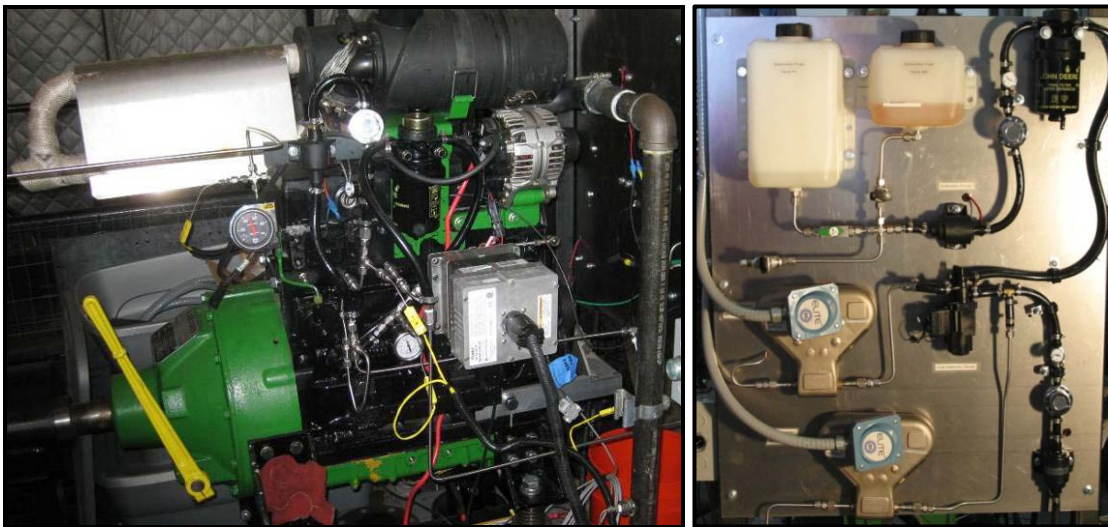


Figure 2.4 - Completed fuel injection system and instrumentation panel.

## 2.2 Exhaust Manifold Modification

To measure the emissions from the isolated cylinder running on the fuel of interest, emissions probes were located in the exhaust manifold upstream of where the exhaust mixed with the gases from the other three cylinders. The gaseous probe and the particulate probe were sized and oriented according to 40 CFR Part 60 and ISO 8178 standards, but all the requirements in these standards could not be met because of geometrical constraints of the exhaust manifold (International Organization for Standards 1996) (EPA 2007). The aforementioned standards require that the probes be inserted eight pipe diameters downstream and two pipe diameters upstream from any disturbance such as a bend or contraction in a straight pipe. This requirement is to ensure that the flow is fully-developed at the probe inlet. Additionally, the exhaust manifold is pressurized due to the turbocharger and the samples are taken much closer to the exhaust ports than is recommended. The pressurization and elevated temperature of the exhaust sample could impact the measurements presented herein. Accordingly, this unconventional setup will make it difficult to compare these results directly with other studies that follow the guidelines set forth in the aforementioned standards. However, since all measurements were taken with the same experimental setup and test protocol, results for the different fuels should be consistent. Moreover, as discussed in Section 5.2.1, the brake specific emissions of all criteria pollutants measured using the technique described above were consistent with previous studies conducted using the same engine (Bennett, 2007; Bennett, et al, 2008).

The orientation of the exhaust probes in the exhaust manifold is presented in Figures 2.5 and 2.6. Four sample probes were installed on exhaust port for cylinder 4, the isolated cylinder, while two probes were used to monitor cylinder 1, the other outer cylinder, for direct comparison against cylinder 4. As shown in Figure 2.5, a probe for all the gaseous measurements, a probe for all the particulate measurements, a thermocouple and a probe for the Cambustion CLD500 Fast NO<sub>x</sub> analyzer were clustered around the exhaust port for cylinder 4. Another Fast NO<sub>x</sub> probe and

thermocouple are located at the exhaust port for cylinder 1. Since cylinder 1 was always operated on petroleum diesel, the temperature and  $\text{NO}_x$  concentration in this cylinder provided a real-time comparison to the specialty fuel exhaust gases from cylinder 4. Heated sample lines carried the exhaust gases from the particulate probe to a dilution tunnel (as described in Section 2.4.4) and from the gaseous probe to the Control Room where a 5-gas analyzer and Fourier Transform Infrared spectrometer are located (as described in Sections 2.4.1 and 2.4.3, respectively). The sample lines are heated to  $110\text{ }^\circ\text{C}$  for the gaseous line and to  $150\text{ }^\circ\text{C}$  for the particulate line to prevent condensation in the exhaust.

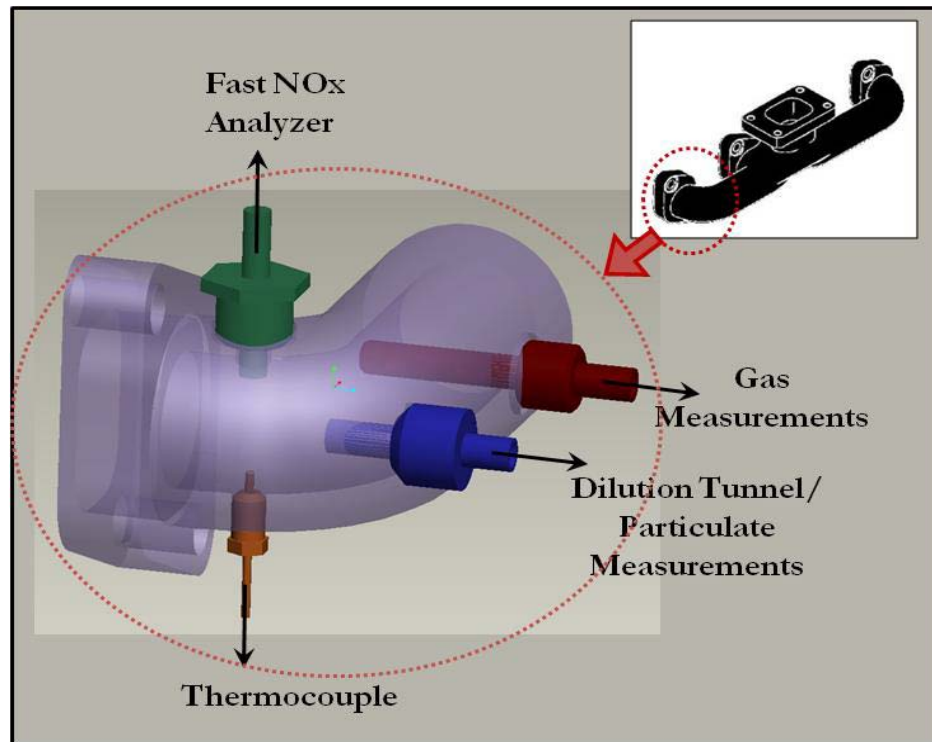


**Figure 2.5 - Schematic of Exhaust Manifold and orientation of sample probes on cylinder 4.**

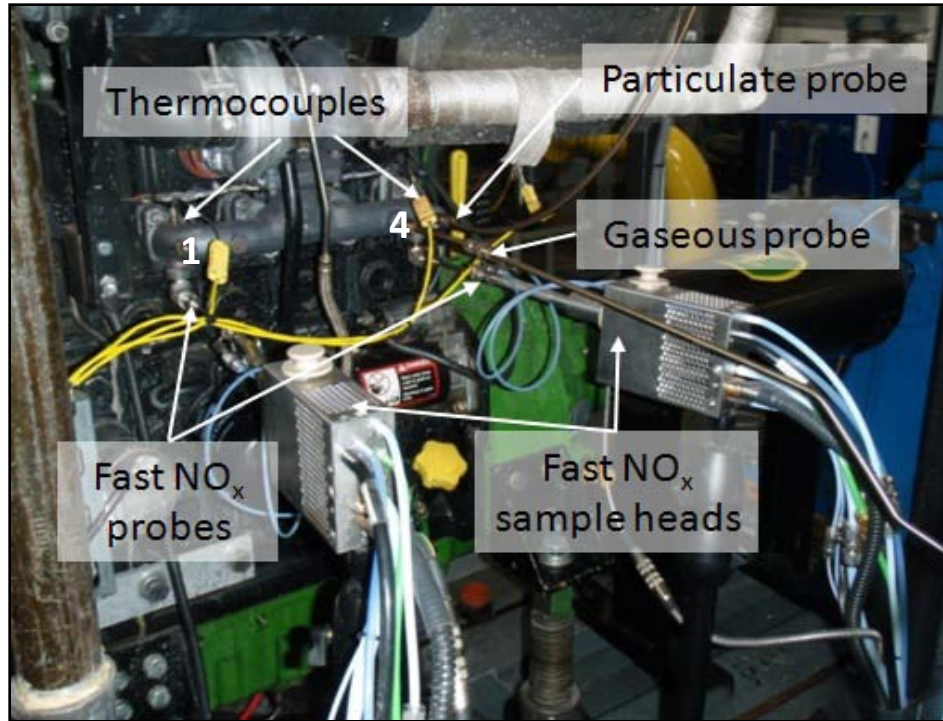


**Figure 2.6 - Photograph of all the probes installed on the exhaust manifold. Cylinder 1 is located on the left; cylinder 4 is on the right.**

## **2.3 Data Acquisition and Control System**

In addition to the exhaust gas measurements, parameters such as oil temperature and turbocharger boost pressure were measured to monitor the engine operating condition and to ensure that the engine was functioning properly. Some systems needed to be controlled by an external controller, such as the three-way valve controlling the fuel source for the isolated cylinder. All of these functions were accomplished using a National Instruments data acquisition system and a LabVIEW program written by the undergraduate student design team.

A Compact RIO (cRIO) 9074 control and data acquisition system made by National Instruments collected all the signals from the various engine monitoring equipment. The cRIO also supplied analog voltage signals for control purposes such as operation of the specialty fuel supply system and the 4024T engine throttle control. Two 32 channel analog input units were used for the thermocouples and pressure transducer signals. A 32 channel 24 V digital input unit

accepted the digital signals from the Micro Motion coriolis meter transmitters. The cooling system and throttle were both controlled with a digital signal, produced by a 24 V digital output module, while the isolated cylinder's three-way valve required an analog signal for control, so a 4 channel analog output module was also needed. All these input and output modules were installed in the cRIO. The electrical box containing all the control modules and associated wiring is shown below in Figure 2.7.

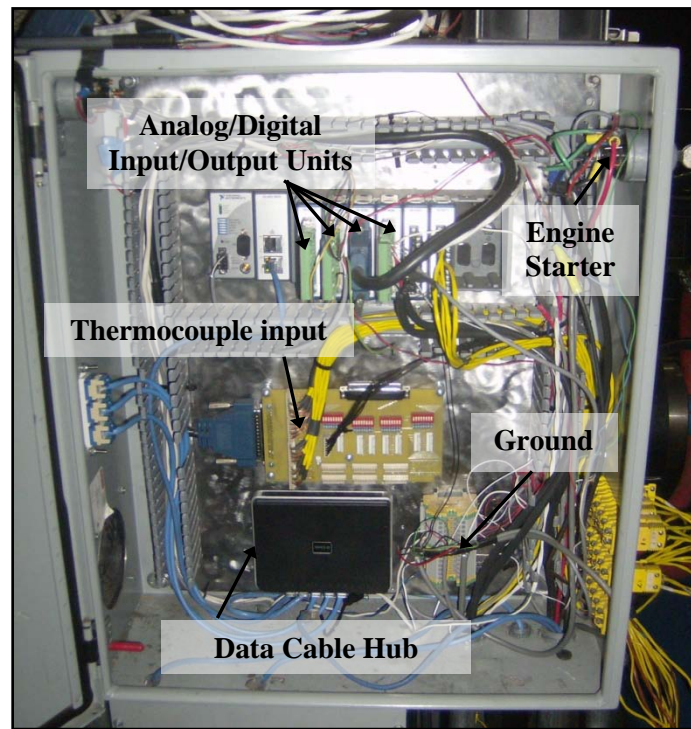


**Figure 2.7 - Electrical control box containing cRIO and associated data acquisition systems.**

All the signals collected by the cRIO were sent to a LabVIEW program that enabled monitoring and data collection at a rate of 4 Hz. The main screen of the LabVIEW program is shown in Figure 2.8. The three buttons in the top left corner turn on the power for the radiator pump and fan, which are components of the engine cooling system, and for the AC power source in the electrical box. The fuel switch at the top was used to change the fuel source for the isolated cylinder. This switch could be actuated while the engine was running. Temperatures are displayed on the right side of the screen. The temperatures near the top of the screen are

associated with the engine, while the bottom four temperatures monitor the cooling system for the engine and dynamometer. The measurements in the center of the screen include the fuel mass flow rates, inlet manifold pressure due to the turbocharger, and the concentration from the Fast NO<sub>x</sub> analyzer. The signals from the coriolis flow meters had a low signal to noise ratio, so for the purposes of monitoring, averaged fuel flow values were also displayed. At the bottom left, the engine speed, power and torque are displayed. All these values are measured by the dynamometer control unit. The throttle control dial is shown in the center at the bottom. This dial controls a voltage signal sent to the throttle control unit attached to the engine. As the voltage increases, the speed also increases. The throttle was used in conjunction with the dynamometer controller to set the load and speed during the tests.

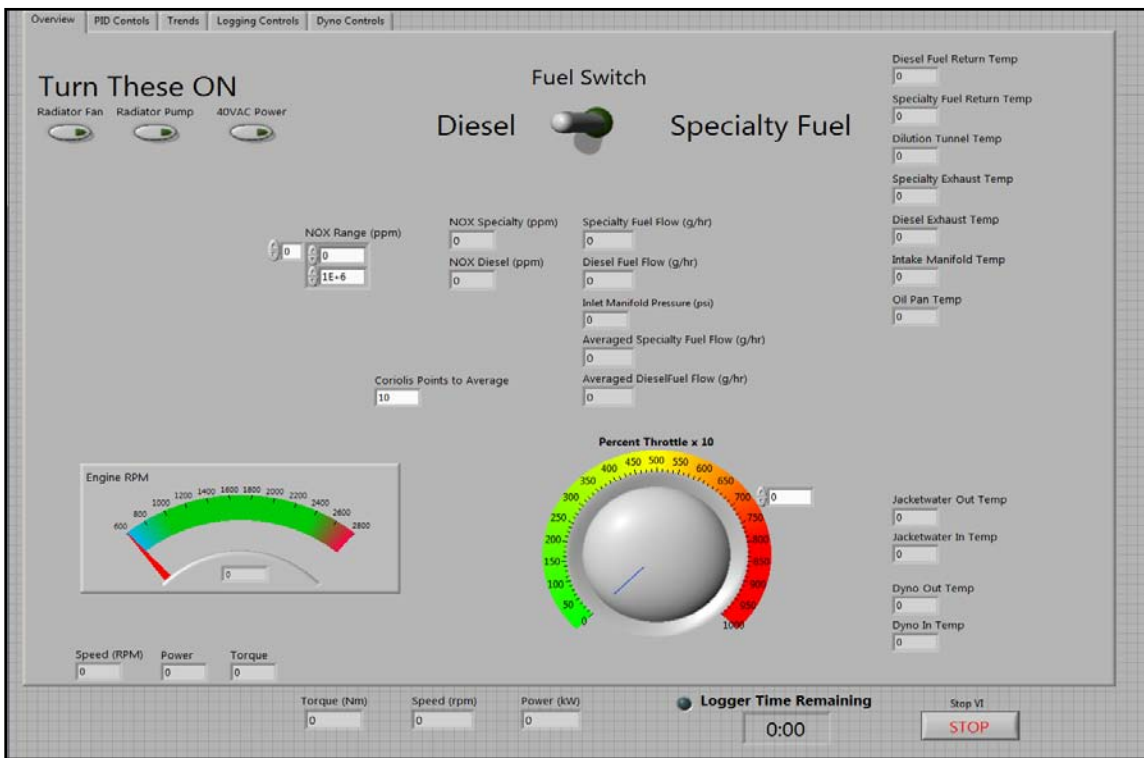


**Figure 2.8 - Main screen of LabVIEW program showing temperatures, pressure, fuel flow rates, and engine speed, power and torque.**

A second LabVIEW program, written by the control room staff, to control the dynamometer was integrated into the program written by the senior design team. The front

screen for that program is shown in Fig. 2.9b. The instrument panel in the program is a replica of the panel on the Dyne Systems Co Dyne-Loc IV dynamometer controller (Fig. 2.9a) and the LabVIEW program functions identically to the dynamometer controller. The dynamometer can be controlled using the LabVIEW program or the physical dynamometer controller. For the tests described here, the LabVIEW instrument panel set the torque produced by the dynamometer and the throttle was adjusted to set the engine speed. Both load and speed were increased incrementally so as not to damage either the engine or the dynamometer.

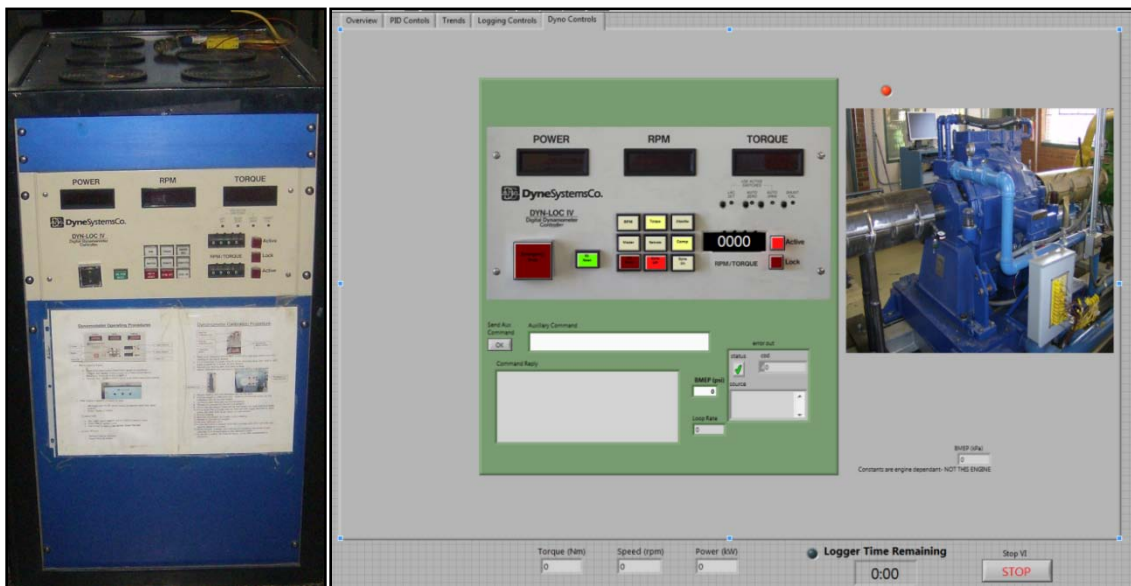


**Figure 2.9 - (a) Dynamometer controller. (b) Dynamometer control screen from LabVIEW program.**

A summary of all the measurement and support equipment used on the engine is provided in Table 2.1 below.

**Table 2.1 - All equipment used to monitor engine and measure properties of the exhaust that were of interest.**

<b>Measurement</b>	<b>Instrumentation</b>	<b>Data Collection System</b>
Exhaust Manifold Temp.	1/16" Type K thermocouple	cRio, main system LabVIEW
Diesel & Isolated Cylinder Fuel Return Temp.	1/8" Type K thermocouple	cRio, main system LabVIEW
Oil Pan Temp.	1/8" Type K thermocouple	cRio, main system LabVIEW
Intake Manifold Temp.	1/8" Type K thermocouple	cRio, main system LabVIEW
Particulate Probe Temp.	1/8" Type K thermocouple	cRio, main system LabVIEW
Engine Coolant In & Out Temp.	1/4" Type K thermocouple	cRio, main system LabVIEW
Dynamometer Cooling Water In & Out Temp.	1/4" Type K thermocouple	cRio, main system LabVIEW
Intake Manifold Pressure	Omega PX181B-030G5V pressure transducer	cRio, main system LabVIEW
In-Cylinder Pressure	Kistler 6056 A pressure transducer	Hi-Techniques Win600 computer
Diesel and Isolated Cylinder Fuel Mass Flow Rate	Micro Motion flow meter CMF010M323NQEZZZ and transmitter 2700R11BBCEZZZ	cRio, main system LabVIEW
Fast NO <sub>x</sub>	Cambustion CLD500 Fast NO <sub>x</sub> analyzer	cRio, main system LabVIEW
Engine Speed	Hall effects rpm sensor	Dynamometer Controller
Engine Torque	Load Cell	Dynamometer Controller
CO concentration	Siemens Ultramat 6 non-dispersive infrared sensor	5-Gas LabVIEW
CO <sub>2</sub> concentration	Siemens Ultramat 6 non-dispersive infrared sensor	5-Gas LabVIEW
O <sub>2</sub> concentration	Rosemount NGA 2000 paramagnetic detector	5-Gas LabVIEW
THC concentration	Rosemount NGA 2000 flame ionization detector	5-Gas LabVIEW
NO concentration	Siemens NOXMAT 600 chemiluminescence detector	5-Gas LabVIEW
NO <sub>2</sub> concentration	Siemens NOXMAT 600 chemiluminescence detector	5-Gas LabVIEW
Other gaseous compounds concentrations	Nicolet Magna 560 Fourier Transform Infrared Spectrometer	FTIR LabVIEW
Dilution Tunnel Inlet Temp.	Type K thermocouple	Dilution Tunnel LabVIEW
Dilution Tunnel Residence Chamber Temp	Type K thermocouple	Dilution Tunnel LabVIEW
Exhaust sample flow rate	Venturi flow meter	Dilution Tunnel LabVIEW
Clean dilution air flow rate	Turbine flow meter	Dilution Tunnel LabVIEW
Particulate Size Distribution	Grimm Technologies Sequential Mobility Particle Sizer	Dilution Tunnel LabVIEW
Organic carbon chemical composition	Aerodyne High-Resolution Time-of-Flight Aerosol Mass Spectrometer	AMS Computer

## **2.4 Exhaust Measurements**

A total of seven instruments characterized the gaseous and particulate components of the engine exhaust. A 5-Gas analyzer measured CO, CO<sub>2</sub>, O<sub>2</sub>, Total Hydrocarbons (THC), NO, NO<sub>2</sub> and NO<sub>x</sub>. A Combustion CLD500 Fast NO<sub>x</sub> analyzer also measured NO, and a Nicolet Magna-560 Fourier Transform Infrared Spectrometer (FTIR) was used to identify larger gaseous compounds. Emissions of total mass were measured gravimetrically via collection on to Teflon filters, and elemental and organic carbon were measured via collection on (and subsequent analysis of) quartz filters. A Grimm Technologies Sequential Mobility Particle Sizer (SMPS) was used to measure particle size distributions from 10 to 1000nm, and an Aerodyne High-Resolution Time-of-Flight Aerosol Mass Spectrometer (AMS) analyzed the chemical composition of organic carbon particles. All the particulate measurements were taken after the exhaust sample was diluted with clean air in a dilution tunnel. In addition to the exhaust measurements, Kistler 6056A high speed pressure transducers recorded the in-cylinder pressure of cylinders 1 and 4. Each of these instruments is described in detail in the following sections.

### **2.4.1 5-Gas Analyzer**

The 5-Gas analyzer measures the following gaseous species found in the exhaust: CO, CO<sub>2</sub>, O<sub>2</sub>, Total Hydrocarbons (THC), NO, NO<sub>2</sub> and total NO<sub>x</sub>. Five separate instruments, which are located in the Control Room, detect each species individually, as shown in Figure 2.10.

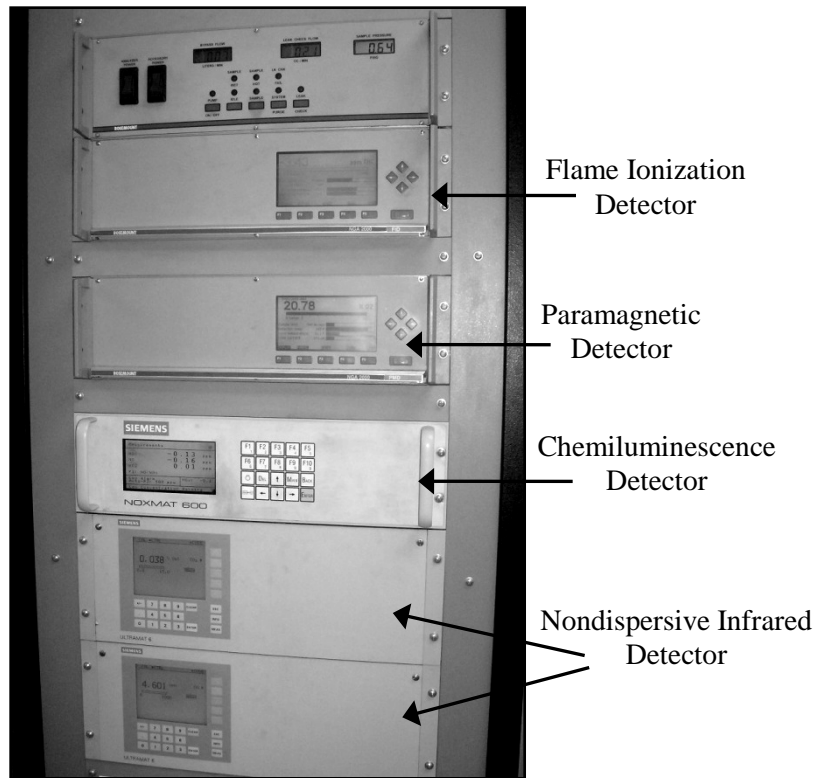


**Figure 2.10 –Rosemount 5-Gas analyzer rack for measurement of CO, CO<sub>2</sub>, O<sub>2</sub>, NO, NO<sub>2</sub>, and THC.**

CO and CO<sub>2</sub> are measured via a Siemens (Munich, Germany) model Ultramat 6 nondispersive infrared (NDIR) sensor. CO and CO<sub>2</sub> absorb slightly different portions of the infrared spectrum and the intensity at which the light is absorbed is proportional to the concentration of CO and CO<sub>2</sub> in the exhaust. A Rosemount (Solon, OH) model NGA 2000 paramagnetic detector is used to measure the magnetic susceptibility of the exhaust, which is proportional to the concentration of O<sub>2</sub> in the exhaust. O<sub>2</sub> is highly paramagnetic and so the magnetic susceptibility of the exhaust is almost entirely due to O<sub>2</sub>. Total hydrocarbons are measured using a Rosemount NGA 2000 Flame Ionization Detector (FID). The exhaust is mixed with H<sub>2</sub> and air and burned. The flame produces ions, creating a current in the detector circuit that is proportional to the number of carbon atoms. The FID used in this experiment was calibrated with methane (CH<sub>4</sub>). Concentrations of NO, NO<sub>2</sub> and total NO<sub>x</sub> are measured individually using a Siemens NOXMAT 600 chemiluminescence detector. In the

chemiluminescence detector, NO is reacted with ozone ( $O_3$ ) and an electronically excited  $NO_2^*$  molecule is formed, which will emit a single photon per molecule. To measure  $NO_2$  in the exhaust, an oxidation catalyst is used to convert all the exhaust gas  $NO_2$  to NO before the reaction with ozone takes place. The chemiluminescence detector alternates between measuring NO and using the oxidation catalyst to measure  $NO_2$ . Other  $NO_x$  species such as  $N_2O$ ,  $N_2O_4$ , etc are not measured but concentrations of these species are negligible in diesel exhaust.

#### **2.4.2 Fast $NO_x$ Analyzer**

A Cambustion CLD500 Fast  $NO_x$  analyzer was used to directly measure the NO in the exhaust manifold locations in the vicinity of the exhaust ports from cylinders 1 and 4, respectively. The same chemiluminescence principle used for detecting NO in the 5-gas analyzer is used in the Cambustion CLD500, but the chemiluminescence reaction occurs in a sample head that is located directly at the sample location resulting in response times on the order of 1 ms. Rather than having to travel through dozens of feet of heated sample line between the engine and the control room to reach the 5-gas analyzer, the sample heads of the Fast  $NO_x$  analyzer (the two stainless steel rectangles with tubes attached, seen in Figure 2.6) are a couple inches away from the exhaust manifold. This allows the fluctuations of  $NO_x$  produced during the combustion cycle to be measured in real time.

#### **2.4.3 Fourier Transform Infrared Spectrometer**

To identify and quantify the concentration of other gaseous compounds in the exhaust, a Nicolet (Madison, WI) Magna 560 Fourier Transform Infrared Spectrometer (FTIR) was used. The FTIR operates similarly to the NDIR used to measure CO and  $CO_2$  in that it measures the spectrum of light absorbed by different gaseous species. The infrared light excites the vibrational/rotational energy modes of the chemical bonds in a molecule and the unique pattern of absorbed light from the entire molecule can be used to identify the chemical species. The FTIR

can measure the entire infrared spectrum simultaneously using an interferometer. The interference pattern generated by the interferometer is analyzed by applying a Fourier Transformation, which results in a plot of the absorbance versus wavelength. This absorbance map is used to determine species and concentration, as the intensity of light absorbed is proportional to the concentration of the species present in the exhaust. Some of the hazardous air pollutants (HAPs) measured with the FTIR include formaldehyde, acrolein, acetaldehyde, ammonia, and hydrogen cyanide.

#### 2.4.4 Dilution Tunnel

To better simulate tailpipe exhaust and allow time for the complex agglomerates of carbon particles to stabilize, all the particulate measurements were taken after the exhaust passes through a dilution tunnel. The dilution tunnel mixes the exhaust with clean ambient air and includes a residence chamber that allows the particles to age.

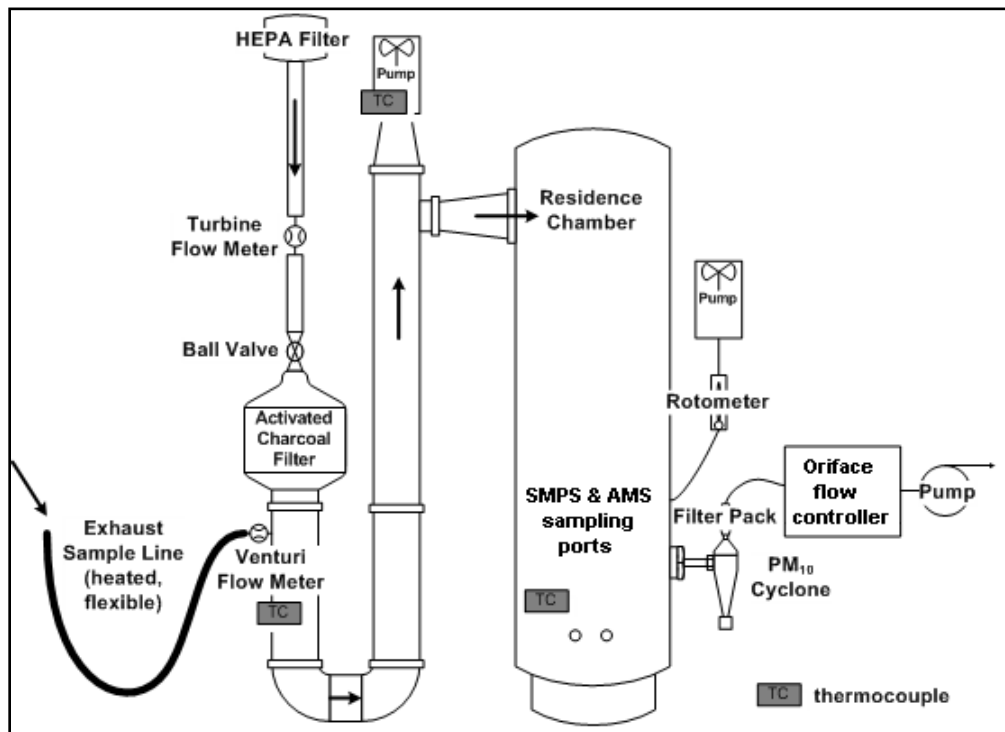


Figure 2.11 – Schematic diagram of dilution tunnel (Bennett, et al. 2008).

A heated sample line, set at 150 °C, delivered the exhaust sample to the dilution tunnel and prevents the gases from condensing while en route. A Venturi flow meter, also heated to 150°C, is used to measure the flow rate of the exhaust air sample entering the dilution tunnel by relating the pressure drop across an orifice to volumetric flow. The dilution air is first cleaned by a HEPA filter, followed by an activated charcoal filter to ensure that the dilution air is free of particles that may be present in the ambient air. A turbine flow meter is used to measure the flow rate of clean dilution air. A LabVIEW program associated with the dilution tunnel converts both flow rates to actual liters per minute (ALPM), calculates the dilution ratio, and records the temperatures of the sample line, the Venturi flow meter, the pump pulling air into the tunnel, and the residence chamber. A ball valve located downstream of the turbine flow meter is used to make minor adjustments in the dilution ratio. Since the probe location in exhaust manifold of the 4024T engine (as described above) was at a pressure higher than that of a typical exhaust sample location, the dilution ratio that could be achieved in the present study was slightly lower than previous tests with the same engine and dilution tunnel (Bennett, et al. 2008). Specifically, the tests conducted by Bennett and coworkers (2008) employed a dilution ration of 50:1, whereas for the tests presented herein, a dilution ration of 40:1 was achieved.

For the present study, at the higher loads, the turbocharger produces a higher pressure resulting in increased sample flow rate thereby decreasing the dilution ratio. To keep the dilution ratio constant at 40:1 for both engine loads, the ball valve was closed slightly at the lower load. A pump was used to discharge air and exhaust from the residence chamber to control the residence time in the tunnel. For tests reported in this thesis, a valve and rotameter combination was set to allow 200 scfm of air and exhaust out of the tunnel. All of the particulate measurements were taken from the bottom of the residence chamber so that the dilution and aging of the particles would be complete before sampling.

#### 2.4.5 Particulate Matter Filter Measurements

Two filter sampling sets, each including a PM<sub>10</sub> aluminum cyclone, a dual-stage stainless steel filter pack, a standard air rotameter and a critical orifice, were used to collect particulate matter. The cyclones use centripetal force to trap all particles larger than 10 µm in diameter, leaving all the particles smaller than 10 µm in the sample line, denoted as PM<sub>10</sub>. This size is significant because this is the cutoff for thoracic particles that penetrate into and beyond the bronchial region of the lungs (Hinds 1999). The cyclones also prevent a few large particles from biasing the mass measurements. The 0.081 inch diameter critical orifices were used to keep the volumetric flow rate constant at 28.3 LPM by choking the flow. This flowrate is required to ensure that the cut point for the cyclones is 10 µm, as intended. The rotameters were used to monitor the volumetric flow rate to ensure that the flow remained choked at the critical orifice.

Within the stainless steel filter packs, the filters are held in 47 mm Delrin filter cassettes that can be removed in between tests. There must be two filter cassettes in each filter pack during testing for the filter pack to seal properly. The two filter sampling lines were used to make two separate measurements on the particulate matter present in the exhaust: total mass and elemental and organic carbon content. Figure 2.12 shows the setup for the filter packs and cyclones and a photograph of the pair of instruments attached to the dilution tunnel.

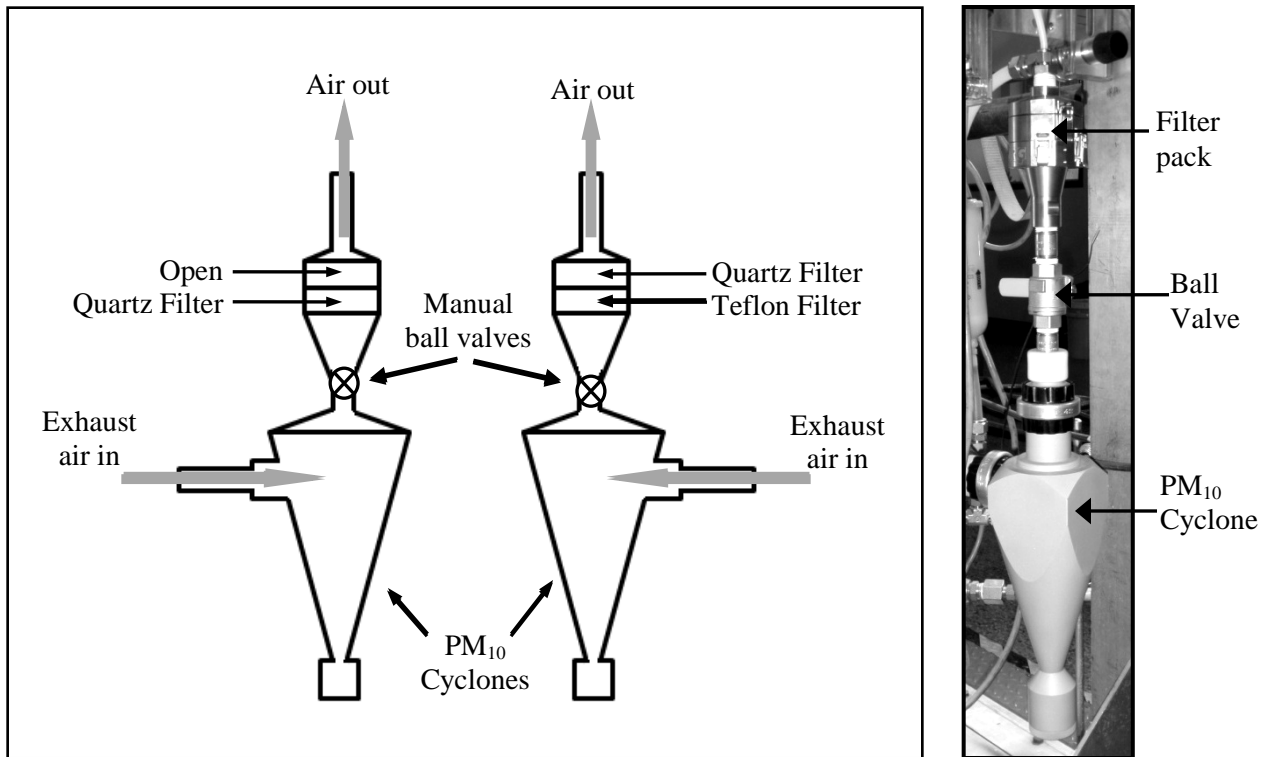


Figure 2.12 - (a) Filter pack set up. (b) Photo of one cyclone and filter pack line.

A Teflon filter was used to measure the total mass concentration in the exhaust. The Teflon filters had a diameter of 46.2 mm (Whatman Co., Kent, UK) and were purchased from Fisher Scientific (Waltham, MA). The filters were weighed before and after sampling to find the mass of the particulates on the surface of the filter. To quantify the small amount of particulate matter collected, a Mettler Toledo (Columbus, OH) MX5 microbalance (shown in Figure 2.13) was used to weigh the filters, accurate to  $\pm 1$  microgram. The filters were weighed hours after sampling was completed, to give the filters time to equilibrate to the weighing room conditions. All mass measurements were taken three times for each filter, before and after sampling.



**Figure 2.13 - Microbalance used to weigh the Teflon filters.**

In the other filter pack, a quartz filter collected particulate matter for elemental and organic carbon (EC/OC) characterization. The quartz filters were cut from a sheet of Pallflex Tissuquartz (Pall Gelman, Ann Arbor, MI) sheets and baked at 550 °C for 12 hours to remove any carbon. To keep the filters clean until testing, they were stored in a glass jar and sealed with aluminum foil; both the glass jar and foil were baked with the filters.

Quartz filters were used because the analysis of the EC and OC in the particulate matter requires the filter to be heated to temperatures higher than the Teflon filter could withstand. Two known sources of error when collecting organic carbon samples are the evaporation of particulate organic carbon from the surface of the filter (negative artifact) and the adsorption of gas-phase organic carbon on to the filter (positive artifact). Since evaporation is more likely if the concentration of OC in the exhaust air decreases, the positive artifact is the more significant effect since the exhaust concentration remains relatively constant during the sampling period. To account for the positive artifact, a second quartz filter sat behind the Teflon filter in the first filter pack to simulate the adsorption of gas-phase organic carbon. The Teflon filter is assumed to catch all of the particles in the exhaust and so any OC found on the backup quartz filter is adsorbed gaseous organic carbon. The results from the backup quartz filter were used to correct the organic carbon measurement from the main quartz filter.

The analysis of the elemental and organic carbon was conducted on a Sunset Labs OC/EC Analyzer (Forest Grove, OR), in collaboration with the CSU Department of Atmospheric Science. The Sunset Analyzer uses thermal evolution and optical transmission to quantify both the EC and OC content on the filter. To perform each analysis, a 2.27 cm<sup>2</sup> circular punch was taken from the quartz filter and inserted into the Sunset Analyzer using tweezers. The punch and tweezers were rinsed with isopropyl alcohol in between samples.

The analysis began by volatilizing the organic carbon in a pure helium environment at 870 °C. The temperature was reduced to 450 °C and the volatilized OC was oxidized to CO<sub>2</sub> so that it can be measured by an NDIR detector. This is the same method used by the 5-Gas analyzer to measure CO<sub>2</sub>. Optical transmission through the filter is monitored using a pulsed Helium-Neon (He-Ne) laser and photodetector. The transmissivity of the filter is used to correct for char that can form at temperatures above 300 °C and affect the carbon measurements. Char is strongly absorbent in the infrared region and so would affect the measurements of the NDIR. As the OC is volatilized, the transmittance of the filter decreased. The second stage of the analysis targets the elemental carbon by introducing 10% oxygen to the flow at a temperature of 860 °C. The elemental carbon burned off the filter and was also oxidized to CO<sub>2</sub> and measured with the NDIR. As the EC burns, the filter transmittance increased and the point at which the transmittance was equal to the original transmittance is defined as the split between elemental and organic carbon. After all the elemental carbon has been burned off the filter, the instrument was calibrated using methane and any needed corrections are integrated into the internal calculations. The results from the Sunset Analyzer are reported in terms of µg of carbon for both elemental and organic carbon. Figure 2.14 shows a sample analysis cycle for the Sunset Analyzer, including temperature, transmittance, and CO<sub>2</sub> from the carbon on the filter.

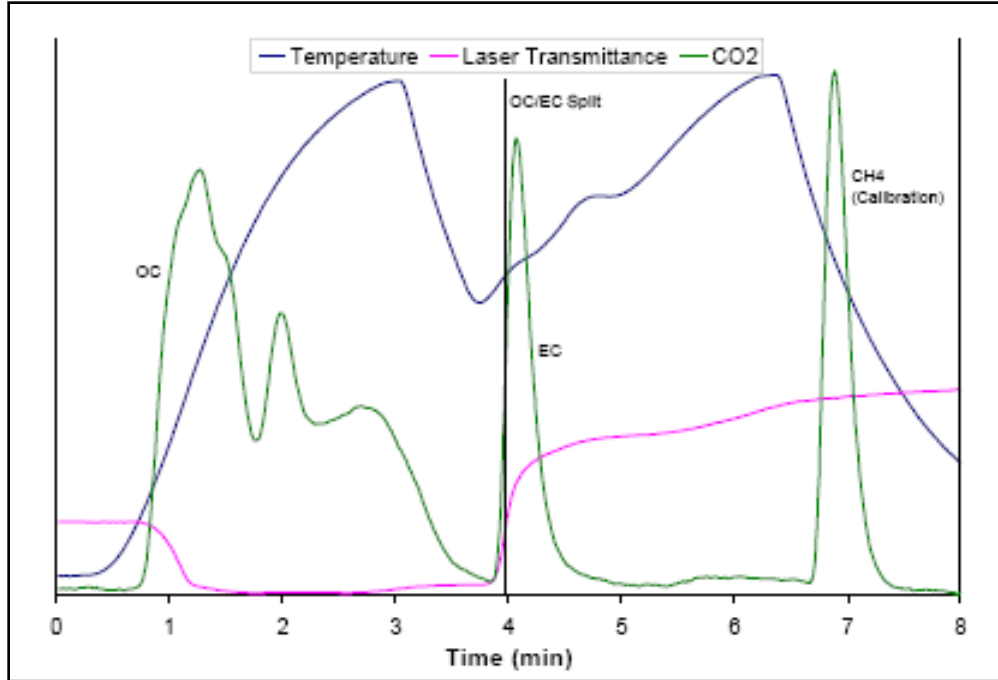


Figure 2.14 - Sample analysis cycle for Sunset Analyzer, reprinted with permission of the author (Holden 2008).

#### 2.4.6 Sequential Mobility Particle Sizer

The Sequential Mobility Particle Sizer (SMPS), built by Grimm Technologies, Inc. (Douglasville, GA) is a device that charges particles prior to entering a variable electric field that is used to determine the size distribution of an aerosol. The SMPS is comprised of two devices in series: a differential mobility analyzer (DMA) and a condensation particle counter (CPC). The DMA pulls 0.3 LPM of aerosol where it is immediately subjected to an impactor that prevents all particles larger than 1  $\mu\text{m}$  from entering the SMPS (as shown in Figure 2.15). The remaining aerosol then enters a polonium ( $^{210}\text{Po}$ ) neutralizer where it receives a Boltzmann charge distribution. In the main chamber of the DMA, clean sheath air flows around a charged central rod. The positively charged aerosol is then sorted according to its mobility, a combination of mass and charge, by varying the voltage on the central rod. Electrical mobility,  $Z$ , is given by:

$$(2.3) \quad Z = \frac{V_{TE}}{E} = \frac{neC_c}{3\pi\eta d}$$

where  $V_{TE}$  is the terminal electrostatic velocity (equivalent to terminal velocity due to gravity),  $E$  the electric field,  $n$  the number of charges on the particle,  $e$  the elementary charge,  $C_c$  the Cunningham slip correction factor,  $\eta$  the viscosity of the air or fluid the particle is in, and  $d$  the particle mobility diameter.

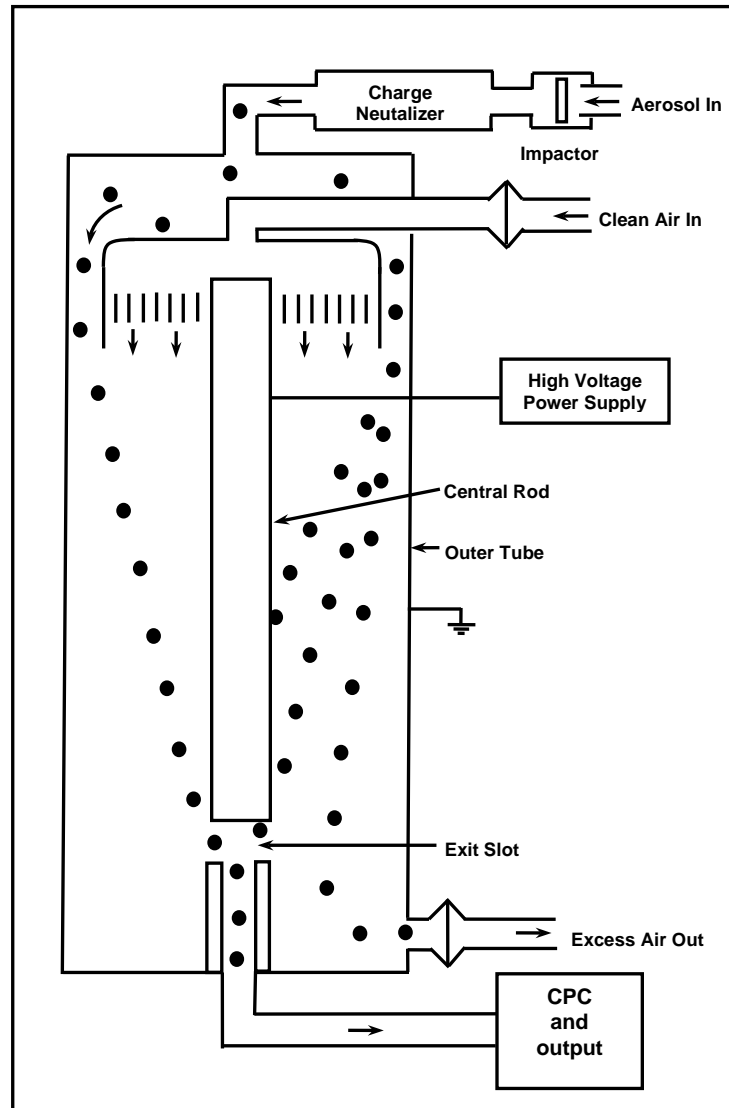


Figure 2.15 – Schematic diagram of the Differential Mobility Analyzer (DMA).

If the mobility of a particle is too large, it will impact on the central rod but if the mobility is too small, it will pass through the chamber and exit with the excess air. Only a small range of particle mobility will be able to exit through the sample port. The voltage on the central rod is varied to classify the particles into 44 size bins between 1  $\mu\text{m}$  and 10 nm. Upon exiting the

DMA, the particles are monodisperse of a known size, but their concentration is still unknown. To quantify the concentration, the particles enter the CPC and are saturated in butyl alcohol vapor. The particles and alcohol vapor enter a condenser and are cooled so that the vapor condenses on the particles, increasing their size. The larger size enables them to be counted with a photodetector using scattered laser light. The combination of DMA and CPC allows very small particles to be sized based on mobility and counted.

The SMPS assumes that each particle receives a single charge but it is possible for particles, especially the larger ones, to acquire multiple charges in the neutralizer. The software associated with the SMPS uses a transfer function to adjust for the possibility of multiple charges, but this correction works best for particles less than 0.1  $\mu\text{m}$ .

Several size distributions were recorded by the SMPS for each fuel type as well as size distributions for the ambient lab air and the clean dilution air flowing through the dilution tunnel. The lab air scans and dilution air scans were used to help quantify any contamination from these sources that could affect results from the engine exhaust.

#### **2.4.7 Aerosol Mass Spectrometer**

The Aerodyne High-Resolution Time-of-Flight Aerosol Mass Spectrometer (AMS) contains a high-resolution time-of-flight mass spectrometer that can characterize the elemental composition of the organic carbon content of particulate matter. The specific chemical breakdown of the exhaust products provides more insight on particle composition from the combustion of different fuels. The exhaust sample from the dilution tunnel passes through a  $\text{PM}_{2.5}$  cyclone (3 LPM, URG-2000-30ED) and a critical orifice, restricting the flow to 0.1 LPM, before entering the AMS. The sample is then concentrated into a narrow particle beam using an aerodynamic lens and accelerated into a vacuum. The particles travel at speeds dictated by their vacuum aerodynamic diameter and the time it takes the particles to cross the Particle Time of Flight (PToF) region is used to determine their size distribution. A rotating mechanical chopper

determines the starting point for the time of flight, which ends when the particles are detected by the mass spectrometer. The chopper can also be used to block all incoming particulates so that a background scan can be performed. After passing through the PToF region, the particles impact on a resistively heated surface used for vaporization. The temperature of the vaporization surface, set at 600 °C, is low enough that only volatile and semi-volatile species can be vaporized; soot and metals will not. In addition to the volatile organic carbon species that are vaporized by the heated surface, other inorganic species are also be vaporized, such as nitrates, sulfates, and ammonium. The vapor then is ionized using electron ionization at 70 eV. From here, the ions enter the time of flight mass spectrometer (ToF MS) region.

The ToF MS region contains an electric field, which directs the ions in one of two paths towards the detector. Ions with the same charge will ideally have the same kinetic energy, so their velocity depends only on the different mass-to-charge ratio ( $m/z$ ) of the ions, resulting in different velocities for different  $m/z$  ions. The time of flight through a known distance distinguishes ions of different  $m/z$ . The particles can be accelerated in either V mode or W mode toward the detector. The V mode is shorter and so there are less ion losses, which means that V mode operation is more sensitive to lower concentrations of ions. Alternatively, the W mode creates a longer path for the ions to travel so differences in mass-to-charge ratio can be distinguished with a higher resolution.

The precision at which the mass is measured allows the vaporized species to be identified. During the vaporization process, the larger organic carbon molecules break apart into smaller fragments. Part of the difficulty of interpreting the results from the mass spectrometer is that the species identified based on their mass are only fragments of the original molecules. Accordingly, some deduction is involved with determining the correct combination of atoms that will correspond to the mass detected by the AMS, and even further supposition is required to determine the parent molecule(s) responsible for the presence of these fragments. Even though

the analysis is complex, significant detail can be garnered about the volatile components of the particulate matter.



**Figure 2.16 - Aero-dyne High-Resolution Time-of-Flight Aerosol Mass Spectrometer.**

#### **2.4.8 Pressure Transducer**

Kistler model 6056A (Amherst, NY) pressure transducers were mounted in the glow plug site in cylinders 1 and 4 of the John Deere 4024T engine to measure instantaneous in-cylinder pressure during the combustion cycle. The in-cylinder pressure measurements were used to calculate the apparent heat release rate (J/deg) and to measure the indicated power (kW) for both cylinders. The latter measurement is critical for converting the exhaust gas concentrations into brake specific mass emissions. Specifically, it cannot be assumed *a priori* that the specialty fuel cylinder produces the same power as the petroleum fuel cylinders. Rather, when cylinder 4 is running on a different fuel than the rest of the engine, it will likely not produce the same power as the others.

The pressure transducer measures pressure at every half angle of the crank shaft, recording 720 data points, for every revolution of the engine. The pressure and crank angle data are recorded on a Hi-Techniques (Madison, WI) Win600 high-speed data acquisition system, which records 1000 cycles of pressure/crank angle data in each set for subsequent time-averaging. The pressure versus crank angle data can be converted to a pressure versus volume data set, which is used to find the indicated power of each cylinder, as well as apparent rate of heat release and mass fraction burn data for each cycle. The net heat release rate is given by:

$$(2.4) \quad \frac{dQ_{net}}{d\theta} = \frac{\gamma}{\gamma - 1} P \frac{dV}{d\theta} + \frac{1}{\gamma - 1} V \frac{dP}{d\theta} = \frac{dQ_{chem}}{d\theta} - \frac{dQ_w}{d\theta},$$

where  $\gamma$  is the specific heat ratio of air,  $P$  is the pressure as measured by the high speed pressure transducer,  $V$  is the volume in the cylinder at that angle,  $\theta$ ,  $\frac{dQ_{chem}}{d\theta}$  is the chemical heat release rate of the fuel, and  $\frac{dQ_w}{d\theta}$  is the heat transfer rate to the walls of the cylinder. The heat transfer rate to the walls is given by:

$$(2.5) \quad \frac{dQ_w}{d\theta} = \frac{1}{2\pi N} h(\theta) A_w(\theta) \cdot [T - T_w],$$

where  $N$  is the speed of the engine in revolutions per second,  $h(\theta)$  is the convective heat transfer coefficient defined by the Woschni correlation,  $A_w(\theta)$  is the exposed surface area of the combustion cylinder (at crank angle  $\theta$ ),  $T$  is the average gas temperature and  $T_w$  is the wall temperature. The Woschni correlation is given by:

$$(2.6) \quad h(\theta) = 3.26 \cdot P^{0.8} U^{0.8} B^{-0.2} T^{-0.55},$$

where  $P$  is the instantaneous pressure in the cylinder,  $U$  the average cylinder gas velocity,  $B$  the bore of the cylinder, and  $T$  the gas temperature in the cylinder (Heywood 1988). The gas temperature and gas velocity are calculated using the ideal gas law and some engine operation parameters.

### **3. FUEL PRODUCTION AND ANALYSIS**

The fuel used for testing was obtained from a variety of sources. The ultra low sulfur diesel (ULSD) was purchased from Team Petroleum in Fort Collins, CO.

The soy biodiesel was donated by Blue Sun Biodiesel, from Golden, CO. The B100 biodiesel that is sold at gas stations in the area contains a number of additives to prevent bacterial growth and gelling in cold weather. A five gallon container of pre-additive B99 Soy biodiesel was donated for this test so that the soy biodiesel results would not be affected by the presence of any additives. Tests were performed within several days of receiving the pre-additive B99 to minimize the possibility of biological or oxidative instability of the fuel.

The canola biodiesel was made from store-bought Wesson pure Canola oil and transesterified with potassium hydroxide and methanol. The potassium hydroxide tablets and methanol were purchased from the Colorado State University Chemistry Stockroom. The canola oil was converted to biodiesel in two gallon batches in a large scale reactor (Figure 3.1) built for this project.

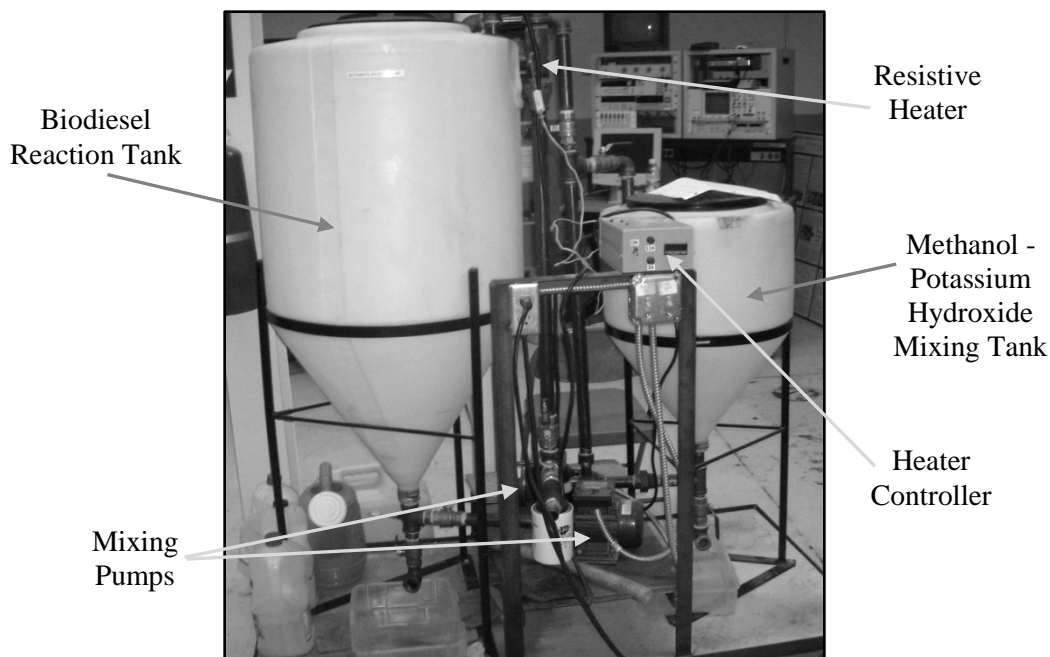


**Figure 3.1 - Large scale biodiesel reactor in the EECL.**

The raw biodiesel was washed several times with water and then was drained through a dry wash resin to ensure that all the water and glycerin were removed from the biodiesel. The resin, Thermax T-45 BD Macroporous Resin purchased from Arbor Biofuels Company (Ann Arbor, MI), is a solid catalyst designed to remove glycerine, soaps, and the potassium hydroxide catalyst from the crude biodiesel.

After contacting a number of algae-for-fuel companies about obtaining a small sample of their algal biodiesel without success, our focus changed to finding a way to simulate algal oil. Chemical supply companies, such as Sigma-Aldrich, sell pure methyl esters for a variety of fatty acids. It would have been possible to buy all the different constituents of a known algal oil profile and assemble the exact profile, but the price would have been exorbitant. A suitable and affordable solution was to use fish oil as the source for the long, highly unsaturated fatty acids that make algal oil so unique. Fish acquire the same highly unsaturated fatty acids from ingesting algae, so fish oil is very similar to algal oil. The pharmaceutical grade fish oil, purchased from Jedwards International (Quincy, MA), was transesterified using the same process as the canola

oil, but in smaller batches. The dry resin used with the canola oil reacted badly with the fish oil methyl ester and so was not used. When transesterification is done on a smaller scale, it is possible to wash and dry the biodiesel with more precision and eliminate the need for the dry resin. A thorough water-washing of the crude biodiesel removes all the impurities that the dry resin is designed to capture. Using fish oil as the main ingredient, two “algal” fuels were made by mixing the fish oil biodiesel with other methyl esters.

### **3.1 Simulating Algal Oil**

The main difference between algal oil and other vegetable oils that are currently used for biodiesel is the long, highly unsaturated fatty acid content. Currently, fish oil is more obtainable than algal oil and has a similar fatty acid composition to that of algal oil. Indeed, fish oil is one of the few oils that contain measureable amounts of EPA and DHA, which are the two most common PUFAs seen in algal oil. However, since the fatty acid composition of the fish oil is not identical to algal oil, pure methyl esters were added to the transesterified fish oil to produce “synthetic” algal methyl ester formulations with a fatty acid composition very similar to that which would be produced from transesterifying algal oil triglycerides.

A five gallon batch of pharmaceutical grade fish oil was purchased from Jedwards International Inc. (Quincy, MA). This oil was transesterified in small batches to ensure that the oil was fully reacted and properly washed. Pure methyl esters were obtained as free samples from Procter & Gamble’s chemical division (Cincinnati, OH). Palmitic acid methyl ester (C16:0) and Oleic acid methyl ester (C18:1) were added to the fish oil biodiesel in two different ratios to simulate two types of algal oil.

The plots below show the two fuels, with the profile of the algal oil in red and the profile of the fish oil mixture intended to duplicate the algal oil in blue.

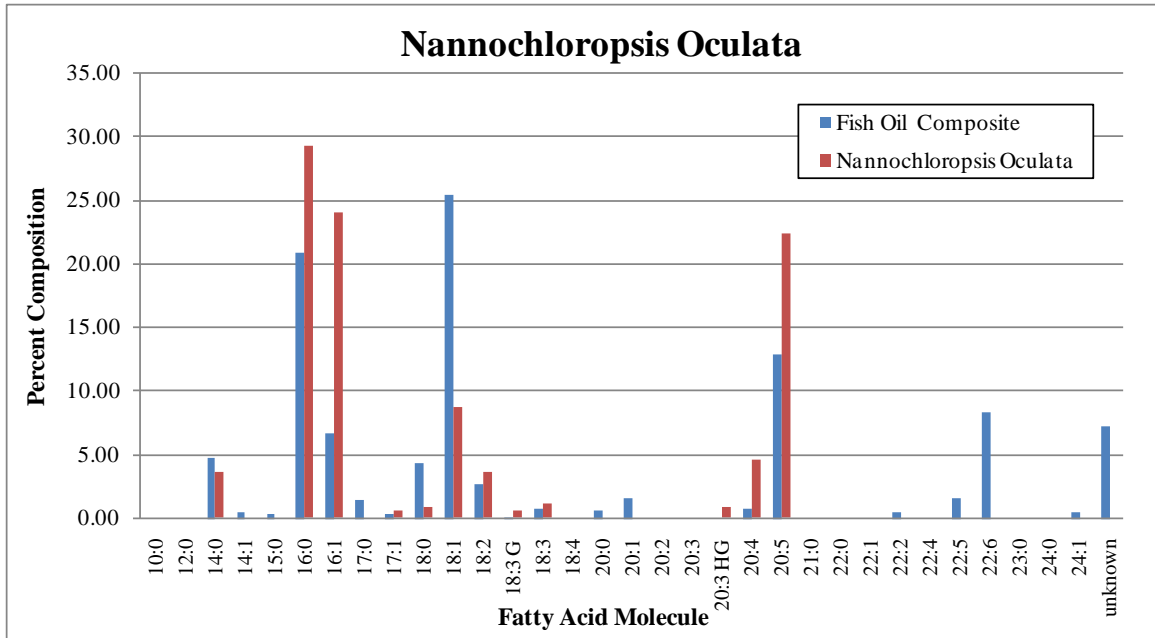


Figure 3.2 - Fatty Acid profile for algae strain *Nannochloropsis Oculata* and the fish oil mixture used to simulate it.

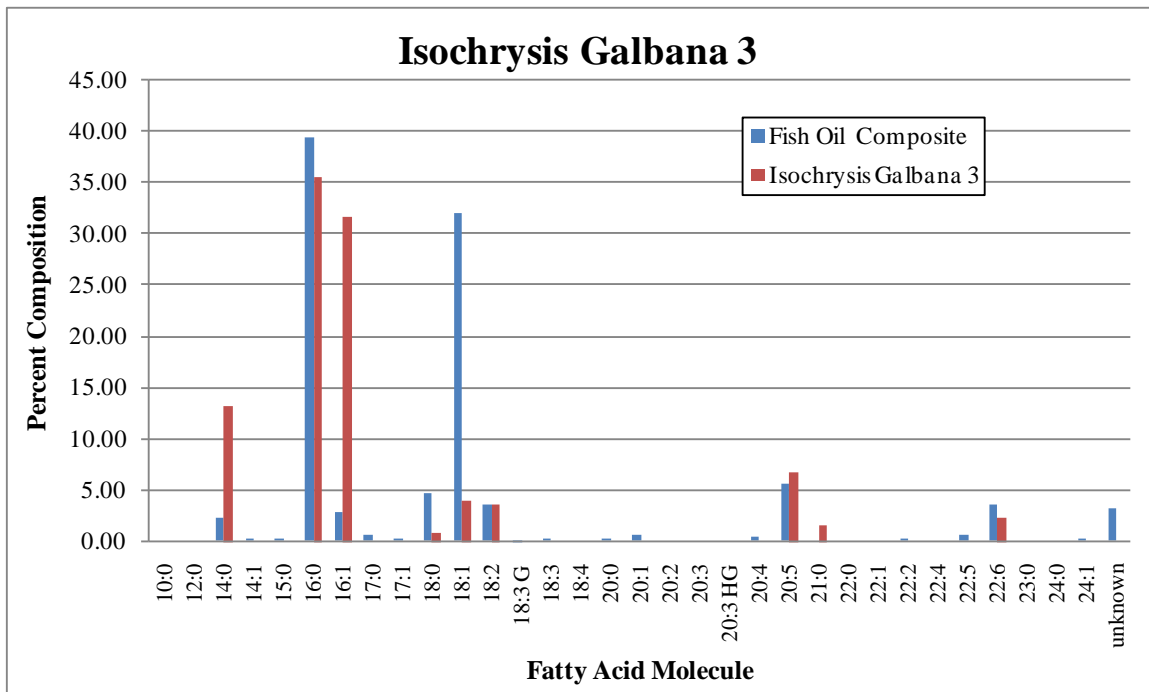


Figure 3.3 - Fatty Acid profile for algae strain *I. Galbana* and the fish oil mixture used to simulate it.

The algae shown in Figure 3.2 is *Nannochloropsis Oculata*, a species of algae grown by Solix Biofuels Inc., a Ft. Collins, CO algae-for-fuel company which spun out Colorado State

University. The fatty acid composition for *Nannochloropsis Oculata* was provided by Solix Biofuels. In Figure 3.3, the profile for a species of algae called *Isochrysis Galbana* is shown; where the “3” in the name indicates that the oil was produced in the late stationary phase of growth (Fernandez-Feiriz, et al. 1989). This profile was chosen as the second algae because it contains about 10% highly unsaturated fatty acids by volume, which is half the amount of highly unsaturated fatty acids found in *Nannochloropsis Oculata*. By simulating two “algal” methyl ester biodiesel formulations that contain a range of highly unsaturated fatty acids, it may be possible to see a trend for how these molecules affect emissions.

The fish oil mixtures are intended to simulate the algal oils shown in Figures 3.2 and 3.3, but the fatty acid profiles do not exactly match. Both EPA and DHA are present in the fish oil, but *Nannochloropsis Oculata* only contains EPA. Also, some fatty acid methyl esters found in algae, such as Palmitoleic acid methyl ester (C16:1), are difficult to find in pure form because they do not exist in high concentrations in other vegetable oil feedstocks. The research done by Grabowski, et al. and Allan, et al. indicated that the number of double bonds in oil has a greater effect on emissions than chain length, so the profiles were matched based on the number of double bonds. Consequently, the monounsaturated Oleic acid methyl ester (C18:1) was used as a substitute for monounsaturated Palmitoleic acid methyl ester, rather than saturated Palmitic acid methyl ester (C16:0). Table 3.1 shows the different oils, compared by percent volume based on number of double bonds. This form of comparisons shows much better agreement between the algal oil and the fish oil composite.

**Table 3.1 - Fish Oil Mixtures compared to Algal Oil, percent volume based on number of double bonds.**

	<b>Nanochl. Occul.</b>	<b>Composite</b>	<b>Iso. Galbana</b>	<b>Composite</b>
<b>Cx:0</b>	33.78	32.39	51.40	47.37
<b>Cx:1</b>	32.84	34.96	35.69	36.05
<b>Cx:2</b>	3.55	3.17	3.64	3.84
<b>Cx:3</b>	2.32	0.78	0.00	0.33
<b>Cx:4+</b>	22.39	23.55	9.25	10.09

Even though fish oil is more easily obtainable than algal oil, it was not practical to buy and transesterify the amount of fish oil needed to make both “algal” biodiesels and run the entire engine for the period of time needed to complete all the emissions tests. The engine modification described in previous sections allowed the biodiesel requirements for all feedstocks to be reduced by a factor of 4, thereby reducing the amount of fish oil biodiesel needed to a reasonable volume.

## **4. EXPERIMENTAL PROCEDURES**

### **4.1 Test Matrix**

For this study, the 4024T John Deere engine was operated at rated speed (2400 RPM) at two different loads (80 N-m and 115 N-m), which correspond to 50% and 75% of the maximum torque at rated speed. Nine different fuel formulations were tested:

- Ultra low sulfur diesel (ULSD),
- Soy methyl ester biodiesel (Soy B100),
- 20% soy methyl ester/80% ULSD (Soy B20),
- Canola methyl ester biodiesel (Canola B100),
- 20% canola methyl ester/80% ULSD (Canola B20),
- Algal methyl ester #1 (Algae 1 B100),
- 20% algal methyl ester #1/ 80% ULSD (Algae 1 B20),
- Algal methyl ester #2 (Algae 2 B100), and
- 20% algal methyl ester #1/ 80% ULSD (Algae 2 B20).

Algal methyl ester 1 and 2 were formulated to match the fatty acid compositions of *Nannochloropsis Oculata* and *Isochrysis Galbana* 3, respectively. Figure 4.1 shows a sample of the ULSD and each of the 100% methyl ester fuels. Each of the load points was repeated twice for each fuel.



Figure 4.1 - Samples of red diesel and B100 biodiesels used in tests.

## 4.2 Testing Procedures

Before warming up the engine, the dynamometer was calibrated at the beginning of every test day. Without any load on the engine, the zero torque point was checked and re-zeroed, if necessary. A 50 lb weight was hung from the lever arm of the dynamometer, which corresponded to 89 N-m of torque, a little less than half the maximum torque for the 4024T engine. Then an additional 70 lbs was added to the lever arm producing 212 N-m of torque, which is the upper limit on torque for the 4024T engine. Loading and unloading was simulated by pulling up on the lever arm and pushing down, respectively. The torque measured by the dynamometer load cell was recorded for each set of weights after loading and unloading and the load cell was recalibrated if necessary.

Once the calibration on the dynamometer was verified, the engine was operated with all four cylinders operating on ULSD at 2400 rpm and 50% load (80 N-m) for 30 minutes prior to the start of each test. Cylinder 4 was then switched to draw fuel from the specialty fuel reservoir and the engine was operated for another ten to fifteen minutes, until the oil temperature stabilized. The valves on the sample lines leading to the particulate filter packs were opened at this point and pumps used to draw diluted exhaust through the filters were activated. After another ten minutes, the five minute data sets for all the LabVIEW-controlled programs were started. This included the 5-Gas Analyzer, the FTIR, and the DAQ for the engine and the dilution tunnel. The high-

speed, in-cylinder pressure data were also acquired during this period. The SMPS collected data continuously, denoting each eight minute sample by its start time, so the time was noted when the filters began sampling for each data point. Once all these data sets were collected and the twenty minutes needed for accumulation of particulate matter on the filters was completed, the load produced by the dynamometer was increased to 75% load (115 Nm). Using the manual ball valve on the dilution tunnel, the dilution ratio was adjusted to remain at 40. After running at the higher load for 10-15 minutes, the same data collection procedure was repeated. Then the engine was returned to 50% load for a second data set at that load, followed by a second data set at 75% load. After completing the set of tests for each fuel, the fuel source for the fourth cylinder was switched back to ULSD and the load was brought down to 50% load for approximately ten minutes before switching to the next fuel.

In the time between data sets, the Teflon and quartz filters in their Delrin cartridges were removed from the filter packs and brought to the Control Room. Using tweezers cleaned with acetone, filters were transferred from the cartridges to numbered Petri dishes and sealed in plastic bags. The bags were labeled with all the information required to identify each test including date, load, fuel type, dilution ratio, sample time, and the number marked on the Petri dish. The Petri dishes containing quartz filters were sealed with Teflon tape before being placed in their plastic bags. At the end of each test day, all the quartz filter bags were placed in a -86 °C freezer to prevent any volatilization from the filter surface.

## 5. RESULTS AND DISCUSSION

### 5.1 Brake Power Calculation

The brake power produced by the isolated cylinder is an important quantity for data analysis, but the traditional method of using the power measured by the dynamometer cannot be used since the cylinders are not all running on the same fuel. Accordingly, the in-cylinder pressure transducer was used to calculate indicated power, which is defined as the net PdV power produced by combustion of the fuel-air mixture in the cylinder according to the following equation:

$$(5.1) \quad \dot{W}_i = \frac{d}{dt} \oint P dV$$

where  $P$  is the instantaneous in-cylinder pressure as measured by the pressure transducer and  $V$  the cylinder volume as calculated from the crank angle and cylinder geometry. The indicated power does not take into account the mechanical losses that occur in the engine between the cylinder and the dynamometer. The brake power accounts for all the losses in the engine and better represents the usable power produced by the engine.

Two Kistler 6056A in-cylinder pressure transducers were installed in the two outer cylinders so that the indicated power could be measured for the cylinder running on biodiesel and one of the cylinders that always operated on ULSD. Using these two values along with the total brake power for the whole engine, as measured by the dynamometer, it would be possible to determine the percentage of the total brake power that can be attributed to the specialty fuel cylinder 4. Unfortunately, for the tests performed in this study, it was found that when all four

cylinders were operating on ULSD, the two outer cylinders, 1 and 4, did not produce the same indicated power. Rather, cylinder 1 (the cylinder that always operated on ULSD), produced only 85-90% of the power produced by cylinder 4. The exhaust temperatures showed a similar discrepancy. Using a handheld infrared thermometer, the temperature of the exhaust manifold for each of the cylinders was checked and it was found that the two central cylinders ran slightly hotter than rest, followed closely by cylinder 4, the isolated cylinder. Cylinder 1 remained much cooler than the other three cylinders for all fuels tested.

Since cylinder 1 could not be used to convert the indicated power produced by cylinder 4 to brake power when running on biodiesel, another means was required. Using the set of baseline tests when all four cylinders were running on diesel, the brake power measured by the dynamometer was divided by four. Then that value was divided by the indicated power from cylinder 4 thereby producing the mechanical efficiency of the engine at each load. At 50% load, 64% of the indicated power was converted to brake power. At 75% load, 71% of the indicated power was converted to brake power. These mechanical efficiency values were then used to convert the indicated power of the isolated cylinder to brake power for all of the fuels. This technique relies on the assumption that the mechanical efficiency of the engine is independent of fuel type.

### **5.1.1 Brake Specific Fuel Consumption**

Using the technique described above to determine the brake power generated for each fuel, results showed that the methyl esters fuels produced less brake power than ULSD even with the engine producing the same overall power. Therefore, the brake specific fuel consumption was higher for the biodiesel blends than for ULSD. Brake specific fuel consumption is given by:

$$(5.2) \quad b s f c = \frac{\dot{m}_f}{\dot{W}_b},$$

where  $\dot{m}_f$  is the mass flow rate of fuel to the isolated cylinder and  $\dot{W}_b$  is the brake power

generated by the isolated cylinder. The results for brake specific fuel consumption are shown below in Figure 5.1, where the error bars represent the range of the data.

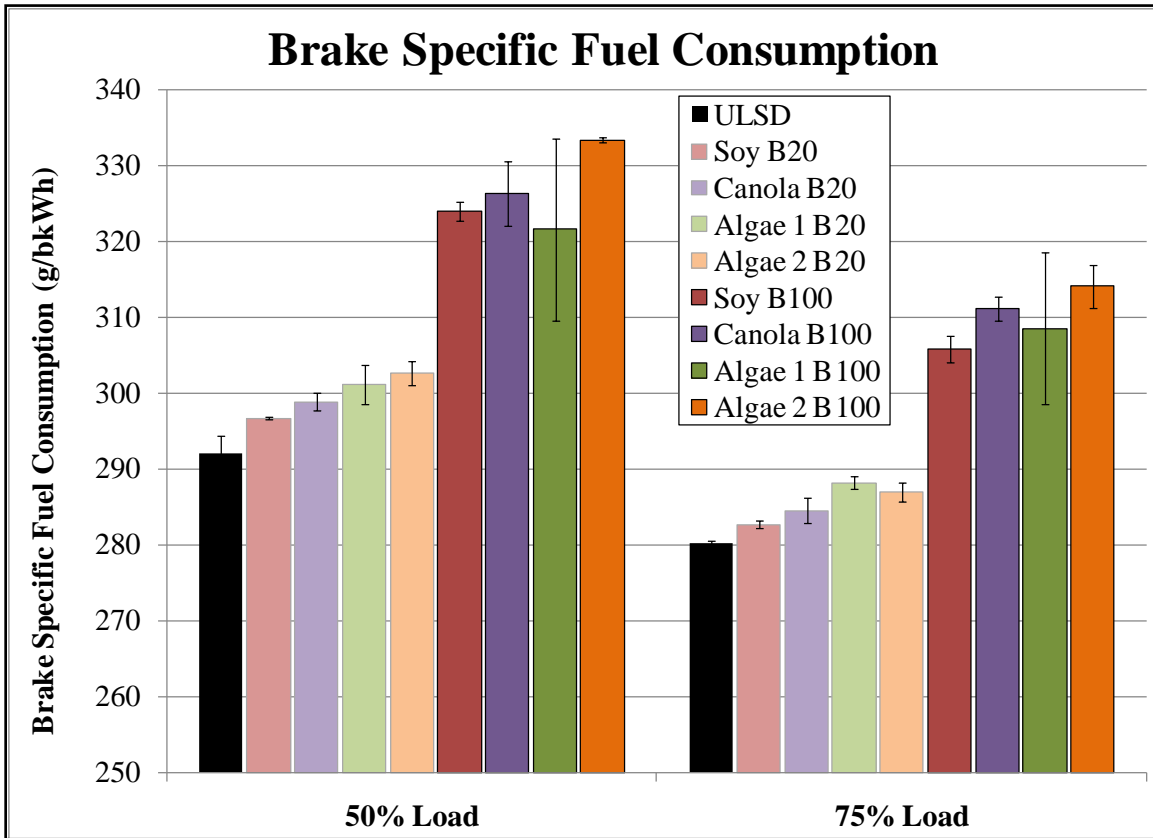


Figure 5.1 - Brake specific fuel consumption (g/kW-hr) for John Deere 4024T engine for 9 different fuel types at rated speed (2400 RPM) and 50% and 75% load. The error bars represent the range of the two runs for each data point.

The fuel consumption for the B100 blends was 10-12% higher than ULSD, with Algae 2 B100 consuming slightly more than the other methyl esters. The B20 blends consume slightly more fuel than ULSD. There is a small decrease in fuel consumption for all fuels when moving from 50% load to 75% load. Engines generally run more efficiently at higher loads, so this trend is expected (Heywood 1988). Other literature has found that brake specific fuel consumption increases by about 10% for B100 fuels, which is consistent with these results (Lapuerta, Armas and Rodriguez-Fernandez 2008).

Also it should be noted that since fuels are purchased by volume, it may be more relevant to look at how the brake specific volumetric fuel consumption varies. For example, the density of

ULSD is  $830 \text{ kg/m}^3$  and the density of canola methyl ester is  $880 \text{ kg/m}^3$ . At 50% load, Canola B100 consumes  $326 \text{ g/bkWh}$  and ULSD  $292 \text{ g/bkWh}$ . If the brake specific consumption numbers are converted to liters/bkWh using the density of the fuels, Canola B100 uses  $0.370 \text{ L/bkWh}$  and ULSD  $0.352 \text{ L/bkWh}$ . This corresponds to a 5% increase in volumetric fuel consumption when switching from ULSD to Canola B100, versus a 12% increase in mass-based fuel consumption.

The increase in fuel consumption for the biodiesel fuels is due to the lower energy content in biodiesel. The lower heating value for biodiesel fuels is about 13% lower than that of diesel. The thermal efficiency, defined below, takes into account the brake specific fuel consumption and the lower heating value for the fuel.

$$(5.3) \quad \eta_{thermal} = \frac{\dot{W}_b}{\dot{m}_f LHV} = \frac{1}{bsfc \cdot LHV}$$

where  $\dot{m}_f$  is the mass flow rate of fuel to the isolated cylinder and  $\dot{W}_b$  is the brake power generated by the isolated cylinder, and  $LHV$  is the lower heating value of the fuel. When the thermal efficiencies for all fuels at both loads are compared, there is little difference between ULSD and the biodiesel fuels, as shown in Figure 5.2. The engine running on the B100 fuels actually operates slightly more efficiently.

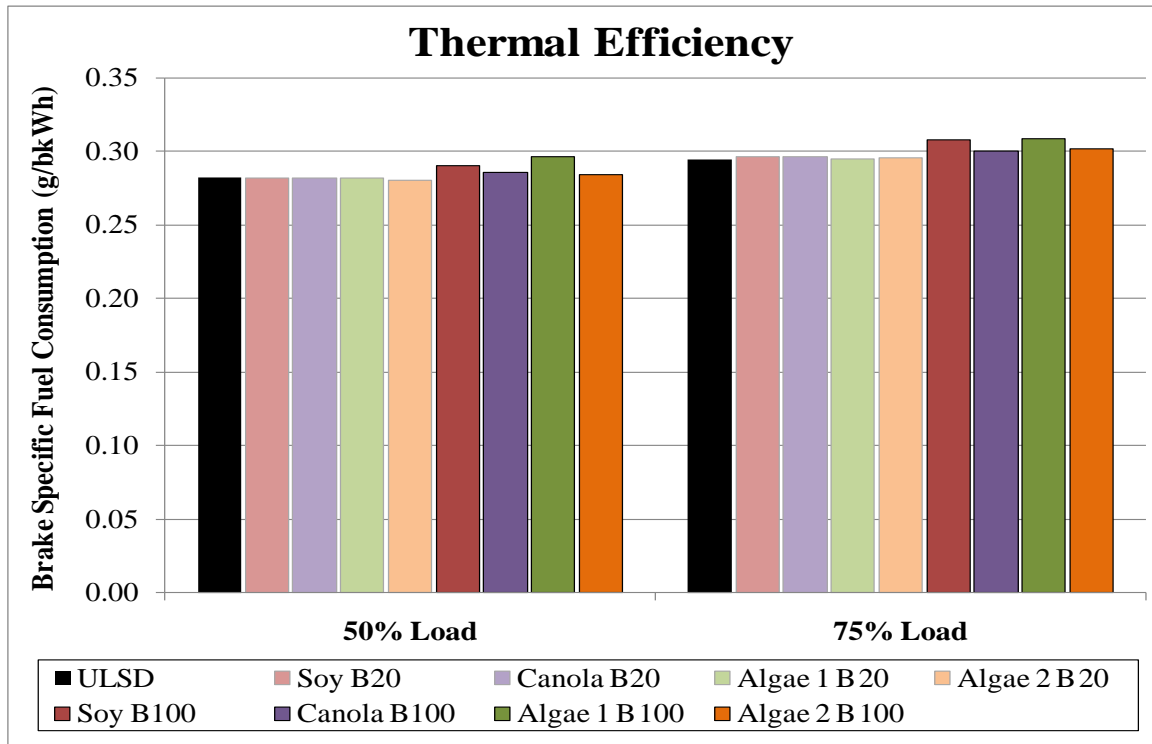


Figure 5.2 - Average thermal efficiency for all nine fuels at both loads.

## 5.2 Gaseous Emissions

For each test point, a five minute data set for the 5-gas analyzer and FTIR was collected during steady state operation. The raw data, presented as a fraction of the exhaust, was averaged over the five minute duration. Since a variety of different fuels and different engine loads were employed during this test, a more relevant way to present gaseous emissions data is in terms of brake specific emissions (g/bkWh). A carbon balance between the carbon burned in the fuel and the carbon emitted as carbon monoxide, carbon dioxide, and total hydrocarbons was used to calculate the brake specific emissions. This analysis assumes that all the carbon in the exhaust comes from the carbon in the fuel. The following equation was used to find the brake specific emissions for gaseous species  $i$ :

$$(5.4) \quad BSE_i = \frac{\dot{m}_f \cdot \alpha_f \cdot Y_i \cdot MW_i}{\dot{W}_b \cdot MW_f \cdot \sum_{exhaust} Y_j \alpha_j}$$

where  $\dot{m}_f$  is the mass flow rate of fuel to the isolate cylinder,  $\alpha_f$  the average number of carbon molecules in the fuel,  $Y_i$  the fraction of  $i^{th}$  species in the exhaust,  $MW_i$  the molecular weight of  $i^{th}$  species,  $\dot{W}_b$  the brake power generated by the single cylinder,  $MW_f$  the molecular weight of the fuel, and  $\sum_{exhaust} Y_j \alpha_j$  the sum of the number of carbon molecules found in the exhaust constituents. This calculation accounts for differences in fuel composition and power produced. This formula was used for both the 5-Gas data and the FTIR data.

### 5.2.1 5-Gas Analyzer Results

Figures 5.3 through 5.5 show the brake specific emissions for carbon monoxide (CO), total hydrocarbons (THC), and nitrogen oxides (NO<sub>x</sub>) for all 9 fuels at 50% and 75% load, respectively. The error bars represent the range of the two runs for each data point. Most studies have shown that when running a diesel engine on B100 biodiesel rather than petroleum diesel, CO and THC decrease but NO<sub>x</sub> increases (EPA 2002). This result is also typically found for biodiesel blends with petroleum diesel, although it has been found that the results are highly dependent on the engine type, engine duty cycle and biodiesel feedstock (McCormick, et al. 2006). Emissions of NO<sub>x</sub> tend to increase with increasing levels of unsaturation in the methyl ester hydrocarbon chain (McCormick, Graboski, et al. 2001) (Allan, et al. 2008). Due to the long and highly unsaturated fatty acid methyl ester content in the two algal methyl ester formulations, it was anticipated that that these fuels might produce even more NO<sub>x</sub> than is generally seen with biodiesel.

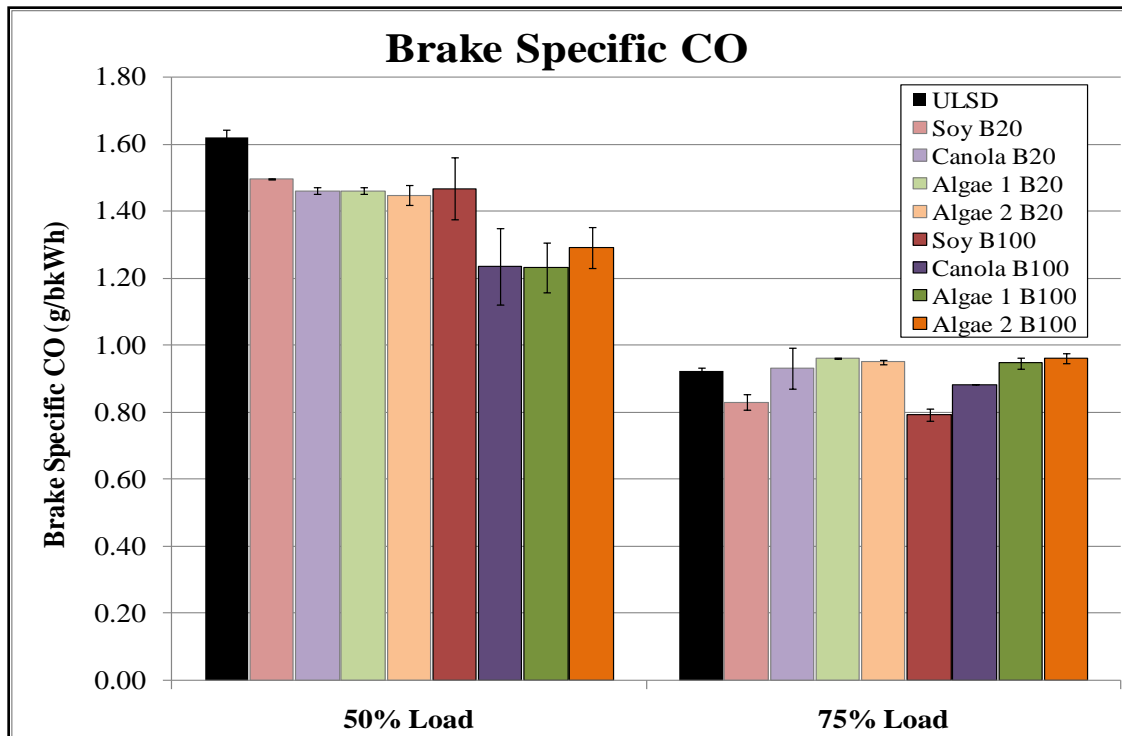


**Figure 5.3 - Brake specific carbon monoxide emissions (g/kW-hr) for John Deere 4024T engine for 9 different fuel types at rated speed (2400 RPM) and 50% and 75% load. The error bars represent the range of the two runs for each data point.**

As shown in Fig. 5.3, the CO produced by the all of the biodiesel blends was less than that produced by ULSD at the lower load, with the B100 fuels producing less CO than the B20 fuels. These results are consistent with previous studies (EPA 2002). At the higher load, however, only the soy biodiesel blends reduced the carbon monoxide emitted relative to ULSD. However, it should be noted that the level of CO emissions at both loads is well below the current emissions regulations for this size and type of engine. Specifically, for an off-road Tier 2 engine producing a maximum of 39 kW, the 2007 standards limit CO to 5.0 g/kWh (Standards on Performance for Stationary Compression Ignition Internal Combustion Engines 2006). All of fuels at both loads meet this standard.

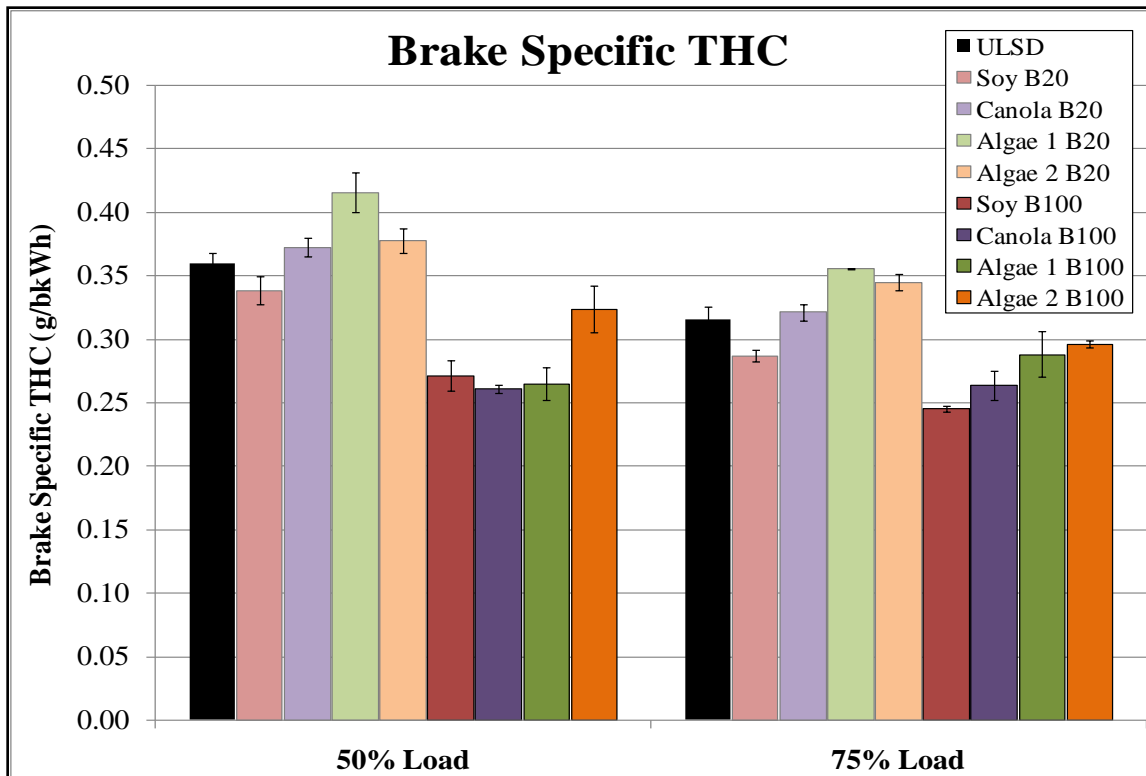


Figure 5.4 - Brake specific total hydrocarbon emissions (g/kW-hr) for John Deere 4024T engine for 9 different fuel types at rated speed (2400 RPM) and 50% and 75% load. The error bars represent the range of the two runs for each data point.

As shown in Fig. 5.4, all of the B100 biodiesel blends resulted in a reduction in THC in comparison to ULSD at both loads. The B20 blends emitted higher levels of THC, with Algae 1 B20 producing the highest level for both loads. It should be noted that, for this class of engine, total hydrocarbons alone are not regulated. Rather, current EPA standards call for the regulation of the sum of  $\text{NO}_x$  and non-methane hydrocarbons (NMHC). For fuels like diesel and biodiesel, very little of the hydrocarbons emitted will be methane. The FTIR is set up to measure methane but the levels of methane detected were small in comparison to the total hydrocarbon measurement and the uncertainty in the methane measurement was larger than the measured concentration, making it statistically irrelevant. Therefore, total hydrocarbons measured by the 5-Gas analyzer can be considered equivalent to non-methane hydrocarbons. The current  $\text{NO}_x$ +NMHC regulation for this size of engine is 4.7 g/kWh, with the majority of that total coming from  $\text{NO}_x$  (to be discussed in the next section).

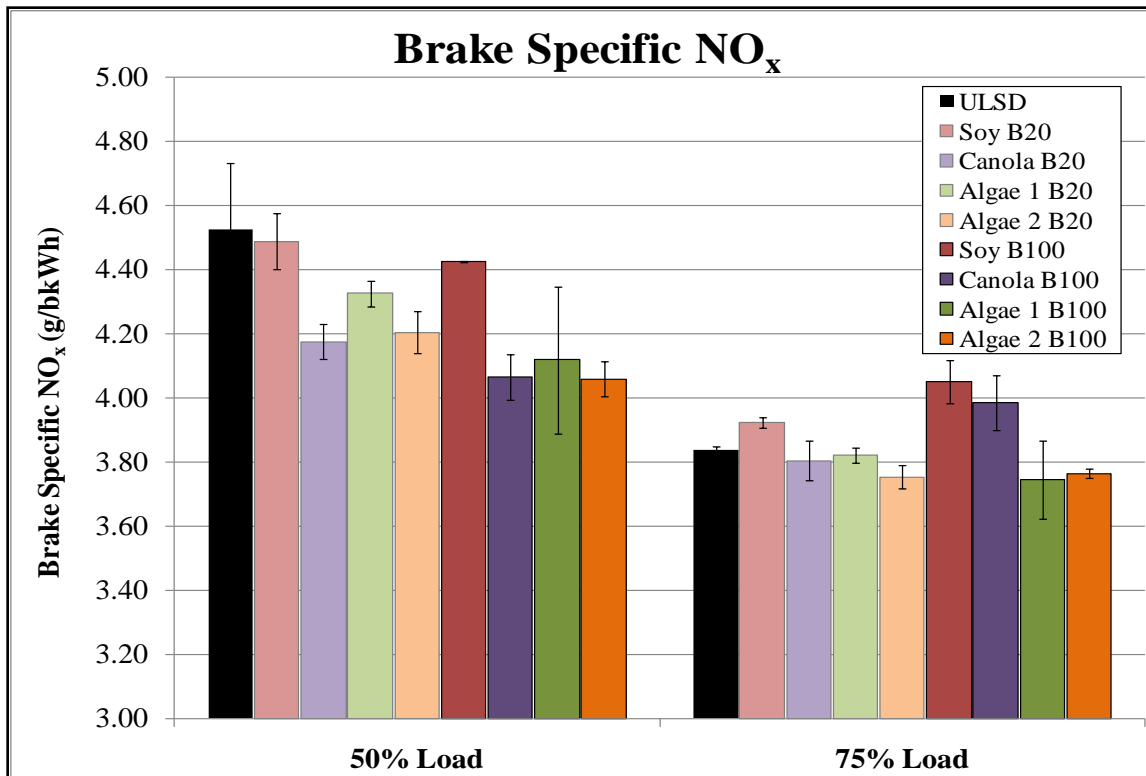


Figure 5.5 - Brake specific NO<sub>x</sub> emissions (g/kW-hr) for John Deere 4024T engine for 9 different fuel types at rated speed (2400 RPM) and 50% and 75% load. The error bars represent the range of the two runs for each data point.

Figure 5.5 shows that, contrary to expectations based on earlier research, the NO<sub>x</sub> produced by the two algal biodiesels did not increase relative to the other biodiesel, or even relative to ULSD. The only B100 fuels to reduce NO<sub>x</sub> at both loads were Algae 1 and Algae 2. At the lower load, all the biodiesel blends reduced NO<sub>x</sub> but at the higher load, Soy and Canola B100 produced more NO<sub>x</sub> than ULSD. Studies have shown that soy biodiesel tends to generate more NO<sub>x</sub> than canola biodiesel, which is consistent with these results (Graboski, McCormick and Alleman, et al. 2003).

The regulations for NO<sub>x</sub> in the U.S. are given as a combination of NO<sub>x</sub> and non-methane hydrocarbons. The current standard is that the sum of NO<sub>x</sub> and NMHC should be less than 7.5 g/kWh for engines made in or before 2007. The newer standard, for engines made between 2008 and 2012, states that NO<sub>x</sub> and NMHC combined should be less than 4.7 g/kWh. All of the fuels comply with the 2007 standard at both loads and almost all fuels and loads comply with the

stricter 2012 regulations. Only ULSD and Soy B20 at the lower load are higher than this specification. It should be noted that the tests reported here were not conducted in strict accordance with the 40 CFR standard test procedures. However, the brake specific emissions levels provide confidence that the engine was operating properly.

The 5-Gas Analyzer measured NO and NO<sub>2</sub> separately and while most literature lumps the two together in a NO<sub>x</sub> measurement, they can be looked at individually. For completeness, separate plots of brake specific NO and NO<sub>2</sub> are shown below in Figures 5.6 and 5.7.

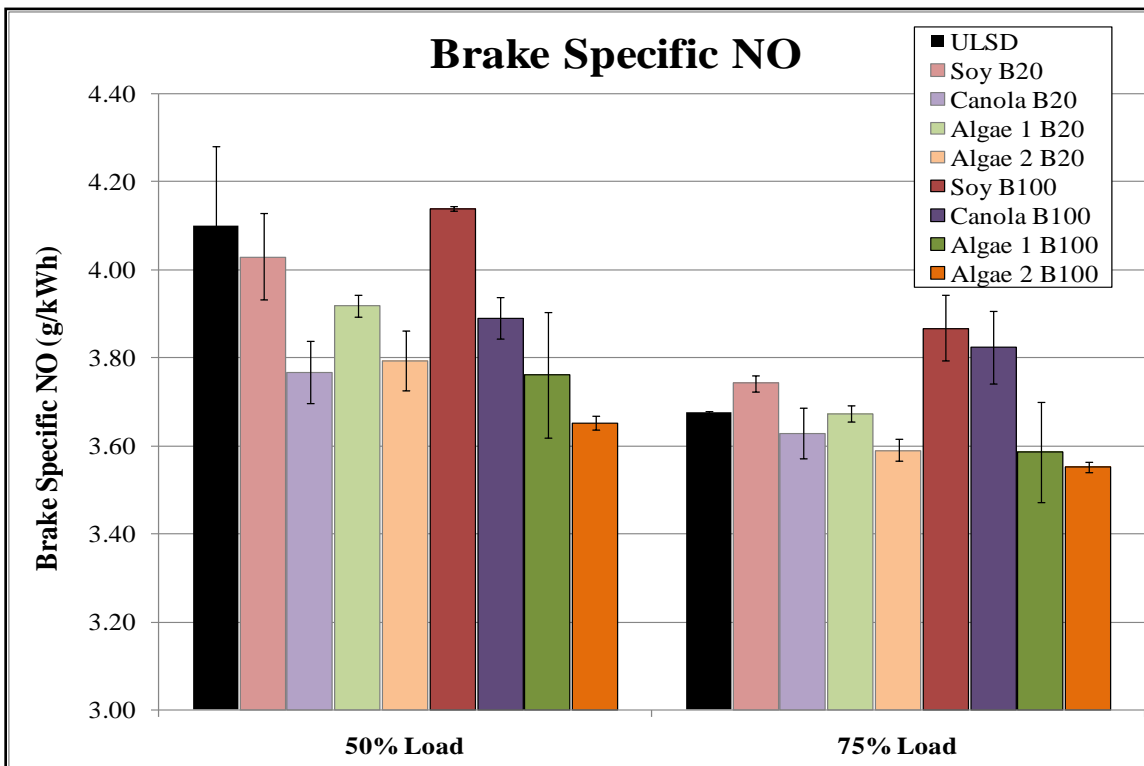


Figure 5.6 - Brake specific NO emissions (g/kW-hr) for John Deere 4024T engine for 9 different fuel types at rated speed (2400 RPM) and 50% and 75% load. The error bars represent the range of the two runs for each data point.

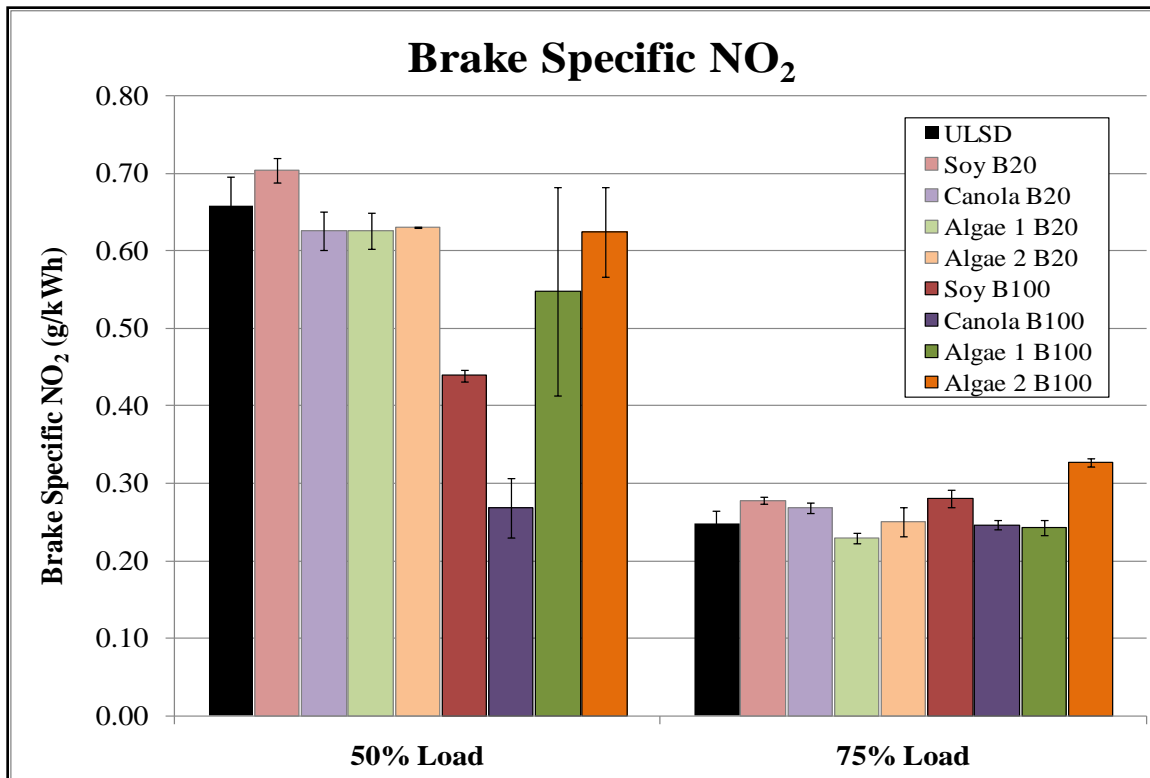


Figure 5.7 - Brake specific NO<sub>2</sub> emissions (g/kW-hr) for John Deere 4024T engine for 9 different fuel types at rated speed (2400 RPM) and 50% and 75% load. The error bars represent the range of the two runs for each data point.

Since NO makes up over 90% of the total NO<sub>x</sub> emissions, it follows that the relative NO emissions have the same pattern as the NO<sub>x</sub> emissions. Soy and canola B100 methyl esters produce the highest NO levels of the B100 blends at both loads, while soy and algae 1 B20 create the most NO for the B20 blends. For both loads and blends, the algal methyl esters produce less NO than ULSD.

However, the NO<sub>2</sub> results do not resemble the overall NO<sub>x</sub> emissions. Unlike the NO and NO<sub>x</sub> results, algae 1 and algae 2 B100 produce high levels of NO<sub>2</sub>, especially at 50% load. The B20 blends emit relatively the same amount of NO<sub>2</sub>, with soy B20 producing slightly higher levels than the other fuels.

### 5.2.2 Heat Release

The in-cylinder pressure transducer records high speed pressure data, which can be plotted as a function of crank angle. The known geometry of the cylinder and connecting rod can then be used to calculate the cylinder volume as a function of crank angle. Pressure versus volume curves can then be used to calculate the apparent rate of heat release ( $J/deg$ ) due to fuel combustion in the cylinder. The apparent heat release rate calculation assumes a rate of heat loss to the cylinder walls and some additional losses due to crevice effects. The remaining energy generated during combustion is referred to as the net apparent heat release, the energy that actually goes towards doing work. A LabVIEW program was used to convert pressure vs. crank angle to apparent heat release rate given the engine geometry.

Since the heat release rate is based on time derivatives of the instantaneous pressure data ( $dP/dt$ ), the resulting heat release calculations contain a substantial high frequency component, which is inherent to taking the time derivative of experimental data. Accordingly, a low pass Inverse Chebyshev filter was used with the LabVIEW pressure data program to filter out the high frequency component (Winder 2002). The filter parameters were adjusted so that most of the oscillations due to the time derivative of pressure were removed but not to the point that some key characteristics of the heat release curve were lost. In diesel combustion, the general shape for a heat release rate curve begins with a peak due to premixed autoignition event, followed by a longer duration combustion curve dictated by the mixing rate of the fuel and air. An example heat release rate curve which exhibits both the premixed and mixing-controlled phases of diesel combustion is shown below in Figure 5.8.

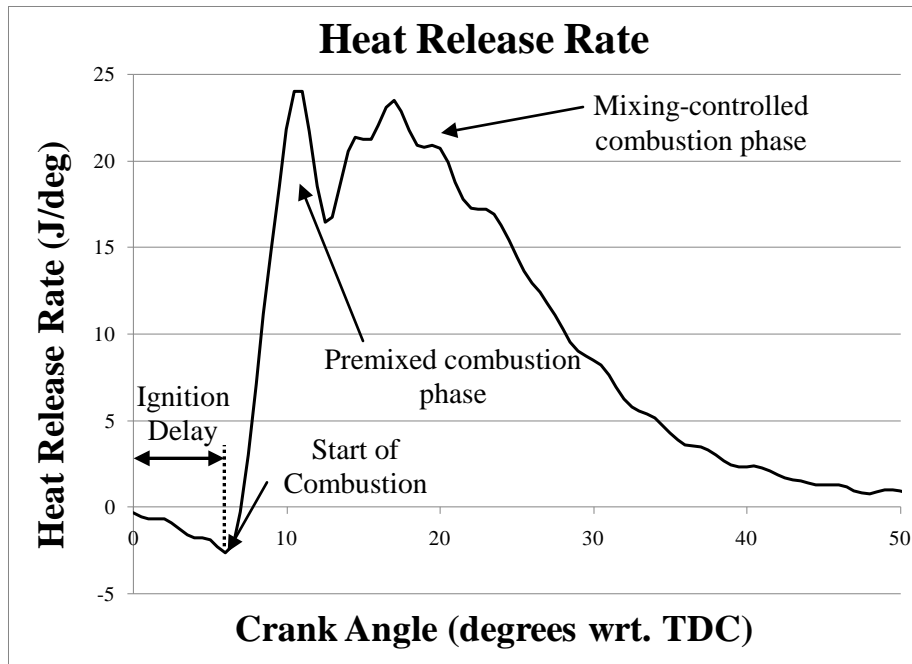


Figure 5.8. Example heat release rate curve.

As shown in Figure 5.8, the mixing-controlled phase still contains some higher frequency oscillation because the degree of filtering required to remove all of the high frequency oscillations results in the complete loss of the premixed autoignition combustion peak. Examples are shown in Appendix C as to how the parameters of the Chebyshev filter affect the calculation of apparent heat release rate. As underscored in the data in Appendix C, significant care must be taken when performing heat release rate calculations so that artificial high frequency oscillations are filtered out, but real events such as the premixed burn event are retained. For the calculations presented herein, once suitable Chebyshev filter parameters were chosen, the filter parameters were kept constant for all the fuels and loads analyzed. The apparent heat release rate curves (J/deg) are presented in Figs. 5.9 to 5.12 for the B100 and B20 blends at 50% and 75% load, respectively.

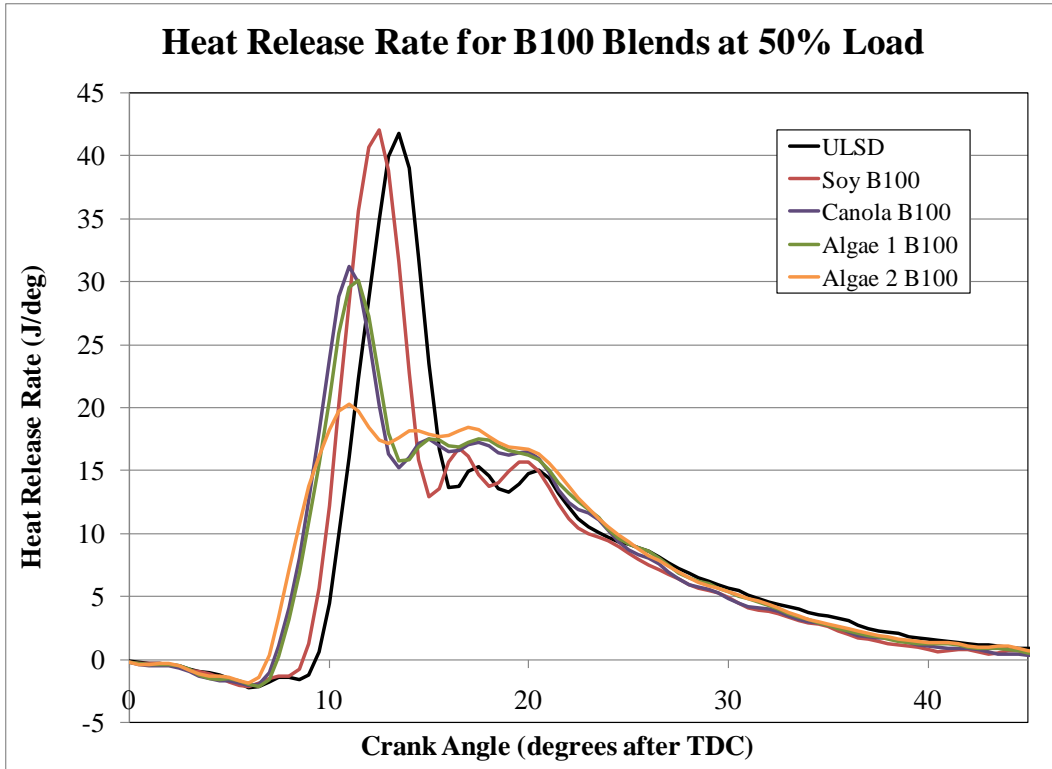


Figure 5.9 - Heat Release Rate (J/deg) from John Deere 4024T engine for B100 Blends at 50% load.

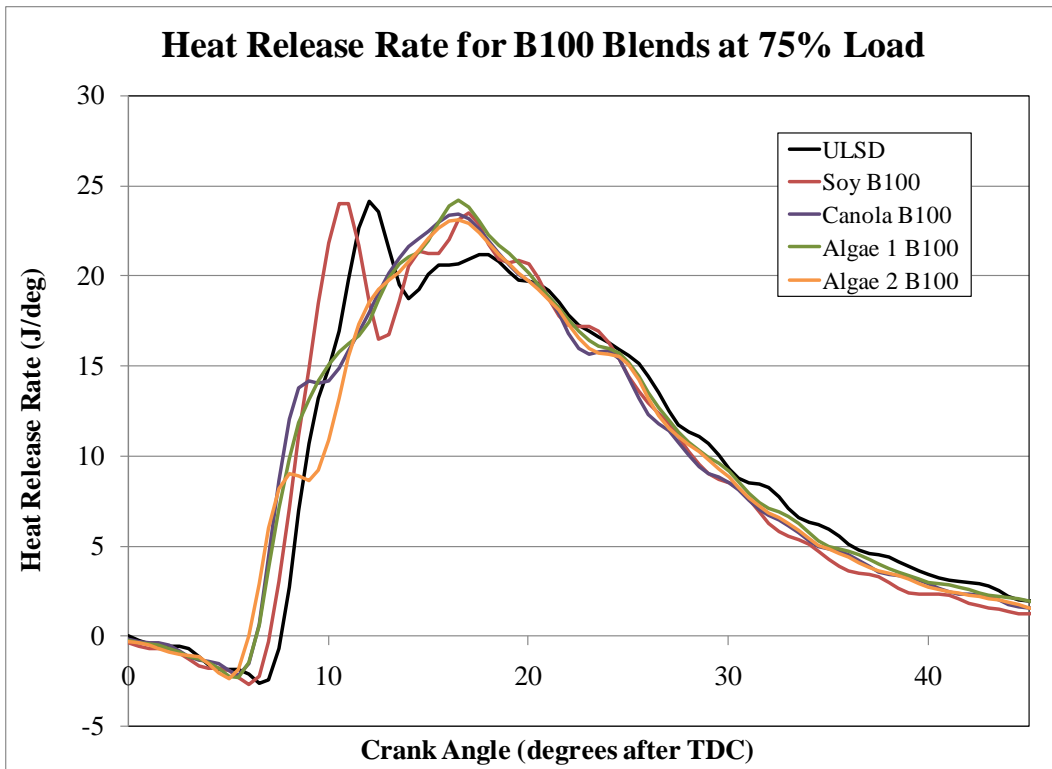


Figure 5.10 - Heat Release Rate (J/deg) from John Deere 4024T engine for B100 Blends at 75% load.

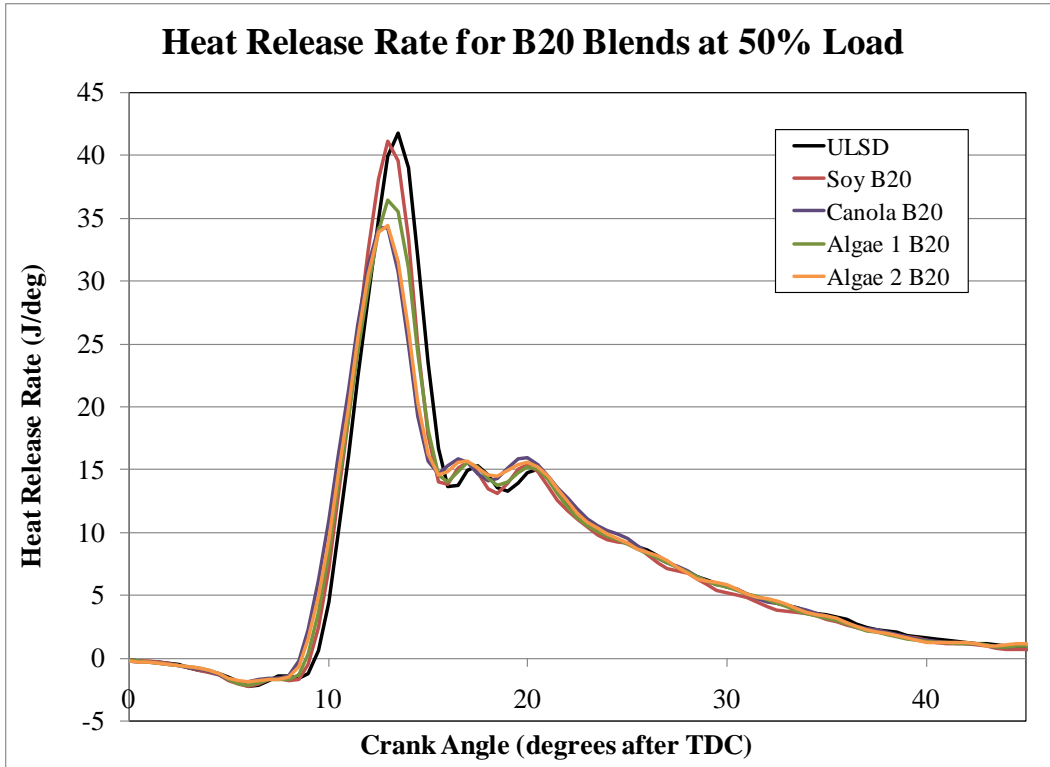


Figure 5.11 - Heat Release Rate (J/deg) from John Deere 4024T engine for B20 Blends at 50% load.

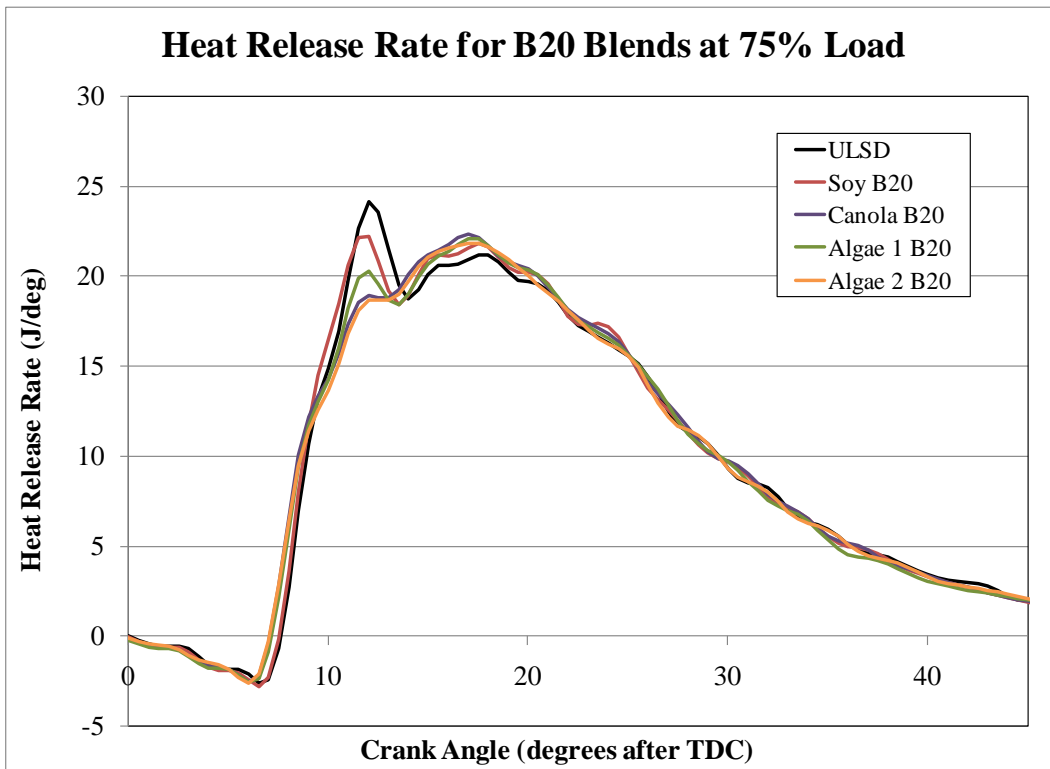


Figure 5.12 - Heat Release Rate (J/deg) from John Deere 4024T engine for B20 Blends at 75% load.

In these four heat release rate plots, there are several phenomena to note. First, all of the biodiesel blends resulted in an advance in the start of combustion in comparison to the ULSD. This is not unexpected as many studies have shown that biodiesel tends to advance the start of injection (and thereby the start of combustion) because of the higher bulk modulus (a measure of the speed of sound in a liquid) of biodiesel with respect to petroleum diesel (Mueller, Boehman and Martin 2009). In the current configuration, the fuel injectors of the 4024T engine are not instrumented, so there is no way to distinguish between an increase in start of combustion due to advance in injection timing or a decrease in the ignition delay. Accordingly, the advance in start of combustion could be a combination of those two effects. The advance in combustion is more pronounced with B100 blends, with Canola B100, Algae 1 B100 and Algae 2 B100 starting combustion even a few degrees before Soy B100.

The second characteristic of note in Figs. 5.9 through 5.12 is the height of (and integrated area underneath) the initial premixed combustion peak. For example, as shown in Figs. 5.9 and 5.10, the height of the premixed combustion peak for Soy B100 is approximately the same as ULSD, but advanced by a few degrees. However, for all of the other B100 methyl esters, the height of the premixed combustion peaks are much lower than that of ULSD. Similarly, as shown in Figs. 5.11 and 5.12, the height of the premixed combustion peak is lower than that of ULSD for all of the B20 methyl ester blends.

### **5.2.3 Premixed Burn Fraction and NO<sub>x</sub> Production**

Referring back to Figure 5.8, during the ignition delay period, a portion of the liquid fuel spray evaporates, mixes with the air and locally reaches the rich flammability limit for that fuel. This vaporized fuel and air mixture then autoignites, resulting in a rapid pressure rise as signified by the first peak in the heat release curve. After the autoignition event, the remaining fuel can only burn as fast as it can vaporize and diffuse to a non-premixed flame zone where it reacts stoichiometrically with oxygen. The second, longer duration peak denotes this mixing-controlled

combustion phase. The production of  $\text{NO}_x$  in diesel engines is typically attributed to the mixing-controlled combustion phase because the mixture is burned stoichiometrically and therefore at a higher temperature. Moreover, the longer duration of the mixing controlled phase (as compared to the premixed combustion phase) promotes  $\text{NO}_x$  formation. However, recent studies suggest that the premixed combustion phase is responsible for increased  $\text{NO}_x$  production observed with methyl esters.

The most common mechanism for  $\text{NO}_x$  production is known as the thermal or Zeldovich mechanism, which is highly dependent on temperature and very slow in comparison to other chemical reactions occurring during combustion (Turns 2000). Accordingly, during the mixing controlled phase, the Zeldovich mechanism is assumed to dominate  $\text{NO}_x$  production. However, during the premixed combustion phase, the fuel rich combustion occurs too fast and at too low a temperature to promote substantial NO production via the Zeldovich mechanism. For that reason, if substantial NO is produced during the premixed combustion phase, it is likely due to the prompt or Fenimore  $\text{NO}_x$  mechanism. Prior to discussing the differences in the premixed autoignition zone between ULSD and methyl ester combustion, a quick review of the many theories used to explain biodiesel  $\text{NO}_x$  increases is presented.

The full mechanism responsible for increased  $\text{NO}_x$  emissions from combustion of fatty acid methyl esters (FAME) has yet to be fully explained and debate is ongoing as to whether it is a consequence of differences in physical properties or chemical kinetics. Numerous mechanisms have been hypothesized (Cheng, Upatnieks and Mueller 2006). The physical properties of biodiesel that may explain the increase in  $\text{NO}_x$  are boiling point, bulk modulus, and viscosity. According to Choi and coworkers, the higher boiling point of biodiesel relative to petroleum diesel will cause the fuel to be injected further into the cylinder, increasing the fuel consumed in the premixed phase of combustion, resulting in higher  $\text{NO}_x$  emissions. (Choi, Bower and Reitz 1997). Biodiesel has a higher bulk modulus and causes the fuel to be injected earlier in the combustion cycle, which increases the reaction time and temperature, increasing  $\text{NO}_x$  production

(Heywood 1988) (Szybist and Boehman 2003) (J. Szybist, A. Boehman, et al. 2005) . The last physical property that could affect  $\text{NO}_x$  production is viscosity. Biodiesel has a higher viscosity than diesel and so the fuel spray will have poorer atomization and reduced spray penetration, which reduces combustion efficiency (Patterson, et al. 2006).

Differences in chemical properties also may be responsible for the increase in  $\text{NO}_x$ . Biodiesel is an oxygenated fuel and this difference in chemical structure may be responsible for increased production during combustion of the CCO radical, which has been proposed as a prompt  $\text{NO}_x$  precursor (Williams and Fleming 2007) (Konnov 2009). Cetane number affects ignition timing, with the higher cetane number of biodiesel leading to an advance in injection timing. This increases the residence time for the combustion products at high temperatures and increases thermal  $\text{NO}_x$  production (Ban-Weiss, Buchholz and Dibble 2007). Additionally, the differences between diesel and biodiesel in radiative heat transfer during combustion have also been proposed as the sources of the  $\text{NO}_x$  increase. Biodiesel produces less soot than diesel and since soot radiation is the primary means of heat loss from an in-cylinder flame, the radiative heat loss should be lower for biodiesel thereby producing higher flame temperatures and increased thermal  $\text{NO}_x$  (Cheng, Upatnieks and Mueller 2006).

The last mechanism of  $\text{NO}_x$  increase, which will be explored further in the present study, relates to the premixed-burn fraction. Specifically, it has been shown that, for biodiesel, a larger fraction of the heat release occurs during the premixed-burn phase of combustion at ignition. It has been hypothesized that the difference in  $\text{NO}_x$  produced during premixed combustion is responsible for the biodiesel  $\text{NO}_x$  increase. During the premixed combustion phase, prompt  $\text{NO}_x$  is the mechanism for  $\text{NO}_x$  production. Others have hypothesized that prompt  $\text{NO}_x$  is also responsible for the difference in  $\text{NO}_x$  emissions between different biodiesels (McCormick, Alvarez and Graboski 2003). A study performed by NREL found that different types of biodiesel produced similar levels of particulate matter but different amounts of  $\text{NO}_x$ . Usually, there is a trade-off between  $\text{NO}_x$  and PM but if PM remains constant than that relationship is no longer

applicable. The PM/NO<sub>x</sub> trade-off is attributed to the thermal NO<sub>x</sub> mechanism since an elevated amount of PM in the combustion products will reduce the temperature, which reduces the amount of NO<sub>x</sub> produced via the thermal mechanism (McCormick, Graboski, et al. 2001).

Although many competing mechanisms may be involved, it is clear that biodiesel NO<sub>x</sub> production is affected by the premixed combustion phase. One way to quantify the amount of fuel burned in the premixed phase is to examine the ratio of the heat release generated in the premixed phase relative to all the heat released in the cycle. This ratio is called the premixed burn fraction. Figure 5.13 shows the calculated premixed burn fraction for each fuel/ load condition.

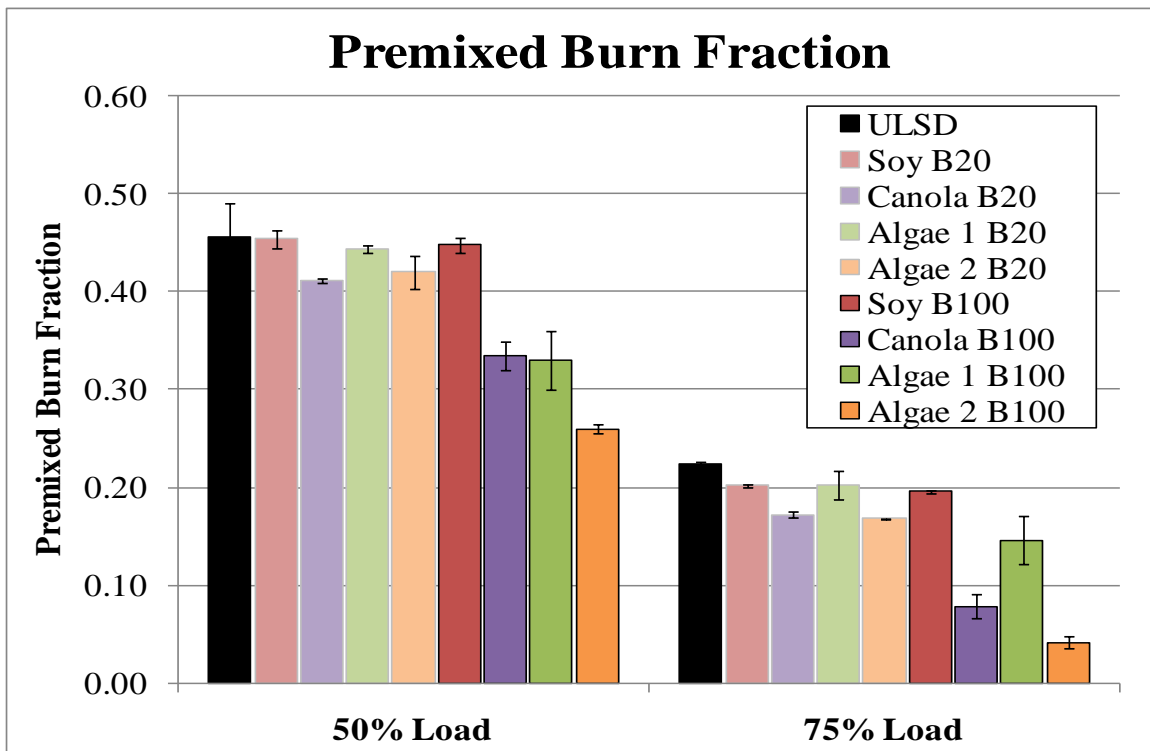
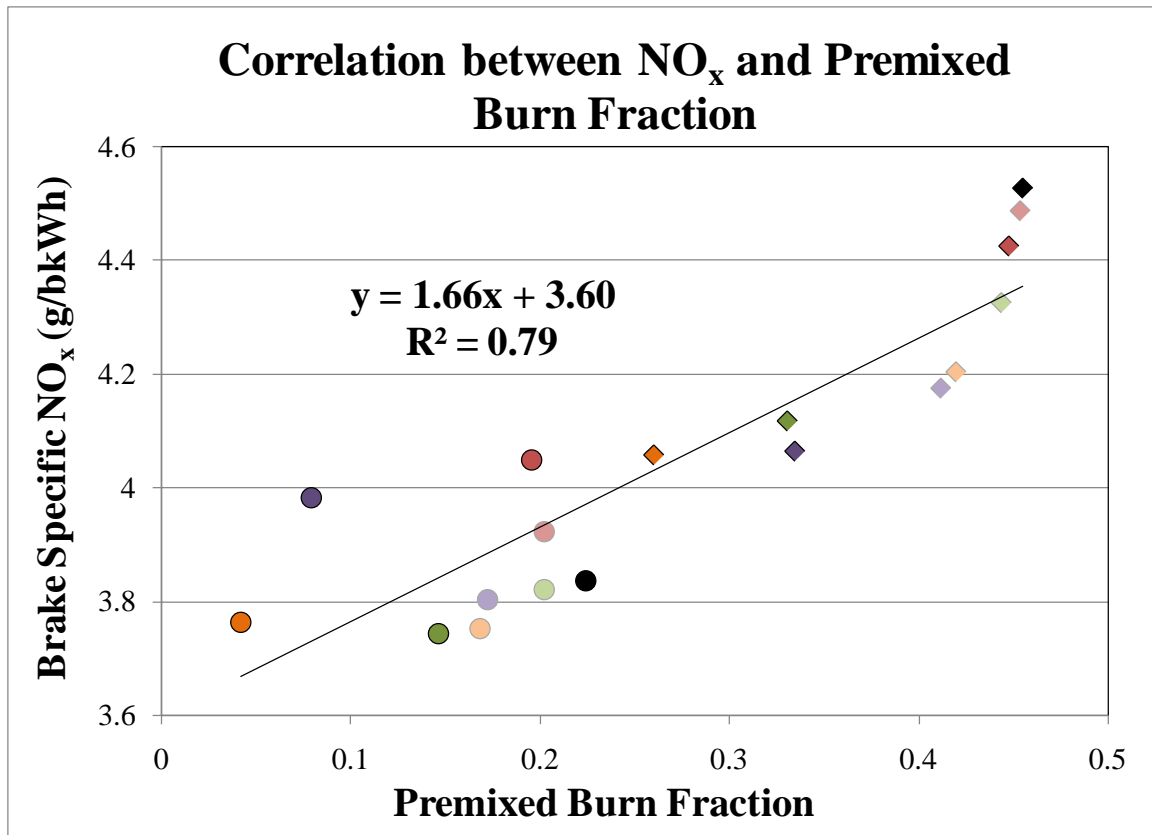


Figure 5.13 - Premixed burn fraction for all fuels. The error bars represent the range of the two runs for each data point.

Premixed burn fraction is intended to be a parameter used to explain why biodiesel NO<sub>x</sub> emissions increase with respect to petroleum diesel. That the premixed burn fraction for ULSD is larger than most of the other fuels is not entirely unexpected since there were only a few fuels that

increased  $\text{NO}_x$  relative to ULSD. The three cases where the average  $\text{NO}_x$  value was larger than ULSD are Soy B20 and B100 at 75% load and Canola B100 at 75% load and in all of these cases, the premixed burn fraction for the biodiesel blends are smaller than ULSD at that load. Along with Algae 2 B100 at 75% load, the premixed burn fraction for Canola B100 at 75% load appears uncharacteristically low. The premixed burn fraction was determined by dividing the integrated area below the initial peak in the heat release rate curve by the area under the entire curve. The filtering process used to filter out the high frequency component of the heat release rate curves altered the height of the premixed peak and so this process also affects the calculated premixed burn fraction. It is possible that the filtering of the heat release curves is responsible for the low premixed burn fraction values for Canola B100 and Algae 2 B100 at 75% load.

Aside from the two data points that appear abnormally low, the premixed burn fraction correlates well with the  $\text{NO}_x$  results. Since the ULSD premixed fraction is larger than the fuels that produced more  $\text{NO}_x$ , it is likely that there are other factors that contribute to the increased  $\text{NO}_x$  in biodiesel. However, the data shows a relationship between  $\text{NO}_x$  production and premixed burn fraction. Figure 5.14, which is a plot of brake specific  $\text{NO}_x$  emissions versus premixed burn fraction, demonstrates the correlation. The data points are colored to indicate the fuel type and the load is identified by the data point shape: diamond-shaped points represent 50% load and circles denote 75% load. The data clearly shows that, for the experiments presented here, the  $\text{NO}_x$  emissions varied linearly with premixed burn fraction.



**Figure 5.14 - Brake Specific NO<sub>x</sub> vs. Premixed Burn Fraction.** The data points are colored to show fuel type. Diamond-shaped data points correspond to 50% load; Round data points denote 75% load.

Since the John Deere 4024T engine was not equipped with injection monitors, it is impossible to know when injection occurred for each of these fuels. As discussed above, some biodiesel properties cause injection to be advanced relative to ULSD. Combustion is also advanced with methyl esters, as seen in the heat release plots shown in Figures 5.9 through 5.12, which could be due to an advance in injection or a shorter ignition delay, as would be caused by a higher cetane number (Ban-Weiss, Buchholz and Dibble 2007). Upon a closer inspection of the heat release plots, the fuels that had the earliest combustion also had the smallest premixed burn fraction. That same relationship between start of combustion and premixed burn fraction was seen in Heywood when varying air temperature within the cylinder (Heywood 1988). Intuitively this relationship makes sense if the ignition delay is responsible for the advance in combustion, since a shorter time between fuel injection and combustion would mean less fuel could vaporize

and reach the upper flammability limit, decreasing the amount fuel burned in the premixed combustion phase. Figure 5.15, below, shows a plot of premixed burn fraction vs. start of combustion (SOC), which shows the correlation.

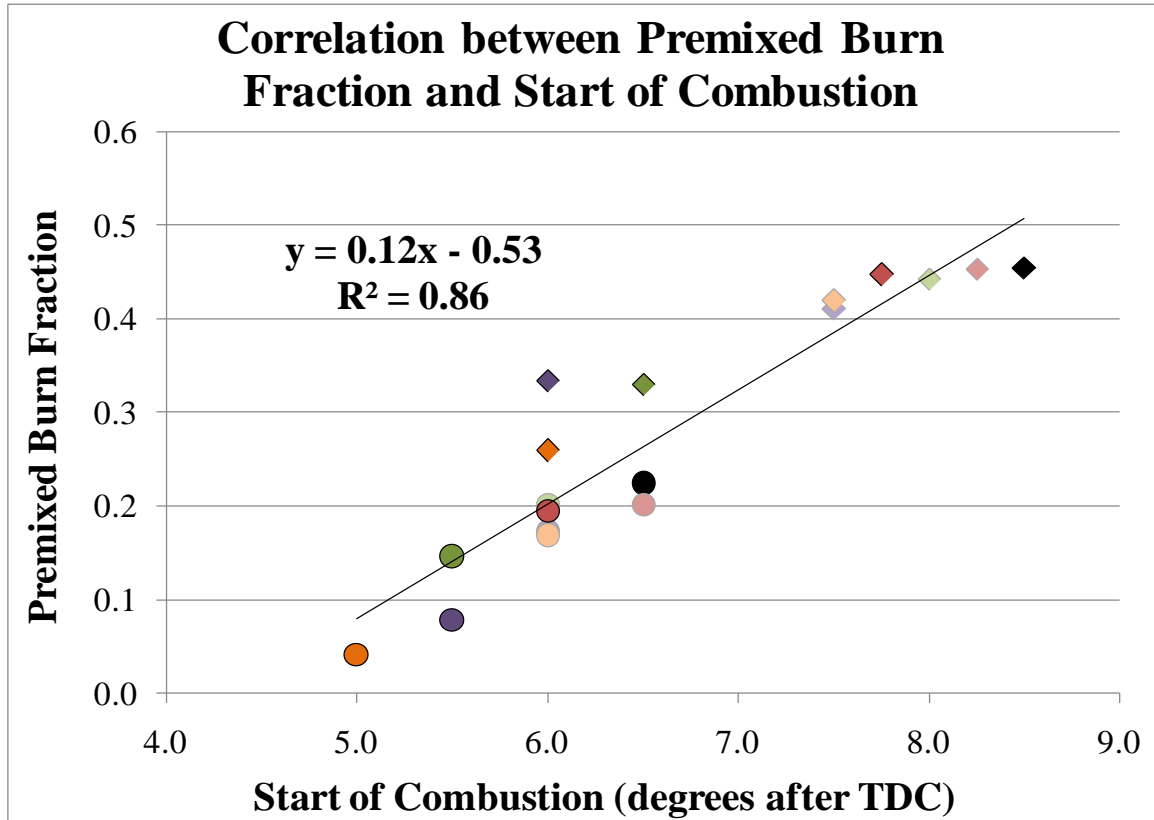


Figure 5.15 - Premixed Burn Fraction vs. Start of Combustion. Diamond-shaped data points correspond to 50% load; Round data points denote 75% load.

Since there is a strong correlation between brake specific  $\text{NO}_x$  and premixed burn fraction and between premixed burn fraction and start of combustion, it should follow that there also will be a correlation between brake specific  $\text{NO}_x$  and start of combustion. Figure 5.16 is a plot of brake specific  $\text{NO}_x$  versus start of combustion.

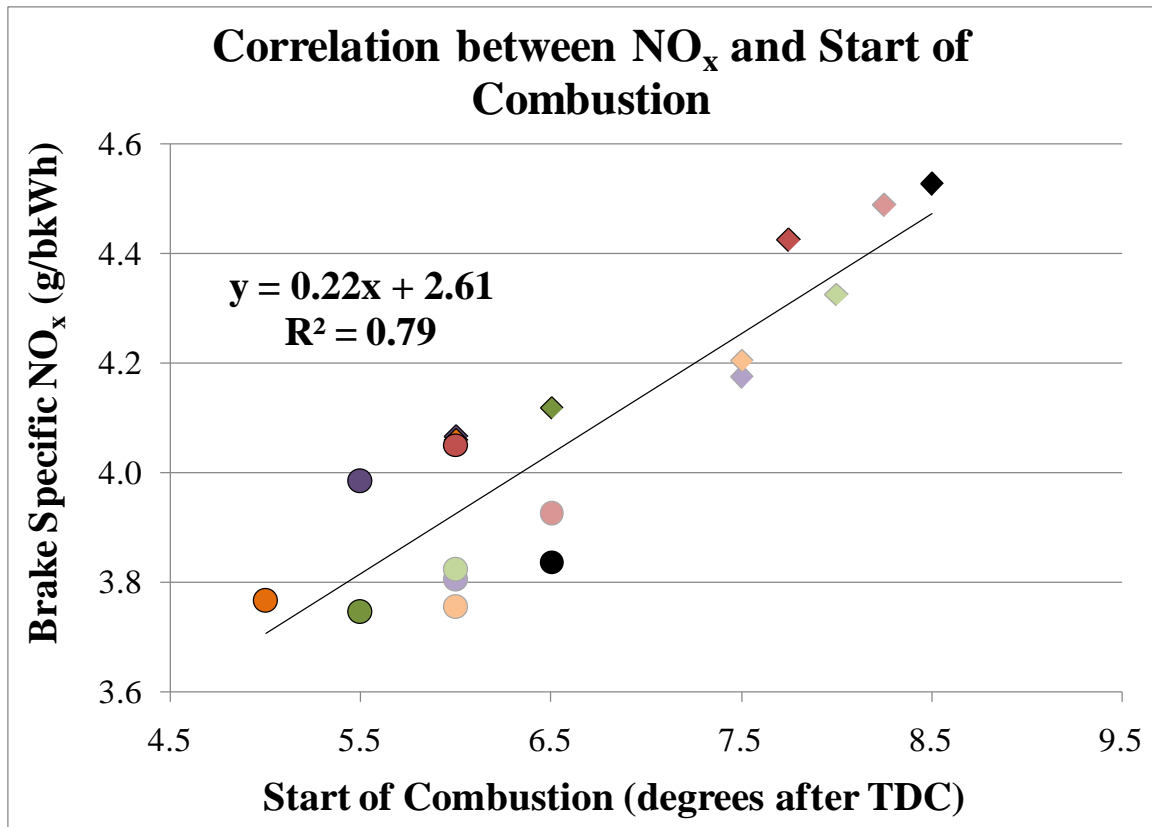


Figure 5.16 - Brakes Specific NO<sub>x</sub> vs. Start of Combustion. Diamond-shaped data points correspond to 50% load; Round data points denote 75% load.

Most of the theories used to explain the biodiesel NO<sub>x</sub> increase say that an advance in start of combustion would lead to an increase in NO<sub>x</sub> due to an increased residence time and therefore higher temperatures. Figure 5.16 shows the opposite trend. As the start of combustion is advanced further, NO<sub>x</sub> decreases. Based on Figures 5.14 and 5.15, the relationship between start of combustion and NO<sub>x</sub> has more to do with premixed burn fraction. A later start of combustion seems to imply a longer ignition delay, leading to an increase in premixed burn fraction. This would also imply that most of the NO<sub>x</sub> is produced via prompt NO<sub>x</sub> and not thermal NO<sub>x</sub>. A comprehensive study on the biodiesel NO<sub>x</sub> increase by Mueller and Boehman found that a hydrocarbon fuel with identical ignition delay and start of combustion to Soy B100 biodiesel produced less NO<sub>x</sub> than the biodiesel (Mueller, Boehman and Martin 2009). They also found that an increase in premixed burn fraction always accompanied an increase in NO<sub>x</sub>. It

should be noted that other studies have used retarded injection timing as a means to decrease  $\text{NO}_x$  emissions (Zhang and Boehman 2007). If the injection event is retarded enough that the bulk cylinder temperatures start to decrease,  $\text{NO}_x$  will also decrease.

#### **5.2.4 FTIR Results**

The EECL has developed test methods using the Nicolet Magna 560 FTIR to measure a variety of gaseous species that are typically found in internal combustion engine exhaust, including oxides of nitrogen, oxides of sulfur and various hydrocarbon species that are considered hazardous air pollutants, such as aldehydes. Some of these species are also measured by the 5-Gas analyzer (e.g.  $\text{NO}$ ,  $\text{NO}_2$ ,  $\text{CO}$ ) and many of the other species for which test methods have been developed are not produced in significant concentrations in diesel and biodiesel combustion. Two exhaust species of interest that were measured in significant quantities in the FTIR data were formaldehyde and acetaldehyde. The brake specific emissions for these two aldehydes are shown below in Figures 5.17 and 5.18, with the error bars representing the range of the two sets of data taken.

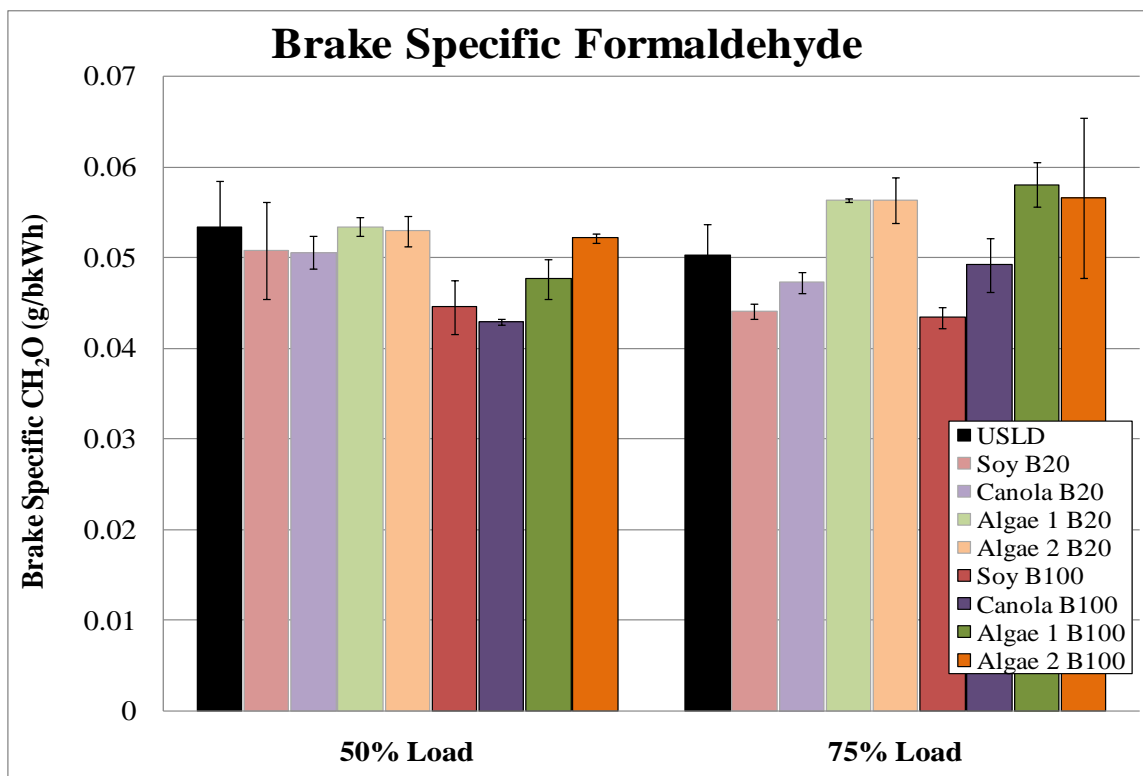


Figure 5.17 - Brake specific formaldehyde emissions (g/kW-hr) for John Deere 4024T engine for 9 different fuel types at rated speed (2400 RPM) and 50% and 75% load. The error bars represent the range of the two runs for each data point.

Of the gaseous emissions previously presented, none showed an overwhelming difference between the algal biodiesels and the other types of biodiesel. The hazardous air pollutant formaldehyde does show a clear difference between the more traditional feedstocks and the algae-based fuels. For all loads and blends, the algal biodiesels produced more formaldehyde than all other biodiesel blends.

Prior studies have not shown consistent trends on whether aldehydes increase or decrease with the use of biodiesel. The majority of studies have shown that aldehyde emissions decrease with the use of biodiesel but some studies have reported the opposite effect (Szybist, Song, Alam, & Boehman, 2007), (Graboski & McCormick, 1998). Some more recent studies have found a decrease in formaldehyde emissions, but an increase in acetaldehyde emissions (Di, Cheung and Huang 2009), (He, et al. 2009). The soy and canola biodiesel blends tested in this study show a decrease in formaldehyde at both loads and since all previous studies looking at the relationship

between biodiesel and aldehydes have been performed with soy or canola biodiesel, the results presented here are consistent with the majority of previous tests that reported decreased aldehyde emissions. Although formaldehyde is not currently a regulated emission for engines of this size, formaldehyde is classified as an air toxin by the EPA, so it could become a regulated compound in the future (The Clean Air Act 1990). Accordingly, the increased formaldehyde emissions observed in the study for both algal methyl ester formulations may require further study.

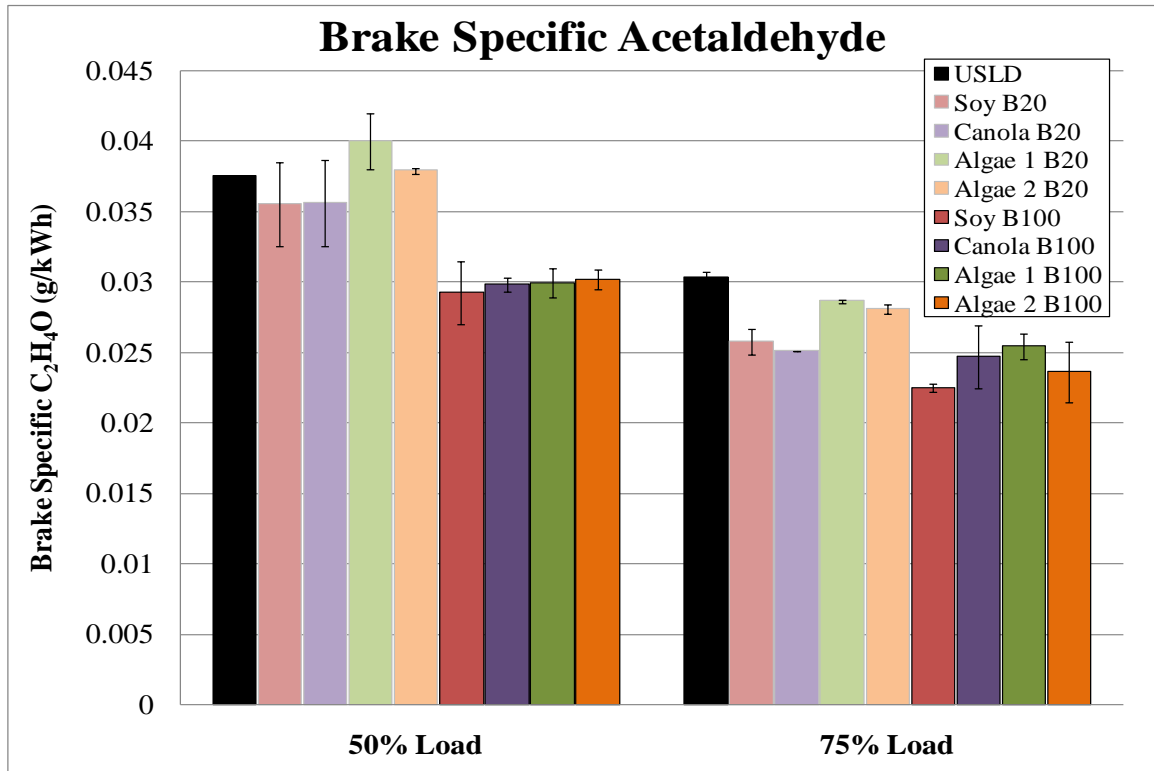


Figure 5.18 - Brake specific acetaldehyde emissions (g/kW-hr) for John Deere 4024T engine for 9 different fuel types at rated speed (2400 RPM) and 50% and 75% load.

At the lower load, all the types of B100 biodiesel produce roughly the same amount of acetaldehyde, about 20% less than the level produced by ULSD. Canola B100 and Algae 2 B100 produce more slightly acetaldehyde at 75% load than the other biodiesel fuels, but still decrease the acetaldehyde emissions relative to ULSD by 16%. Aside from Algae 1 B20 and Algae 2 B20 at 50% load, all biodiesel blends reduced the acetaldehyde in the exhaust with respect to ULSD.

Similar to formaldehyde, previous studies have not produced consistent results with respect to acetaldehyde emissions from biofuels.

Both of these aldehydes are considered hazardous air pollutants by the Environmental Protection Agency. The Clean Air Act of 1990 identified 187 hazardous air pollutants (HAP) that cause serious health problems like cancer and birth defects or produce adverse environmental effects (The Clean Air Act 1990). These HAPs are managed by National Emission Standards for Hazardous Air Pollutants (NESHAP), which vary depending on the source category, such as dry cleaning industries or reciprocating internal combustion engines. Each source category has a different set of regulations for the likely HAPs produced by that industry. The standards for internal combustion engines only apply to engines greater than 500 hp (372 kW). For engines in the size range of the 4024T engine, no regulations govern the emission of aldehydes.

### 5.3 Particulate Matter Emissions

All particulate measurements were taken after the exhaust was diluted with clean air in the dilution tunnel so the cleanliness of the dilution tunnel and dilution air was measured by the SMPS on a daily basis. The results are shown in the table below and are compared to the same measurement taken for ULSD at 50% load. Based on the particle count, the dilution air is much cleaner than the laboratory air, as expected, and accounts for 1% of all particles measured by the SMPS.

**Table 5.1- Cleanliness of Laboratory Air and Dilution Tunnel**

	<b>Laboratory Air</b>	<b>Dilution Air</b>	<b>Typical Test (ULSD 50% Load)</b>
<b>Particle Count (#/cm<sup>3</sup>)</b>	16308	3325	331645
<b>% of typical test</b>	4.9 %	1.0 %	-

### 5.3.1 Total Mass Emissions

Similar to the normalization calculations used to convert the mole fraction of gaseous species in the exhaust to mass emissions, the total mass of particulate matter produced is also normalized to take into account differences in load and fuel composition. Teflon filters collected mass from the exhaust for 20 minutes for each test point, which can be expressed as a mass accumulation rate. A known volumetric flow rate of diluted exhaust passed over the filter, depositing the particles on the filter. The fraction of particulate matter in that filter sample line can be calculated as:

$$(5.5) \quad f_{pm,fs} = \frac{\dot{m}_{pm,fs}}{\dot{m}_{fs} + \dot{m}_{pm,fs}}$$

where  $\dot{m}_{pm,fs}$  is the mass flow rate of particulates in the filter sample line, equal to the mass on the filter divided by the sample time, and  $\dot{m}_{fs}$  the mass flow rate of the diluted exhaust air in the filter sample line. The latter quantity can be found using the following equation:

$$(5.6) \quad \dot{m}_{fs} = \rho_{dil.air} \cdot \dot{V}_{fs}$$

where  $\rho_{dil.air}$  is the density of the dilution air, found using the ideal gas law, and  $\dot{V}_{fs}$  the known volumetric flow rate of the dilution air passing over the filter. Other quantities needed for this calculation are the total mass flow rate of the exhaust and the dilution ratio. The dilution ratio,  $DR$ , was calculated within the LabVIEW program governing the dilution tunnel set up, based on the flow rate of the exhaust sample and the flow rate of the clean dilution air. Both flow rates were measured as volumetric flow rates and converted to mass flow rates using the idea gas law. The total mass flow rate of the exhaust from the isolated cylinder is found using the following equation:

$$(5.7) \quad \dot{m}_{exh} = \dot{m}_f(1 + A/F)$$

where  $\dot{m}_f$  is fuel flow rate to the isolated cylinder and  $A/F$  is the air-to-fuel ratio. The final equation involving the brake power generated by the isolated cylinder,  $\dot{W}_b$ , is given by:

$$(5.8) \quad BSE_{PM} = \frac{\dot{m}_{exh} \cdot f_{pm,fs} \cdot (DR + 1)}{\dot{W}_b}$$

This equation calculates the brake specific mass of particles present in the exhaust emitted by the single cylinder by taking into account the effects of sampling a small fraction of the exhaust and diluting it prior to the deposition of mass onto the filter. The following figure shows the results for total particulate matter mass emissions.

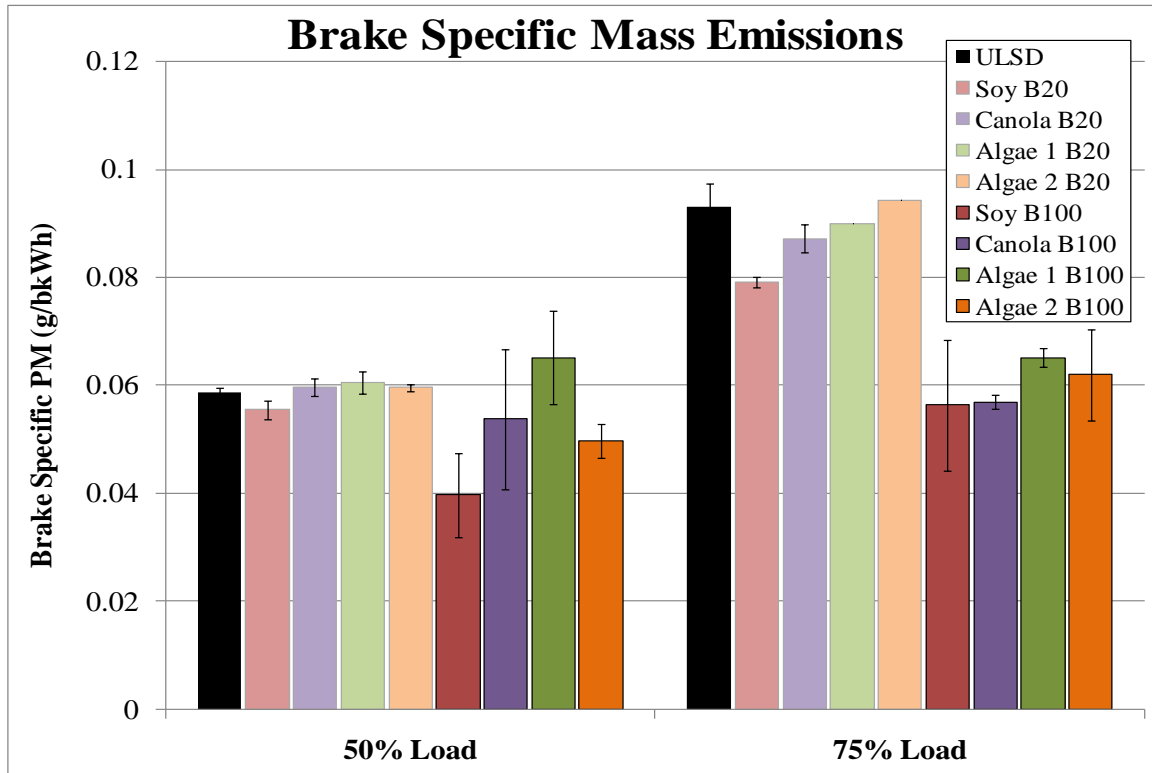


Figure 5.19 - Brake specific total particulate matter mass emissions (g/kW-hr) for John Deere 4024T engine for 9 different fuel types at rated speed (2400 RPM) and 50% and 75% load. The error bars represent the range of the two runs for each data point.

Generally, the use of biodiesel, in a blend with petroleum diesel or neat, results in decreased total PM mass emissions. This trend was observed in almost all the cases shown in Figure 5.19, with the exception of Algae 1 B100 at the lower load. The B20 blends resulted in little reduction in particulate mass, while most of the B100 biodiesel blends reduced the particulate matter mass, particularly at the higher load where reductions of 40% were observed.

Total PM mass emissions are currently regulated by the EPA. Current standards require less than 0.40 g/kWh of PM, decreasing to 0.30 g/kWh for engines made between 2008-2013, and decreasing further to 0.03 g/kWh for all engines made after 2013 (Standards on Performance for Stationary Compression Ignition Internal Combustion Engines 2006). As shown in Fig. 5.19, the PM mass emissions were measured to be well below the limit for the current and new regulations and are close to complying with the 2013 limitations. The slightly increased PM mass emissions of Algae 1 B100 at the lower load may be of concern but it is reiterated here that the tests were not conducted in strict accordance with EPA standards.

### **5.3.2 Scanning Mobility Particle Sizer Results**

The particulate matter size distribution as measured by the SMPS in the exhaust gases produced by the different fuels is shown in Figures 5.7 through 5.10. Figures 5.7 and 5.8 contain the PM size distribution for the B100 fuels in comparison with ULSD for the 50% and 75% loading conditions, respectively. Figures 5.9 and 5.10 contain the PM size distribution for the B20 fuels and ULSD for the 50% and 75% loading conditions, respectively. The PM size distribution is measured as the number of particles per volume and then normalized by the logarithm of the bin widths. This normalization accounts for the variation in bin sizes used to count the particles. Mobility diameter is shown on a log scale on the x-axis since there is a wide range of sizes measured.

The data shown in Figs. 5.20 to 5.23 represent averages of at least four data sets but error bars were omitted from the plots to keep them more readable. The standard deviation on the curves is generally small, but the error in the nucleation mode (the secondary peak observed at smaller diameters for some fuels) is much higher than in the rest of the data. As an example, Figure 5.24 contains a PM size distribution plot containing standard deviation error bars for Soy B100 at 50% and 75% load, respectively. Error bars for all the SMPS results were of the same order as those shown in Figure 5.24.

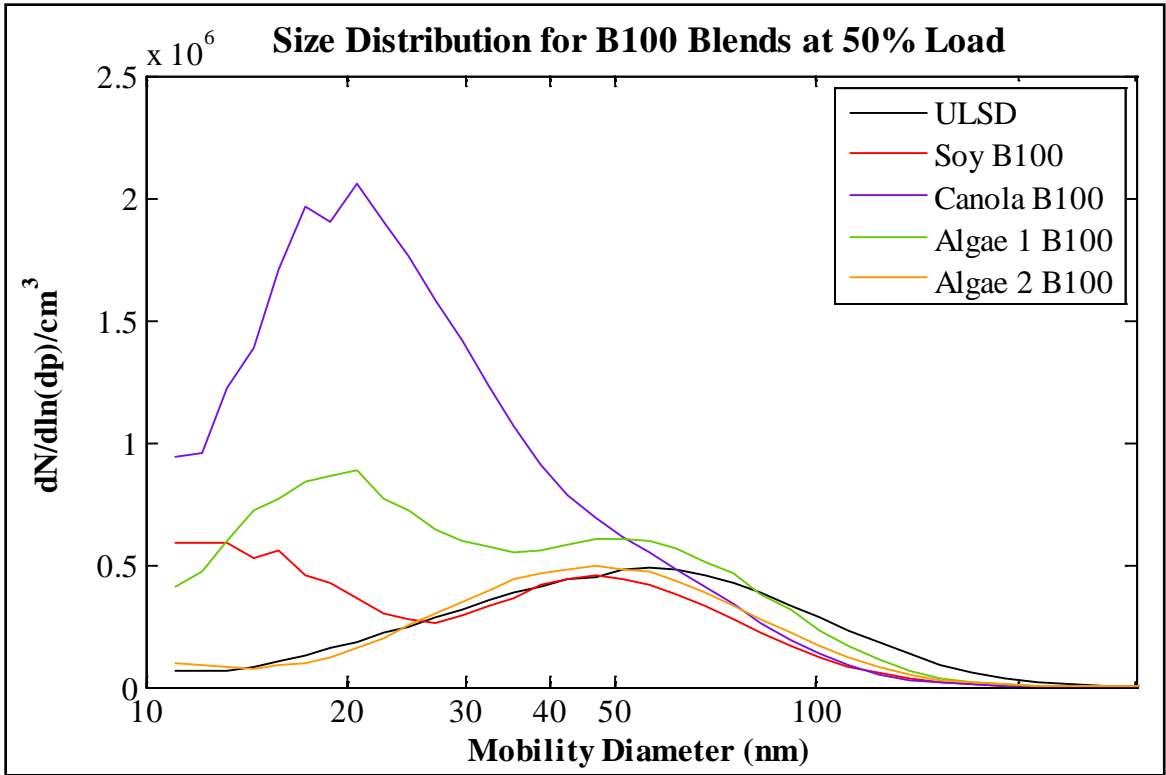


Figure 5.20 - SMPS size distribution for B100 blends at rated speed, 50% load.

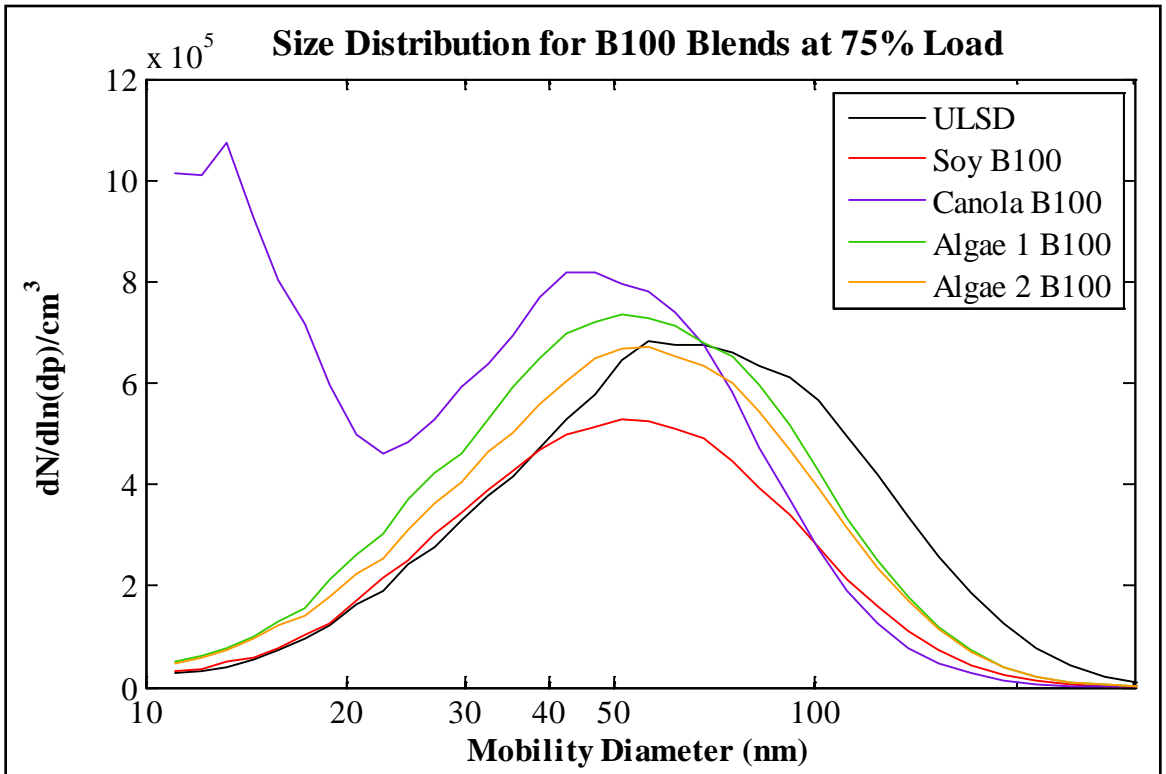


Figure 5.21 - SMPS size distribution for B100 blends at rated speed, 75% load.

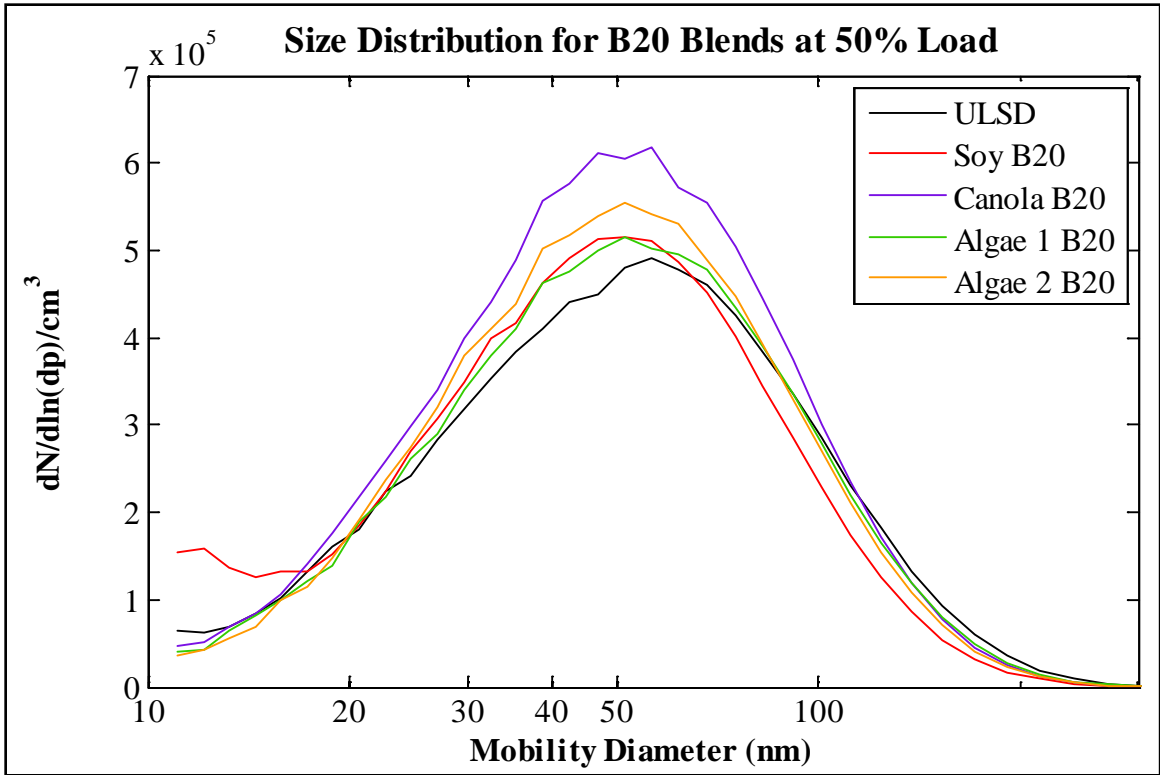


Figure 5.22 - SMPS size distribution for B20 blends at rated speed, 50% load.

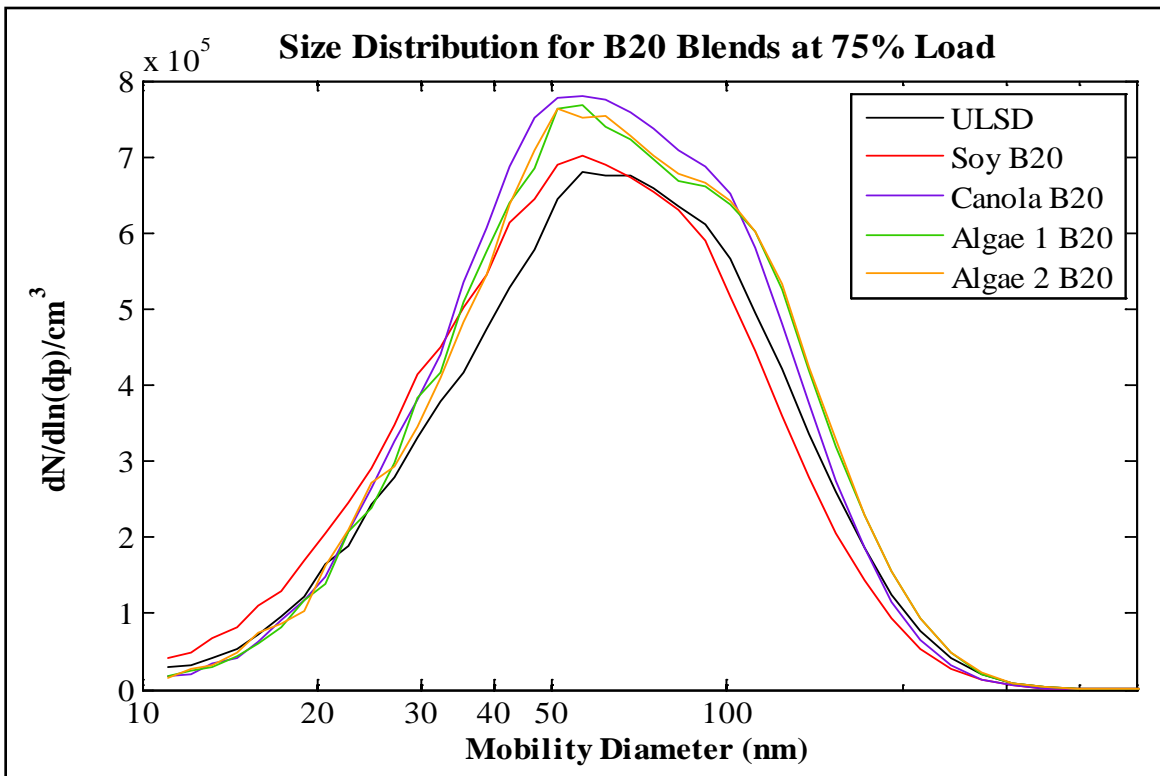
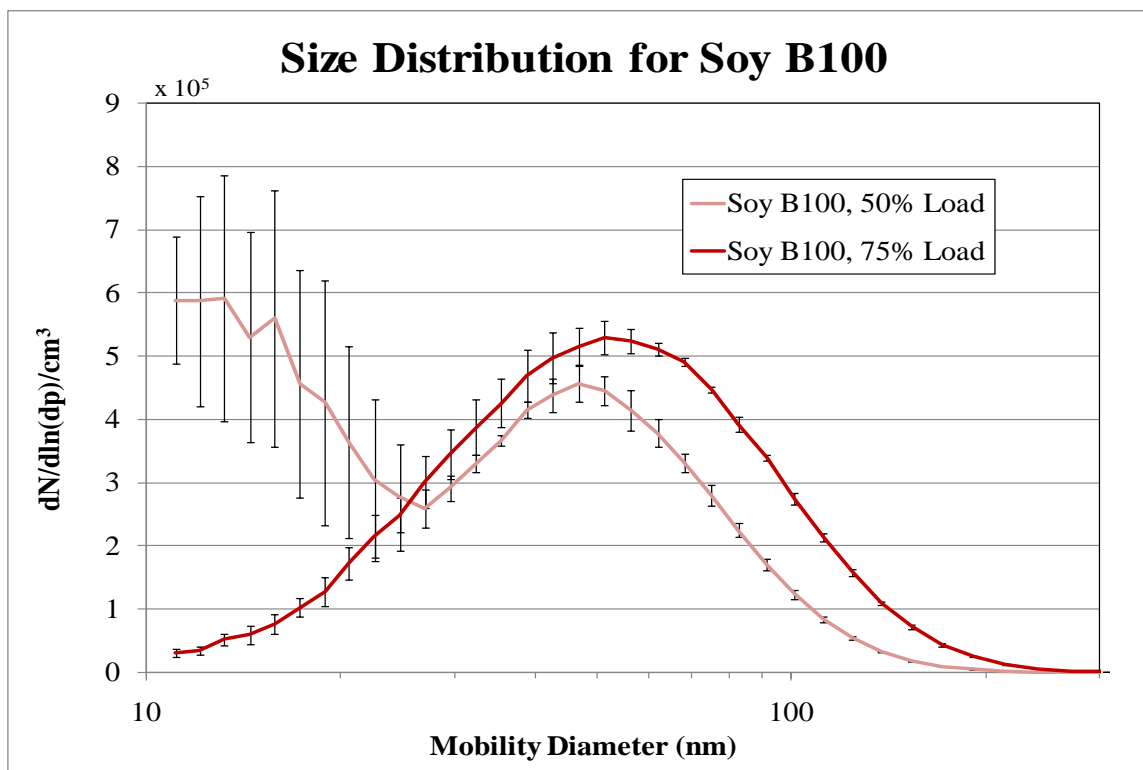


Figure 5.23 - SMPS size distribution for B20 blends at rated speed, 75% load.

Prior research, including studies performed at CSU using the same 4024T engine, have shown that soy methyl ester biodiesel produces particulates with a smaller mean mobility diameter than petroleum based diesel (Bennett, et al. 2008) (M. Bennett 2007). The results shown above are consistent with the previous studies. In fact, all of the methyl ester formulations resulted in a reduction in mean particle mobility diameter as signified by the leftward shift in the mode of the distribution for the methyl ester fuels in comparison with the ULSD. The reduction in mean particle mobility diameter is more prominently observed in the B100 blend particle distributions than in the B20 distributions. Canola biodiesel blends produced the highest concentration of particles at all blends and loads, in contrast to soy biodiesel that generated the lowest particle concentration in all cases. The two algal fuels produced particles with size distributions in between that of canola and soy biodiesel.

The B100 plots also contain some distributions with a second peak in the 10-30 nm range, which corresponds to particles in the nucleation mode. Combustion particles are comprised of many small particles that agglomerate to form larger complex particulates. The smaller nucleation particles are generally comprised of liquid volatile organic compounds and sulfur acid, as opposed to the larger particles found in the accumulation mode that are made up of agglomerated carbon particles (Casati, et al. 2007).

Figure 5.24 contains a plot of the PM size distribution for soy methyl ester B100 at 50% and 75% load, respectively. As noted above, the standard deviation on the curves is generally small, but the variability in the nucleation mode is much higher than in the accumulation mode for the rest of the data.



**Figure 5.24 - Size Distribution for Soy B100 at 50% and 75% load, with standard deviation error bars shown.**

The 75% load curve in Figure 5.24 has no nucleation mode and all the error bars are small. In contrast, the 50% load curve displays the nucleation mode seen in many of the B100 blends (see Figs. 5.20 and 5.21 above) and the error bars are substantially larger. While the standard deviation seen is not large enough to suggest that the nucleation mode is a product of instrument error, the large difference between multiple runs suggest that the nucleation mode is not as steady or repeatable as that of the accumulation mode.

The formation mechanism for the nucleation mode particles is not well understood. Some studies have shown that the sulfur content in the fuel is responsible for the formation of nucleation mode particles and other studies have shown that both low and high sulfur fuels can produce these particles, depending on the engine load (Kirchner, et al. 2009). Since biodiesel contains basically no sulfur, sulfur is likely not the reason that nucleation mode particles were seen in some B100 biodiesel blends. Other studies looking at nucleation mode particles found that their formation is highly dependent on temperature, humidity and dilution ratio (Casati, et al.

2007). Most likely, some combination of fuel chemistry and slight differences in the sampling environment are responsible for the formation of the nucleation mode particles.

It is notable, however, that at 50% the canola, soy and algae 1 methyl esters all exhibited a substantial nucleation mode peak, while at 75% load only the canola fuel exhibited the nucleation mode peak. These results suggest an area of future research as it is difficult to draw any conclusions as to why some of the methyl esters exhibited the large nucleation mode peaks and others did not. Impurities from the transesterification process are a consideration that should also be mentioned since the canola methyl esters and algal methyl esters were produced in-house. However, the soy methyl esters, which were produced commercially, also exhibited the nucleation mode peak. Moreover, the algal methyl esters were produced at the bench scale, while the canola methyl esters were produced in a large batch reactor. Therefore, since three separate transesterification systems all produced fuels that exhibited the nucleation mode peak it is not believed that the nucleation mode peaks are an artifact from impurities from a particular transesterification process.

### **5.3.3 Elemental and Organic Carbon**

The quartz filters used to capture the particulate matter were analyzed for their elemental and organic carbon content using a Sunset Labs OC/EC Analyzer located in the CSU Department of Atmospheric Science. A single, 2.27 cm<sup>2</sup> punch was analyzed from each quartz filter, but room was left for a second punch in case the first result was inconclusive. Since each fuel/load point was repeated twice, the results from the two quartz filters taken under the same engine condition and fuel type were averaged. To correct for the positive artifact, the organic carbon found on the main quartz filter due to adsorption of gaseous organic carbon was corrected for using the back quartz filter, which was located behind the Teflon filter and collected only the gaseous organic carbon that could bias the particulate organic carbon measurement. For each test point, the organic carbon found on the back filter was subtracted from the organic carbon

measurement from the front filter, resulting in a corrected organic carbon measurement:

$$(5.9) \quad M_{PM_{OC}} = M_{front_{OC}} - M_{back_{OC}}$$

Using the average elemental carbon mass and average corrected organic carbon mass, the brake specific EC and OC were calculated using a similar technique to that employed for the total brake specific PM emissions (as described in Section 5.3.1). Figures 5.25 and 5.26 show the breakdown between elemental (EC) and organic carbon (OC) for each fuel at both loads.

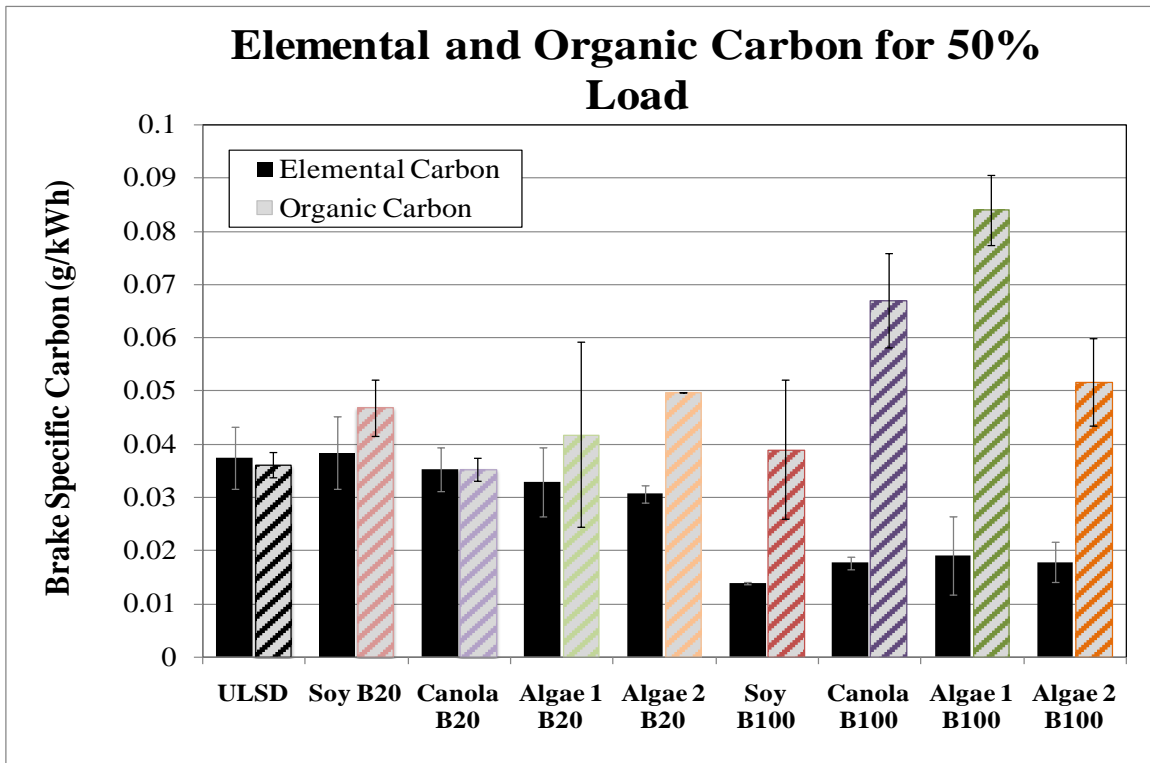


Figure 5.25 - Elemental and Organic Carbon for 9 different fuel types at rated speed and 50% load. The error bars represent the range of the two runs for each data point.

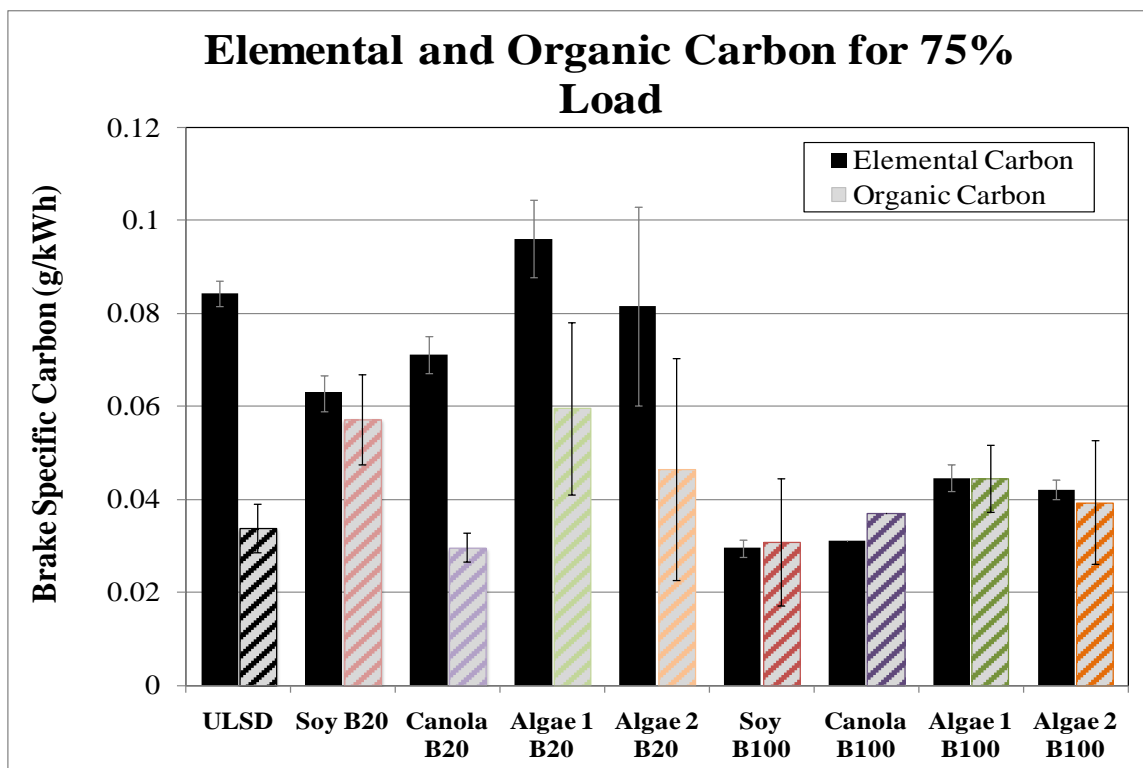


Figure 5.26 - Elemental and Organic Carbon for 9 different fuel types at rated speed and 75% load. The error bars represent the range of the two runs for each data point.

For both loads, the use of B100 biodiesel decreased the elemental carbon in the particulate matter. The organic carbon produced by the B100 fuels increases at the 50% load but remains relatively constant at 75% load. Elemental carbon produced by the B20 blends is on a similar level to ULSD, but OC generally increases. Of the B100 methyl esters, Algae 1 B100 produced the most EC and OC, producing more OC at 50% than any of the other fuels. Algae 1 B20 also produced the highest EC and OC at 75% load, while Soy B20 and Algae 2 B20 produced the most OC and Canola B20 had the most EC at 50% load.

These results are consistent with previous studies that also have seen EC decrease and OC increase with increasing biodiesel content in fuel (Bennett, et al. 2008) (Cheng, Buchholz and Dibble 2003). Bennett and coworkers used the same engine and same dilution tunnel set up, but they collected particulate matter for several hours (M. Bennett 2007). As a result, she captured substantially more elemental carbon and less organic carbon relative to the EC collected. The

study performed by Cheng reported similar levels of EC and OC as the results for the soy methyl esters in Figure 5.25. They found a larger OC to EC ratio for the Soy B100 fuel that they tested, but the order of magnitude was consistent with the results reported here.

The fact that biodiesel fuels tend to increase organic carbon could mean that particulate matter originating from biodiesel exhaust is more harmful than that of petroleum diesel, since organic carbon includes many carcinogenic and toxic species. However, a study performed with diesel passenger cars found the same increase in organic carbon between diesel and biodiesel but a closer look at the SOF revealed that biodiesel exhaust contained less of the potentially carcinogenic PAHs and nitro-PAHs (Karavalakis, Stournas and Bakeas 2009). They also found that the majority of the organic carbon mass was due unburned methyl esters. Particulate matter can also contain mutagenic organic carbon species, also potential carcinogens, but these too have been found in equal or lesser concentrations in biodiesel exhaust relative to petroleum diesel exhaust (Krahl, et al. 2009). This is currently an area of active research and further studies will be needed to understand the complete picture, but early results indicate that the increase in organic carbon in biodiesel exhaust does not lead to an increase in harmful carcinogenic compounds.

#### **5.3.4 AMS Results**

The AMS provided detailed information about the chemical composition of the particulate matter, with the exception of refractory material such as metals and elemental carbon. As was previously discussed in Section 2.4.6, the volatile and semi-volatile particulate species are ionized and fragmented before entering the mass spectrometer and the pieces of the original molecules are identified based on their mass-to-charge ratios. The results can be broken down in varying degrees of precision. All of the ions measured for each fuel can be broken down into organic and inorganic components. The organic carbon content can be broken down into hydrocarbons ( $C_xH_y$ ) and oxygenated hydrocarbons ( $C_xH_yO_z$ ) and the inorganic content can be

divided into sulfate, nitrate, and ammonium. Each of these categories can be segregated further into the individual molecule fragments. The AMS is also capable of measuring the particulate size distribution but the range of sizes detectable by the AMS, from 35 nm to 1  $\mu\text{m}$ , does not include the smallest particles that are within the measurable range for the SMPS, so the AMS particle size data is not reported here. Figures 5.27 and 5.28 show the AMS results, divided into hydrocarbons, oxygenated hydrocarbons and inorganic species. The sum of hydrocarbons and oxygenated hydrocarbons is equal to the total organic carbon content. Figures 5.29 and 5.30 show the breakdown of inorganic content between nitrate, sulfate and ammonium.

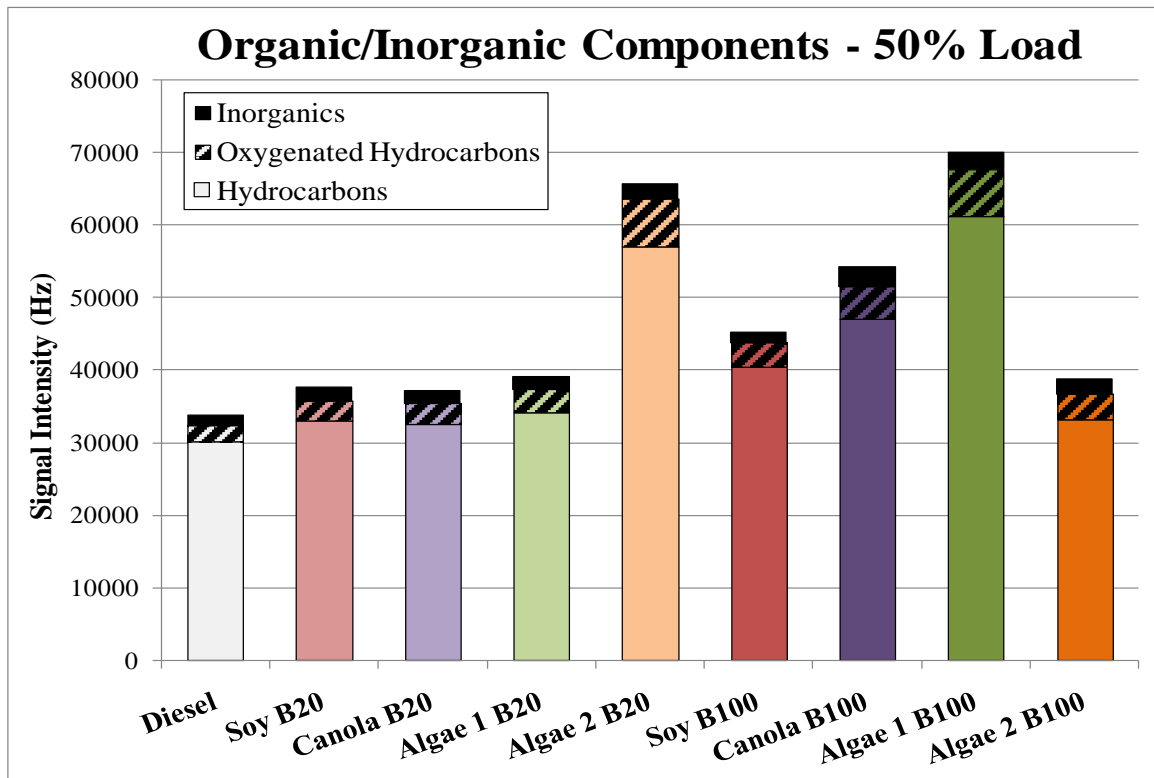


Figure 5.27. Break down of organic carbon for each fuel at 50% load.

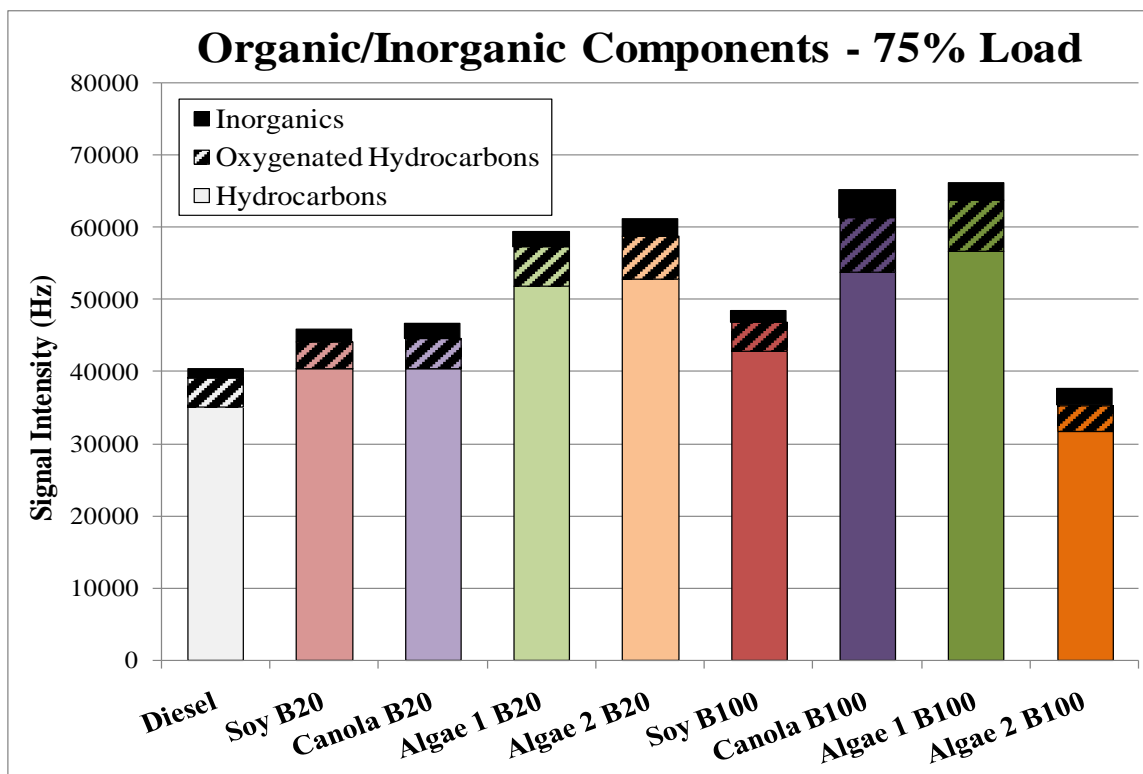


Figure 5.28 - Break down of organic carbon for each fuel at 75% load.

The results for the organic and inorganic content are shown in Figures 5.27 and 5.28 above, compared on the basis of signal intensity. It should be noted that these measurements are not normalized by engine load, so there will be some differences between the organic carbon results shown in Figures 5.25 and 5.26. At 50% load, ULSD produces the least OC, followed by the B20 blends, with the exception of Algae 2 B20. Of the B100 blends, Algae 2 B100 produces the lowest amount of OC, followed by Soy B100. Algae 1 B100 produces the most OC of any of the fuels at the lower load. These trends are similar to the filter-based OC measurements, except that Soy B100 produced the lowest OC in those tests, followed by Algae 2 B100. The amount of oxygenated hydrocarbons and inorganic species produced do not vary significantly between fuels. Similar trends are seen at the higher load, except that Algae 2 B100 produces the least amount of OC for any fuel. Algae 1 B20 and Algae 2 B20 both produce a large amount of OC relative to the other B20 blends. Canola B100 and Algae 1 B100 are the highest OC producers of the B100 blends.

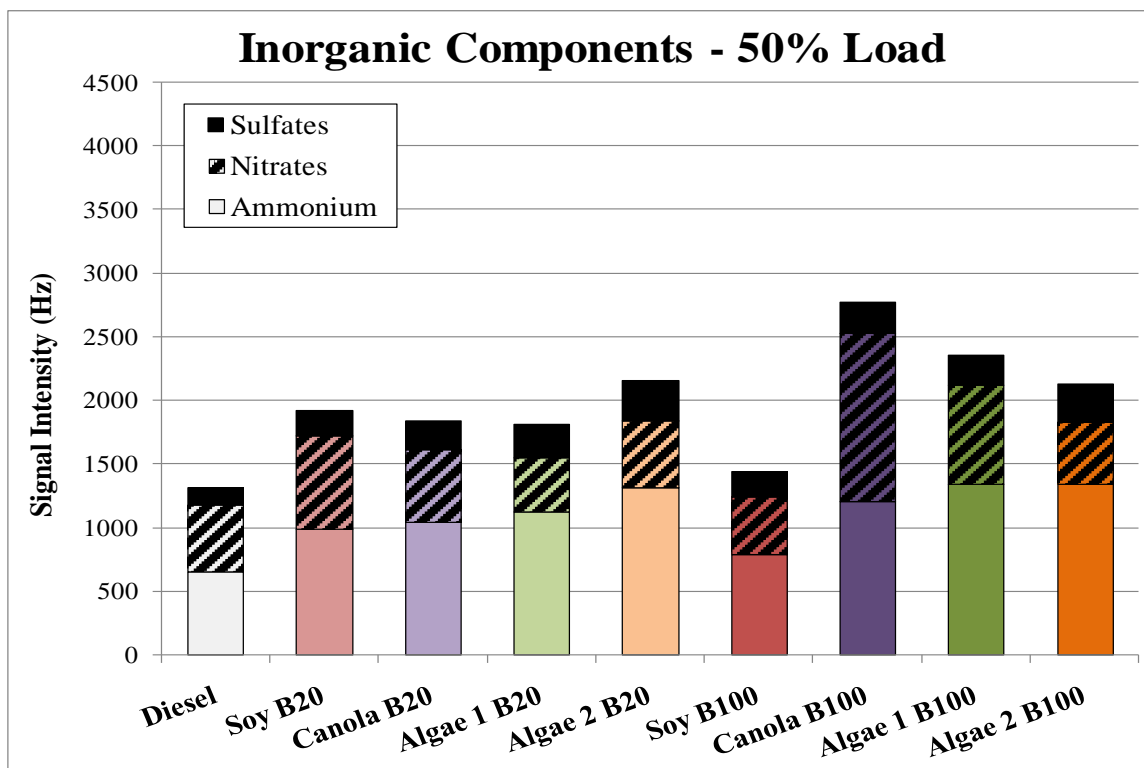


Figure 5.29 - Inorganic Components in Organic Carbon at 50% Load.

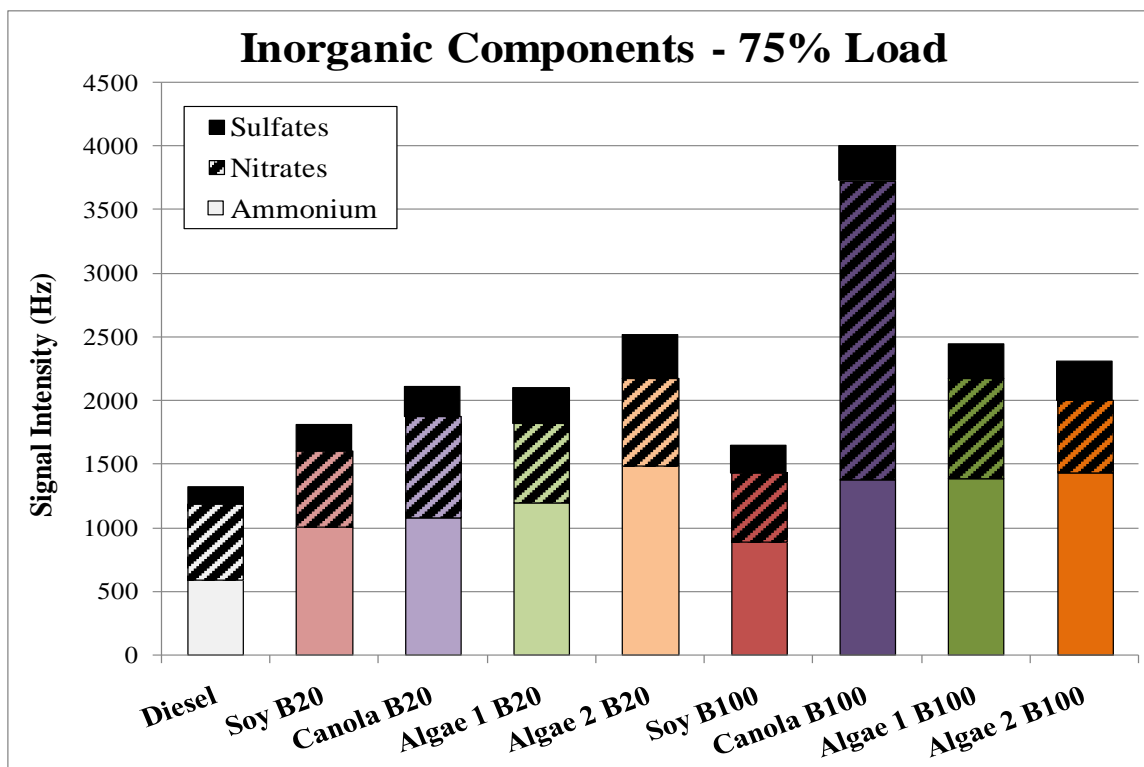


Figure 5.30 - Inorganic Components in Organic Carbon at 75% Load.

Relative to the organic carbon content of the exhaust, the inorganic species make up a relatively small fraction of the volatile and semi-volatile exhaust products. For both loads, ULSD and Soy B100 were the lowest producers of inorganic species and Canola B100 is the highest. The nitrates produced by Canola B100 are significantly higher than for the other fuels, making it the largest source for total inorganic species.

The AMS can be used to identify ions from the exhaust that differ between ULSD and the biodiesel blends. One such molecular fragment, as identified by the mass to charge ratio, is shown below in Figure 5.31. Specifically, the two peaks located at approximately  $m/z = 59$  are notable because the diesel exhaust (as signified by the black line in Figure 5.31) produces less of this molecular fragment in comparison with all of the methyl esters. This result has the potential to be of use for atmospheric scientists as a way of uniquely identifying the source of atmospheric particulate matter. Specifically, if diesel particulate matter contains little or no oxygenated hydrocarbon molecular fragments at 59.0114 (as suggested by Figure 5.31), then it may be possible to distinguish primary atmospheric diesel particulate matter from other sources such as biomass burning, or secondary organic aerosols.

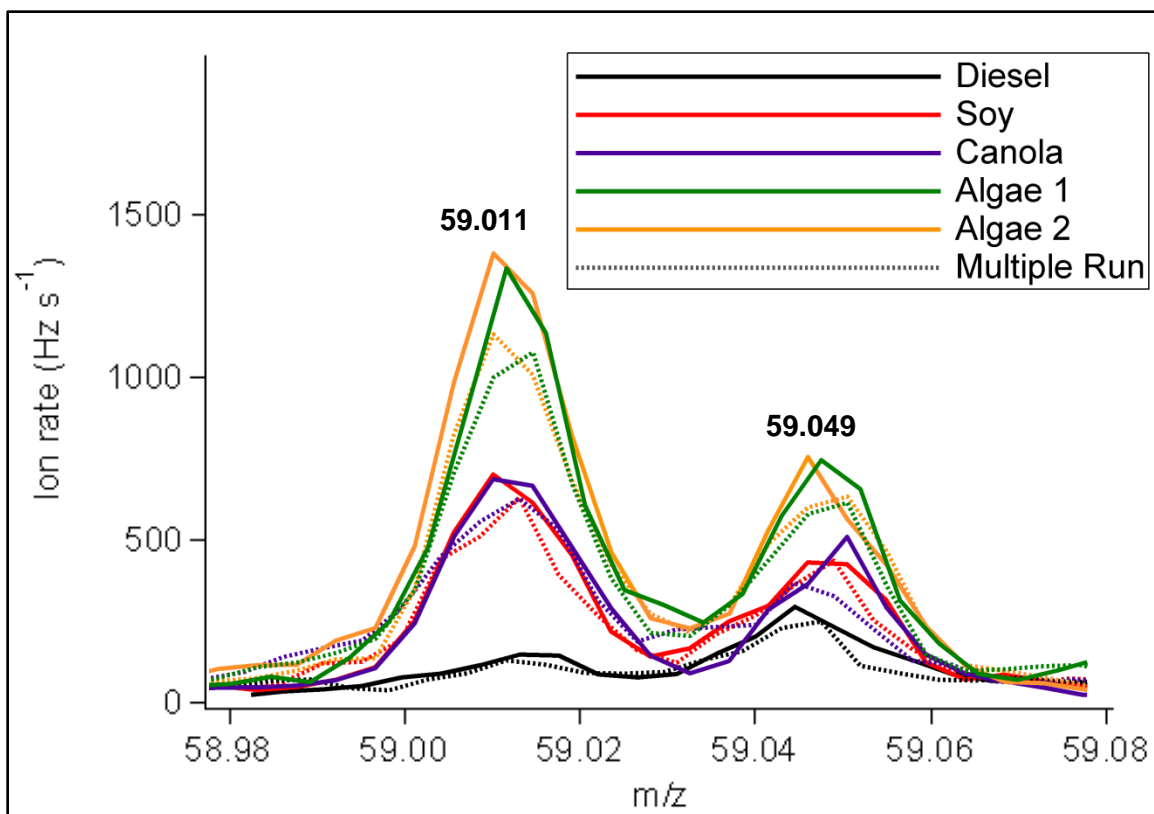
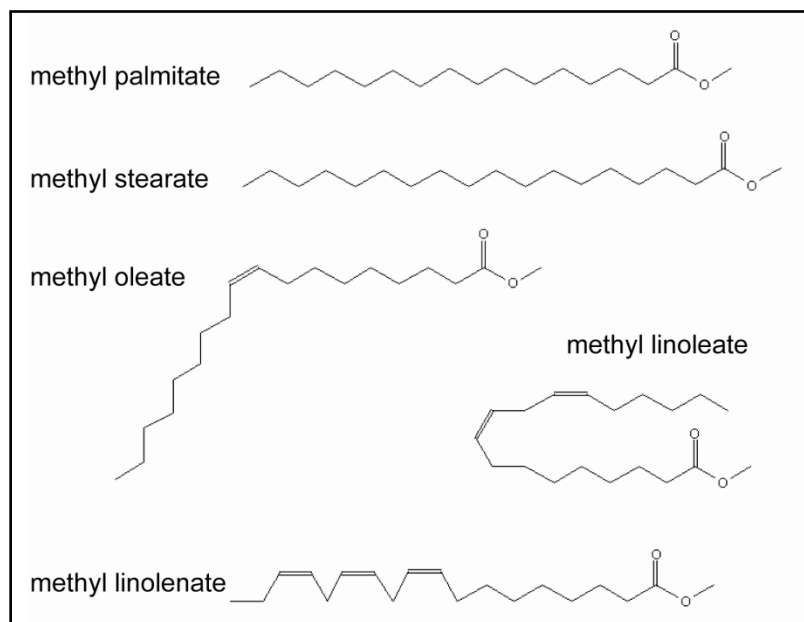


Figure 5.31 – Two peaks in ion concentration near mass-to-charge ratio of 59 for B20 blends at 75% load.

Part of the difficulty of using the AMS is taking a precise mass-to-charge ratio and making an educated guess as to what combination of atoms result in that mass. One likely combination that could produce the exact mass of these peaks is  $C_2H_3O_2$ . All methyl ester molecules have a  $C(=O)OCH_3$  group at one end (See Figure 5.32 below), so it is reasonable to expect that if any unburned fuel is present in the particulate matter in methyl ester exhaust that this fragment would be present in the AMS data. Conversely, even though the AMS data from petroleum diesel exhaust contains some oxygenated hydrocarbon fragments (see Figures 5.27 and 5.28), these ions cannot be fragments of unburned fuel since the fuel itself contains little or no oxygen.

The set of curves shown in Figure 5.31 is a compilation of results from ULSD and the B20 biodiesel blends at 75% load. The other blends and loads show similar results. As mentioned above, these peaks could be used to identify atmospheric particulate matter directly to

biodiesel exhaust, as distinguished from that created by petroleum diesel. Recent results suggest, however, that other types of biomass burning also produce the  $C_2H_3O_2$  fragment (Lee and Collett 2009). However, the fact that petroleum diesel combustion does not produce this peak may still be a useful result.



**Figure 5.32. Examples of the molecular structure of methyl esters.**

## 6. CONCLUSIONS

This work was intended to evaluate whether there were any substantial differences between emissions produced by algae-based biodiesel, more traditional biodiesel feedstocks, and petroleum diesel. Both the gaseous components and particulate content in the exhaust were evaluated using several instruments. Based on earlier research, the highly unsaturated content in algal oil could lead to an increase in  $\text{NO}_x$  relative to soy or canola biodiesel. Most results for the algae-based biodiesels are similar to the other biodiesels but in the case of  $\text{NO}_x$ , the algae-based biodiesel reduced  $\text{NO}_x$  at both loads. The premixed burn fraction, determined using the heat release rate curves, correlate well with  $\text{NO}_x$  levels, though there are probably other factors that contribute to  $\text{NO}_x$  production in biodiesel fuels. The algae-based biodiesel produced small increases in THC and larger increases in formaldehyde and  $\text{NO}_2$ .

Total particulate mass decreased for B100 biodiesel blends, with the algae-based methyl esters producing slightly more than the other B100 fuels. The use of biodiesel increased the organic carbon content in the PM and increased elemental carbon. The two algal fuels produced slightly higher OC levels at both loads and blends. This trend was seen both with the quartz filters analyzed for EC/OC break down and in the AMS results. Since the AMS detected high concentrations of ions at a mass-to-charge ratio of  $m/z = 59$  for the biodiesel fuels but not for petroleum diesel, this could be a possible marker for differentiating biodiesel fuel combustion from diesel combustion.

## 6.1 Recommendations for Future Work

In the short time between the planning stages of the project and the completion of this thesis, the development of algal biofuels has progressed rapidly. Solix Biofuels has built a pilot plant in Durango, CO that is now producing enough algal oil to be used in engine testing. The obvious next step is to run similar tests on actual algal biodiesel. Another change that would improve the repeatability and comparability of these results would be to repeat these tests with the entire engine running on the fuel of interest. Using a 2007/2012 emissions compliant, common rail engine would be preferable, as the results would be representative of the most common engine moving forward. Running the entire engine on the fuel of interest would enable the sampling specifications to be met and thus the results should be comparable to other studies.

Much of the motivation for this work was to evaluate how algal biodiesel may affect the health effects associated with diesel exhaust. While it is possible to make some educated guesses based on particle size and chemical content in the exhaust, it is still difficult to know if there are other factors that could alter the overall effects. In order to get a clearer picture of the health effects, another graduate student is working on building a device that will deposit exhaust particles onto living human lung tissue. The inflammation response of the lung tissue and protein assays will be used to gauge the health of the cells as they are exposed to exhaust from different fuels.

Additionally, the results from this study highlight the lack of understanding on how the molecular structure of a fuel affects the production of  $\text{NO}_x$ . All previous research suggested that increasing the number of double bonds in a methyl ester fatty acid would increase the  $\text{NO}_x$  produced, but that is not what these results show. A more detailed look at the chemical kinetics could provide some insight into what on the molecular level contributes to  $\text{NO}_x$  production. That may help identify species of algae that produce oil optimal for fuel production. A rapid compression machine (RCM) will be used to look at the chemical kinetics of the algal fuel's

combustion. A homogeneous mixture of fuel and air is injected into the RCM and a single compression stroke acts on the fuel/air mixture. Combustion occurs as it would in an engine, but all of the engine complications are removed, including the expansion stroke. Once the compression stroke occurs, high speed sampling equipment, including the Fast NO<sub>x</sub> analyzer, will look at how the species evolve during combustion. Many variables that affect combustion, like the compression ratio and the degree of mixing, can be precisely controlled with the RCM to get a complete picture of the combustion process. The combination of these various experiments should shed more light on the combustion of biodiesel and how algal fuel may or may not affect those processes.

Lastly, the AMS has the potential to provide more insight into the organic carbon content of biodiesel exhaust. Further investigation into chemical signatures found in biodiesel exhaust but not in petroleum diesel exhaust, or vice versa, could provide valuable information on the differences in the organic carbon emitted by both sources. Additionally, the PM exhaust from other types and sizes of diesel engines should be studied with the AMS to ensure the trends seen with the John Deere 4024T engine are not engine-specific.

## 7. REFERENCES

- Alander, T., A. Leskinen, T. Raunemaa, and L. Rantanen. "Characterization of Diesel Particles: Effects of Fuel Reformation, Exhaust Aftertreatment, and Engine Operation on Particle Carbon Composition and Volatility." *Environmental Science and Technology*, 2004: 2707-2714.
- Allan, R., J. Williams, J. Rogerson, A. Schonborn, and N. Ladommatos. *Effect of the Molecular Structure of Individual Fatty Acid Alcohol Esters (Biodiesel) on the Formation of NOx and Particulate Matter in the Diesel Combustion Process*. SAE 2008-01-1578., SAE International, 2008.
- Appenzeller, Tim. "The End of Cheap Oil." *National Geographic*, 2004.
- Ban-Weiss, G., B. Buchholz, and R. Dibble. "A Numerical Investigation into the Anomalous Slight NOx Increase when Burning Biodiesel." *Fuel Processing Technologies*, 2007: 659-667.
- Bennett, M., J. Volckens, R. Stanglmaier, A. McNichol, W. Ellenson, and C. Lewis. "Biodiesel Effects on Particulate Radiocarbon Emissions from a Diesel Engine." *Aerosol Science*, 2008: 667-678.
- Bennett, Maren. "Emissions from a Diesel Engine Operating with Soy-Based Biodiesel Fuel." Master's Thesis, 2007.
- Burtscher, H. "Physical Characterization of Particulate Emissions from Diesel Engines: A Review." *Aerosol Science*, 2005: 896-932.
- Casati, R., S. Volker, R. Vogt, and T. Benter. "Measurement of Nucleation and Soot Mode Particle Emission from a Diesel Passenger Car in Real World and Laboratory in Situ Diltuion." *Atmospheric Environment*, 2007: 2125-2135.
- Chapman, L. "Transport and Climate Change: A Review." *Journal of Transport Geography*, 2007: 354-367.
- Cheng, A. S., A. Upatnieks, and C. J. Mueller. "Investigation of the Impact of Biodiesel Fuelling on NOx Emissions Using an Optical Direct Injection Diesel Engine." *International Journal of Engine Research*, 2006: 297-318.
- Cheng, A.S., B.A. Buchholz, and R.W. Dibble. *Isotopic Tracing of Fuel Carbon in the Emissions of Compression-Ignition Engine Fueled with Biodiesel Blends*. SAE 2003-01-2282, SAE International, 2003.
- Chisti, Y. "Biodiesel from Microalgae." *Biotechnology Advances*, 2007: 294-306.

- Choi, C.Y., G.R. Bower, and R.D. Reitz. "Effect of Biodiesel Blended Fuels and Multiple Injections on DI Diesel Engines." *SAE 970218*, 1997.
- Chung, A., A. Lall, and S. Paulson. "Particulate Emissions by a Small Non-road Diesel Engine." *Atmospheric Environment*, 2008: 2129-2140.
- Congress, 110th United States. "Energy Independence and Security Act of 2007." House Bill H.R.6, 2007.
- Demirbas, A. "Importance of Biodiesel as Transportation Fuel." *Energy Policy*, 2007: 4661-4670.
- Di, Y., C. Cheung, and Z. Huang. "Experimental Investigation on Regulated and Unregulated Emissions of a Diesel Engine Fueled with Ultra-low Sulfur Diesel Fuel Blended with Biodiesel from Waste Cooking Oil." *Science of the Total Environment*, 2009: 835-846.
- Diaz-Robles, L., J. Fu, and G. Reed. "Modeling and Source Apportionment of Diesel Particulate Matter." *Environment International*, 2008: 1-11.
- Energy Information Administration. *Crude Oil Production History*. U.S. Government, 2009.
- EPA. *A Comprehensive Analysis of Biodiesel Impacts on Exhaust Emissions*. EPA 420-P-02-001, 2002.
- EPA. "Title 40: Protection of Environment; Part 60: Standards of Performance for New Stationary Sources." 40 CFR Part 60, 2007.
- Fernandez-Feiriz, M., et al. "Biomass Production and Variation in the Biochemical Profile of Seven Species of Marine Microalgae." *Aquaculture*, 1989: 17-37.
- Gaffney, J., and N. Marley. "The Impacts of Combustion Emissions on Air Quality and Climate - From Coal to Biofuels and Beyond." *Atmospheric Science*, 2009: 23-36.
- Graboski, M., and R. McCormick. "Combustion of Fat and Vegetable Oil Derived Fuels in Diesel Engines." *Progress in Energy and Combustion Science*, 1998: 125-164.
- Graboski, M., R. McCormick, T. Alleman, and A. Herring. *The Effect of Biodiesel Composition on Engine Emissions from a DDC Series 60 Diesel Engine*. NREL/SR-510-31461, NREL, 2003.
- Graedel, T.E., and B.R. Allenby. *Design for the Environment*. Prentice Hall, 1996.
- Grundwald, M. "The Clean Energy Scam." *Time Magazine*, March 27, 2008.
- He, C., et al. "Comparison of Carbonyl Compounds Emissions from Diesel Engine Fueled with Biodiesel and Diesel." *Atmospheric Environment*, 2009: 3657-3661.
- Heywood, John. *Internal Combustion Engine Fundamentals*. New York: McGraw-Hill, 1988.
- Hinds, William. *Aerosol Technology*. New York: John Wiley and Sons, Inc. , 1999.
- Holden, Amanda. *Estimating Contributions of Primary Biomass Combustion to Fine Particulate Matter at Sites in the Western United States*. Fort Collins: Colorado State University Atmospheric Science Department, 2008.

International Organization for Standards. "Reciprocating Internal Combustion Engines - Exhaust Emissions Measurement; Part 4: Test cycles for different engine applications." ISO 8178-4, 1996.

IPCC. *Climate Change 2007*. Fourth Assessment Report, United Nations, 2007.

Jacquot, J. "Five Companies Making Fuel From Algae Now." *Popular Mechanics*, 2009.

John Deere Power Systems. "Technical Manual for Powertech 2.4L & 3.0L Diesel Engines." 2006.

Jung, H., D. Kittelson, and M. Zachariah. "Characteristics of SME Biodiesel-Fueled Diesel Particle Emissions and the Kinetics of Oxidation." *Environmental Science & Technology*, 2006: 4949-4955.

Karavalakis, G., S. Stournas, and E. Bakeas. "Effects of Diesel/Biodiesel Blends on Regulated and Unregulated Pollutants from a Passenger Vehicle Operated over the European and the Athens Driving Cycles." *Atmospheric Environment*, 2009: 1745-1752.

Kirchner, U., V. Scheer, R. Vogt, and R. Kagi. "TEM Study on Volatility and Potential Presence of Solid Cores in Nucleation Mode Particles from Diesel Powered Passenger Cars." *Aerosol Science*, 2009: 55-64.

Kittelson, D. "Engines and Nanoparticles: A Review." *Journal of Aerosol Science*, 1998: 575-588.

Knothe, G., C. Sharp, and T. Ryan. "Exhaust Emissions of Biodiesel, Petrodiesel, Neat Methyl Esters, and Alkanes in a New Technology Engine." *Energy & Fuels*, 2006: 403-408.

Konnov, A.A. "Implementation of the NCN Pathway of Prompt-NO Formation in the Detailed Reaction Mechanism." *Combustion and Flame*, 2009: 2093-2105.

Krahl, J., et al. "Comparison of Exhaust Emissions and their Mutagenicity from the Combustion of Biodiesel, Vegetable Oil, Gas-to-Liquid and Petrodiesel Fuels." *Fuel*, 2009: 1064-1069.

Lapuerta, M., O. Armas, and J. Rodriguez-Fernandez. "Effect of Biodiesel Fuels on Diesel Engine Emissions." *Progress in Energy and Combustion Science*, 2008: 198-223.

Lee, T., and J. Collett. "Personal Communication." 2009.

Maricq, M. "Chemical Characterization of Particulate Emissions from Diesel Engines: A Review." *Aerosol Science*, 2007: 1079-1118.

*Martek Biosciences Corporation*. 2009. <http://www.lifesdha.com/Finding-lifesDHA-/Partner-Products/tabid/129/Default.aspx> (accessed 2009).

McCormick, R., J. Alvarez, and M. Graboski. *NOx Solutions for Biodiesel*. NREL/SR-510-31465, 2003.

McCormick, R., M. Graboski, T. Alleman, A. Herring, and K.S. Tyson. "Impact of Biodiesel Source Material and Chemical Structure on Emissions of Criteria Pollutants from a Heavy-Duty Engine." *Environmental Science and Technology*, 2001: 1742-1747.

- McCormick, R.L., A. Williams, J. Ireland, M. Brimhall, and R.R. Hayes. *Effects of Biodiesel Blends on Vehicle Emissions*. NREL/MP-540-40554, NREL, 2006.
- Moosmuller, H., et al. "Time Resolved Characteristics of Diesel Particulate Emissions." *Environmental Science and Technology*, 2001: 1935-1942.
- Moser, B.R. "Influence of Blending Canola, Palm, Soybean, and Sunflower oil Methyl Esters on Fuel Properties of Biodiesel." *Energy & Fuels*, 2008: 4301-4306.
- Mueller, C., A. Boehman, and G. Martin. *An Experimental Investigation of the Origin of Increased NOx Emissions when Fueling a Heavy-Duty Compression Ignition Engine with Soy Biodiesel*. SAE 09SFL-0093, SAE, 2009.
- National Biodiesel Board. *U.S. Biodiesel Production Capacity*. U.S. Biodiesel Board, 2009.
- Patterson, J., M. Hassan, A. Clarke, G. Shama, K. Hellgardt, and R. Chen. "Experimental Study of DI Diesel Engine Performance Using Three Different Biodiesel Fuels." *SAE 2006-01-0234*, 2006.
- Peters, A., et al. "Air Pollution and Incidence of Cardiac Arrhythmia." *Epidemiology*, 2000: 11-17.
- Sheehan, J., Dunahey, T., Benemann, J. and Roessler, P. *A Look Back at the US Department of Energy's Aquatic Species Report*. NREL/TP-580-24190, NREL, 1998.
- Sheehan, J., V. Camobreco, J. Duffield, M. Graboski, and H. Shapouri. *An Overview of Biodiesel and Petroleum Diesel Life Cycles*. NREL/TP-580-24772, NREL, 1998.
- Standards on Performance for Stationary Compression Ignition Internal Combustion Engines*. 40 CFR Parts 60, 85 et al., Environmental Protection Agency, 2006.
- Szybist, J., A. Boehman, J. Taylor, and McCormick. "Evaluation of Formulation Strategies to Eliminate the Biodiesel NOx Effect." *Fuel Processing Technology*, 2005: 1109-1126.
- Szybist, J., J. Song, M. Alam, and A. Boehman. "Biodiesel Combustion, Emissions and Emission Control." *Fuel Processing Technology*, 2007: 679-691.
- Szybist, J.P., and A.L. Boehman. "Behavior of a Diesel Injection System with Biodiesel Fuel." *SAE 2003-01-1039*, 2003.
- The Clean Air Act*. Environmental Protection Agency, 1990.
- Tiwari, A.K., A. Kumar, and H. Raheman. "Biodiesel Production from Jatropha Oil (*Jatropha curcas*) with High Free Fatty Acids: An Optimized Process." *Biomass & Bioenergy*, 2007: 569-575.
- Turns, Stephen. *An Introduction to Combustion*. Boston: McGraw-Hill, 2000.
- U.S. Department of Energy. *National Algal Biofuels Technology Roadmap*. DOE Biomass Program, 2009.

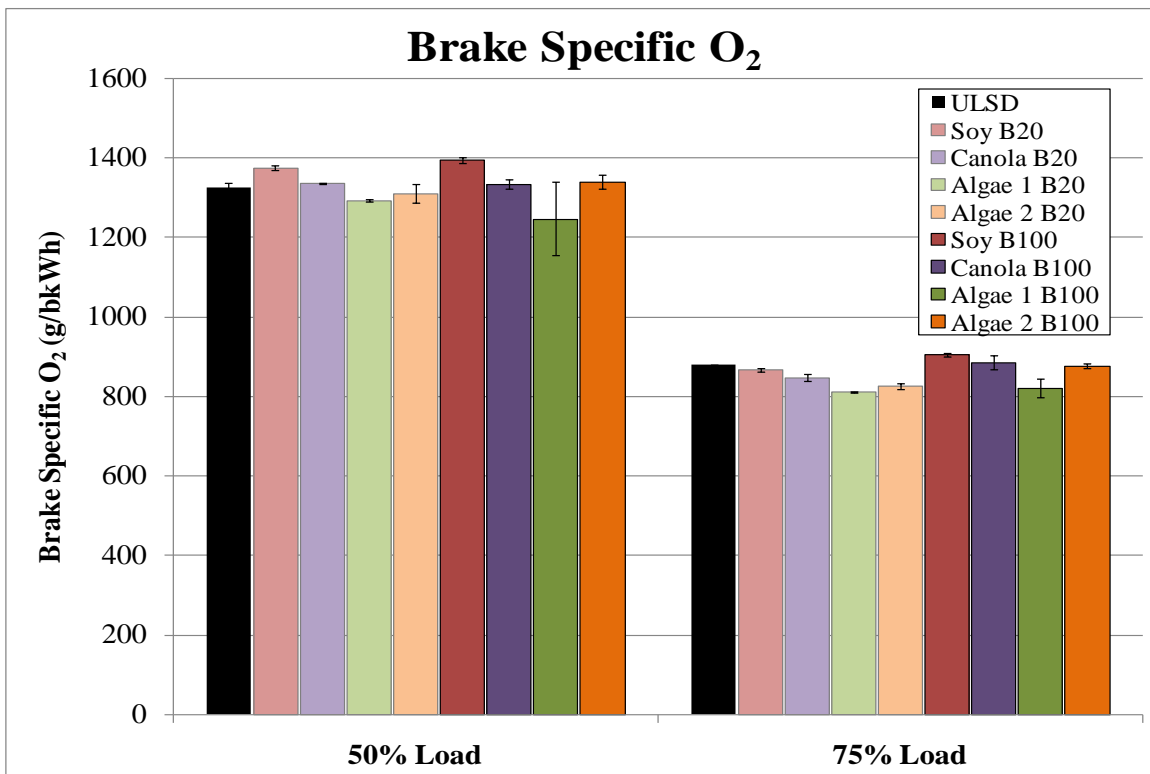
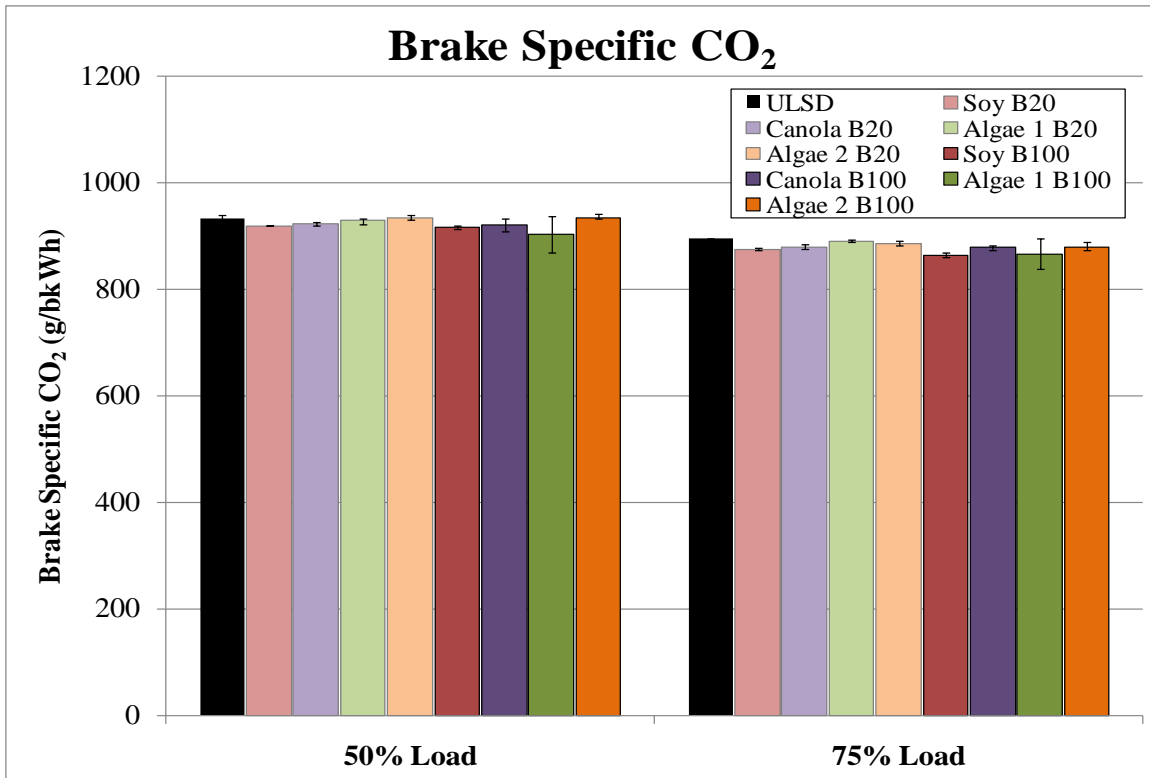
Williams, B.A., and J.W. Fleming. "Experimental and Modeling Study of NO Formation in 10 torr Methane and Propane Flames: Evidence for Additional Prompt-NO Precursors." *Proceedings of the Combustion Institute*, 2007: 1109-1117.

Winder, S. *Analog and Digital Filter Design*. Woburn, MA: Elsevier Science, 2002.

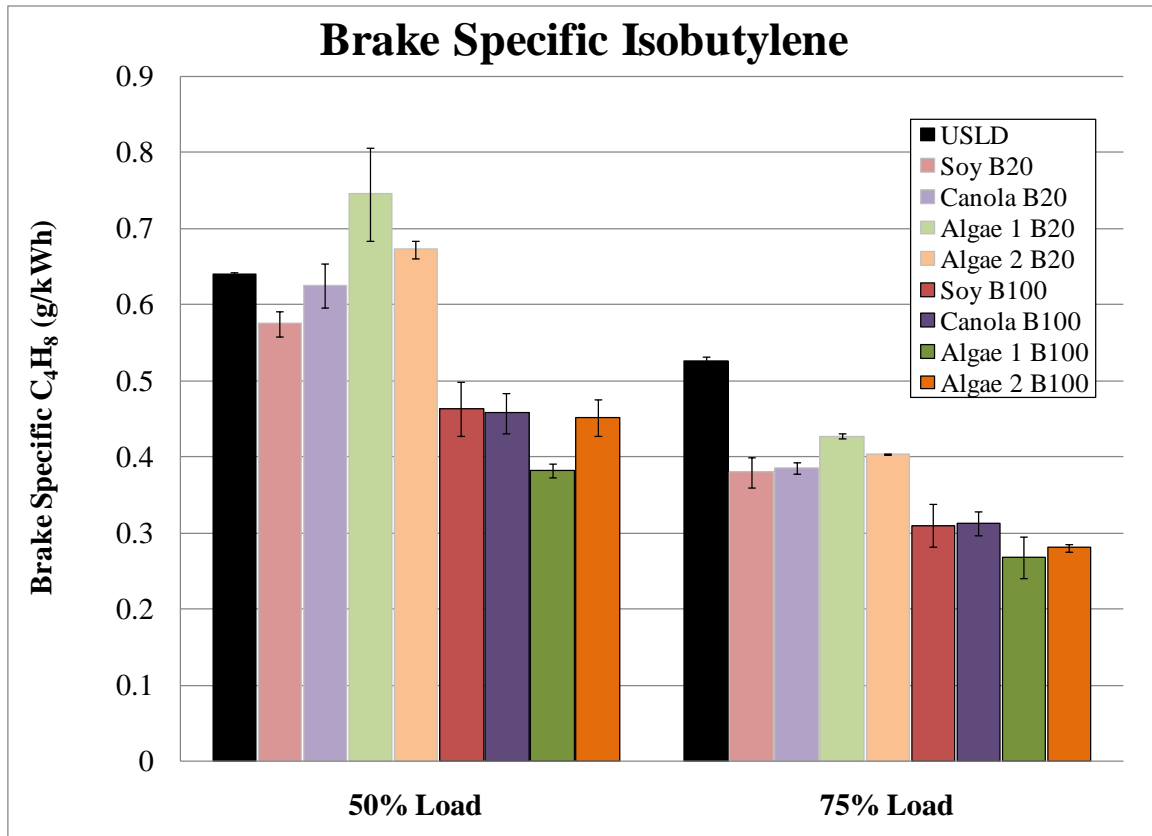
Yuan, W., A.C. Hansen, and Q. Zhang. "Predicting the Temperature Dependent Viscosity of Biodiesel Fuels." *Fuel*, 2009: 1120-1126.

Zhang, Y., and A. Boehman. "Impact of Biodiesel on NO<sub>x</sub> Emissions in a Common Rail Direct Injection Diesel Engine." *Energy and Fuels*, 2007: 2003-2012.

## APPENDIX A – ADDITIONAL 5-GAS RESULTS



## APPENDIX B – ADDITIONAL FTIR RESULTS



## APPENDIX C - HEAT RELEASE ANALYSIS

The two parameters used to control the Inverse Chebyshev filter were the order number and the low cutoff frequency. The values chosen for all of the results shown in Section 5.3.4 were an order of 7 and a low cutoff frequency of 0.25; found through trial and error. The following table shows how the order and low cutoff frequency affected the resulting heat release rate curve.

Figures showing how Inverse Chebyshev parameters affect heat release rate curve

